Earth-Science Reviews xxx (xxxx) 104138

Contents lists available at ScienceDirect

Earth-Science Reviews

journal homepage: www.elsevier.com/locate/earscirev

Crustal anatomy and evolution of a subduction-related orogenic system: Insights from the Southern Central Andes (22-35°S)

Laura Giambiagi [a,*], Andrés Tassara [b,c], Andrés Echaurren [a], Joaquín Julve [b,c], Rodrigo Quiroga [a], Matías Barrionuevo [a], Sibiao Liu [d], Iñigo Echeverría [b], Diego Mardónez [a], Julieta Suriano [a], José Mescua [a,e], Ana C. Lossada [f], Silvana Spagnotto [g,h], Macarena Bertoa [a], Lucas Lothari [a]

[a] IANIGLA-CONICET, Parque San Martín s/n, 5500 Mendoza, Argentina
[b] Departamento de Ciencias de la Tierra, Universidad de Concepción, Victor Lamas 1290, Concepción, Chile
[c] Millennium Nucleus CYCLO The Seismic Cycle along Subduction Zones, Chile
[d] GEOMAR, Helmholtz Centre for Ocean Research Kiel, Kiel, Germany
[e] Universidad Nacional de Cuyo, Mendoza, Argentina
[f] IDEAN-CONICET, Universidad de Buenos Aires, Argentina
[g] Universidad Nacional de San Luis. CONICET, San Luis, Argentina
[h] Universidad de Buenos Aires, Buenos Aires, Argentina

ARTICLE INFO

Keywords:
Central Andes
Mountain building
Subduction orogen
Kinematic forward modeling
Thermomechanical model
Geodynamic modeling
Orogenic processes
Decollement

ABSTRACT

As the archetype of mountain building in subduction zones, the Central Andes has constituted an excellent example for investigating mountain-building processes for decades, but the mechanism by which orogenic growth occurs remains debated. In this study we investigate the Southern Central Andes, between 22° and 35°S, by examining the along-strike variations in Cenozoic uplift history (<45 Ma) and the amount of tectonic shortening-thickening, allowing us to construct seven continental-scale cross-sections that are constrained by a new thermomechanical model. Our goal is to reconcile the kinematic model explaining crustal shortening-thickening and deformation with the geological constraints of this subduction-related orogen. To achieve this goal a representation of the thermomechanical structure of the orogen is constructed, and the results are applied to constrain the main decollement active for the last 15 Myr. Afterwards, the structural evolution of each transect is kinematically reconstructed through forward modeling, and the proposed deformation evolution is analyzed from a geodynamic perspective through the development of a numerical 2D geodynamic model of upper-plate lithospheric shortening.

In this model, low-strength zones at upper-mid crustal levels are proposed to act both as large decollements that are sequentially activated toward the foreland and as regions that concentrate most of the orogenic deformation. As the orogen evolves, crustal thickening and heating lead to the vanishing of the sharp contrast between low- and high-strength layers. Therefore, a new decollement develops towards the foreland, concentrating crustal shortening, uplift and exhumation and, in most cases, focusing shallow crustal seismicity. The north-south decrease in shortening, from 325 km at 22°S to 46 km at 35°S, and the cumulated orogenic crustal thicknesses and width are both explained by transitional stages of crustal thickening: from pre-wedge, to wedge, to paired-wedge and, finally, to plateau stages.

1. Introduction

In active subduction-type orogens like the Andes, the classic paradigm (Bally et al., 1966; Dewey and Bird, 1970; Uyeda and Kanamori, 1979; Suppe, 1981; Price, 1981; Ramos et al., 2002) proposes that mountain ranges grow through sequential stacking of crustal-thrust sheets from the hinterland (arc-region) to the foreland (back-arc region). This mechanism forms an internally-deformed crustal wedge, known as a fold-and-thrust belt, where thrusts are rooted into a major decollement. The critical wedge theory (Davis et al., 1983; Dahlen et al., 1984; Dahlen and Barr, 1989) assumes that the overall shape of the fold-and-thrust belt can be reproduced by a wedge of rocks having brit-

* Corresponding author.
E-mail address: lgiambiagi@mendoza-conicet.gob.ar (L. Giambiagi).

https://doi.org/10.1016/j.earscirev.2022.104138
Received 28 January 2022; Received in revised form 20 July 2022; Accepted 21 July 2022
0012-8252/© 20XX

tle behavior and frictionally sliding above a basal decollement. This belt may have different structural styles, where thick- or thin-skinned end-member models explain whether or not the structural basement is involved in the deformation (Lacombe and Bellahsen, 2016, and references therein). However, at an orogenic scale, these end-member models may not make sense, because, in the hinterland, the basement is always involved in deformation (e.g., Coward, 1983). At this orogenic scale, major decollements are mid-crustal shear zones, located beneath the bottom of the upper brittle crust, that concentrate most of the relative horizontal displacement between an upper and lower block (Harry et al., 1995; Oncken et al., 2012). They are regarded as mechanical discontinuities that are sharply delineated throughout the crust at medium geothermal gradients, being absent at low or high geothermal gradients (Ord and Hobbs, 1989). These shear zones have been proposed to extend sub-horizontally for great distances (Harry et al., 1995), constituting the main means of tectonic transport for mountain building in subduction-related orogens, such as the Central Andes (Isacks, 1988; McQuarrie, 2002; Oncken et al., 2003; Elger et al., 2005; Kley et al., 1997; Baby et al., 1997; Lacombe and Bellahsen, 2016; Martinod et al., 2020).

Worldwide, major decollements have been proposed for several orogenic systems, both in collisional orogens, such as the island of Taiwan (Suppe, 1981), the Apennines (Massoli et al., 2006), the Zagros (Mouthereau et al., 2006) or the Himalayas (Seeber et al., 1981; Avouac, 2008; Mukhopadhyay and Sharma, 2010), and in subduction-related orogens (Lacombe and Bellahsen, 2016, and references therein). Seismic reflection surveys have documented these decollements in the Pyrenees (Choukroune and ECORS Team, 1989; Mouthereau et al., 2007) and in the Central Andes (ANCORP-Working Group, 1999, 2003). In some of these orogens, like the Apennines (Massoli et al., 2006) or the Rocky Mountains (Bally et al., 1966), multiple decollements have been proposed. Several models propose a decoupling between the strong upper crust and the lower ductile crust, such as in the Zagros Mountain system (Mouthereau et al., 2006) and the Alps (Jammes and Huismans, 2012). In the Central Andes, this intracrustal decoupling zone has been visualized as a low-seismic velocity zone beneath the Altiplano-Puna plateau, resembling the crustal structure of the Tibetan plateau (Yuan et al., 2000). While these studies suggest the existence of decollements beneath the orogenic systems, the spatial and temporal distribution of these decollements remain matters of dispute.

The Central Andes constitute an excellent example for investigating a tectonically active subduction orogen, produced by long-term ocean-continent collision between the Nazca and South American plates. This Andean segment exhibits a pronounced variation of orogenic crustal volume and architecture along strike, related to contrasted amounts of crustal shortening-thickening and morphostructural configuration. Its southern part, the Southern Central Andes, ranges from the Altiplano-Puna plateau in the north (22-27.5°S), described as a large and hot orogenic configuration, to the Principal Cordillera in the south (35°S), a small and cold orogen, following the classification of Jamieson and Beaumont (2013). Another major geodynamic feature of the Southern Central Andes is the Pampean flat-slab segment between ~28 and 33°S, linked to changes in upper-plate deformation and an eastward migration of the Neogene arc front (Cahill and Isacks, 1992; Ramos et al., 2002). However, despite decades of study, first-order aspects of this cordilleran system remain as a matter of dispute, such as the overall direction of tectonic transport of the mountain belt, the spatio-temporal distribution of the decollements that deform the orogenic wedge, and the controlling factors over tectonic shortening and crustal thickness distribution. This is exemplified by different proposals at distinctive sectors of the Andes supported by intrinsically different kinematic models.

Specifically, at the Aconcagua latitudes (32-33°S), three types of models have been proposed: (i) a crustal-wedge model, (ii) an east-vergent model and (iii) a west-vergent model (Fig. 1).

The crustal-wedge model (Fig. 1A) proposes that one or two deep crustal wedges are pushed from the cratonic area into the orogenic system, forming a shallow, east-vergent, main decollement (Allmendinger et al., 1990; Cristallini and Ramos, 2000). This model implies an eastward advance of deformation, with the incorporation of new upper-crustal material at the tip of the eastern orogenic wedge. Under this model, the lower crust behaves as brittle material, and there is an asymmetric distribution of shortening.

The east-vergent model (Fig. 1B) is characterized by two decollements. The western one is rooted above the subduction-coupling zone and climbs upward and eastward into shallow crustal levels (Ramos et al., 2004; Farías et al., 2010; Giambiagi et al., 2012). Backthrusts affect the forearc region, but most of the shortening is absorbed along the east-vergent faults. The eastern decollement is younger, and disconnected from the western one, implying a migration of deformation towards the foreland.

The west-vergent model (Fig. 1C) is described as the juxtaposition of the crust and mantle lithosphere on top of the upper-crust at the core of the orogenic system (Armijo et al., 2010; Riesner et al., 2018, 2019). This proposal implies a concentration of shortening at the western cordillera slope and a younger western deformation, with the lithosphere behaving as brittle material. These three models imply the crustal root being constructed by the incorporation of material coming from the east, i.e., from the craton area toward the core of the orogenic system.

Similarly, for the Altiplano transect where the orogenic plateau is located (at latitude 21°-22°S), there are also different tectonic models. First, the east-vergent model proposes two main stacked decollements (Fig. 1D), located in the upper-to-middle crust (McQuarrie, 2002; Anderson et al., 2018). This model implies that deformation progresses eastwards with the incorporation of crustal material both from the forearc and the craton into the orogenic core. Secondly, the model with two disconnected decollements (Fig. 1E) proposes an east-vergent decollement below the Altiplano plateau and a doubly-vergent wedge with a west-vergent decollement below the Eastern Cordillera and an east-vergent decollement below the Sub-Andean ranges (Elger et al., 2005; Oncken et al., 2012). Finally, the doubly vergent, transcrustal-decollement model (Fig. 1F) proposes two opposite decollements reaching the Moho at the Altiplano axis (Armijo et al., 2015).

In our view, constraining the location and timing of activation and deactivation of these decollements appears as a key parameter for understanding orogen dynamics and the evolution of crustal anatomy. Since the Southern Central Andes exhibit significant variations in uplift history, amounts of crustal shortening, crustal anatomy and slab geometry (Jordan et al., 1983; Mpodozis and Ramos, 1989; Charrier et al., 2007; Ramos, 2018), we examine these along-strike changes by constructing seven continental-scale structural profiles crossing this subduction system (Fig. 2). These transects reproduce the present-day crustal structure by incorporating the differential mid-Cenozoic evolution (< 45 Ma) of the margin, reconciling diverse geological evidence, and constituting a suitable tool for testing the decollement activity, i.e., where and when the decollements are created and deactivated.

In this contribution we integrate a plethora of previous and new geological data of the Southern Central Andes (22-35°S) for evaluating the tectonic and deformational evolution of this segment. First, we describe its morphotectonic configuration and present a thorough and updated compilation of previous geological data at a regional scale. Here, we describe the dominant geological units and the main episodes of crustal deformation, exhumation, and basin generation for each of these transects. These data are used to build the seven continental cross-sections from which we obtained new estimations of crustal shortening and thickening values through forward structural modeling. We also present new thermomechanical results for these transects identifying the present-day low-strength zones where the major decollements are likely located and constraining the crustal structure of the last stage of the

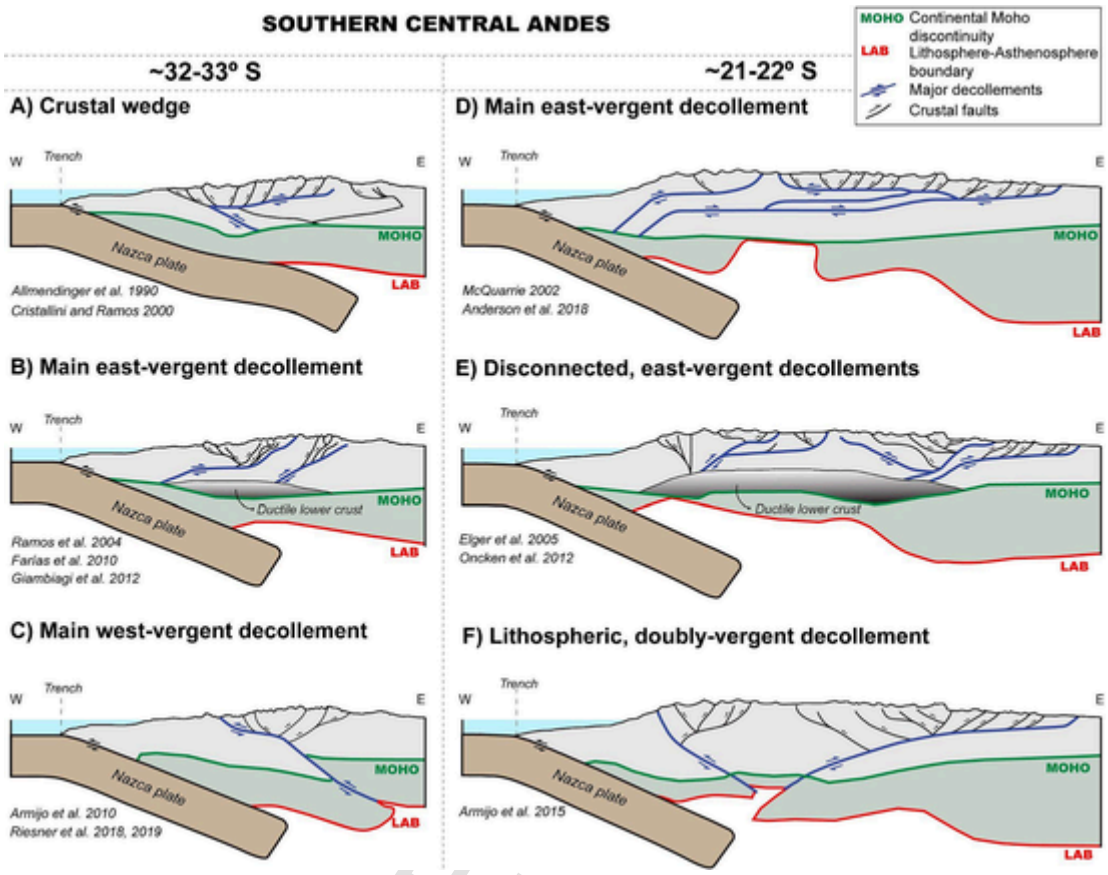

Fig. 1. Different structural models explaining the crustal and lithospheric deformation in the Central Andes at 32-33°S latitudes (A-C) and 21-22°S latitudes (D-F). The sketches are redrawn from published studies (A: Cristallini and Ramos, 2000; B: Giambiagi et al., 2015a; C: Armijo et al., 2010; D: McQuarrie, 2002; E: Elger et al., 2005; F: Armijo et al., 2015).

structural modeling (the last 15 Myr). Additionally, we perform new numerical simulations through a geodynamic model that characterizes the spatio-temporal evolution of crustal faulting.

These results are used to discuss the role that the thermal structure has on crustal rheology and the occurrence of low-strength decollements in the upper crust where surface structures can be rooted. We argue that the presence of sub-horizontal layers with contrasting strength promotes the generation of decollement levels in different sectors of the orogenic crust. However, this time-dependent rheological condition changes during the construction of the crustal root and the thinning of the lithosphere, which increase mid-crustal temperatures, reducing or eliminating the rheological contrast between the upper and lower crust, and therefore inducing the abandonment of the decollement and the generation of a new one towards the east, in an east-vergent evolution mode.

2. Geotectonic setting of the Southern Central Andes (22°-35°S)

The Southern Central Andes comprise, in its northern sector (22° - 27° S): (i) the Coastal Range, which mainly includes Jurassic to Cretaceous magmatic arcs and associated sedimentary basins (Reutter et al., 1996; Riquelme et al., 2003; Oliveros et al., 2006); (ii) the Chilean Precordillera, or Domeyko Range, corresponding to the Late Cretaceous to Eocene magmatic arc, developed over a Devonian to Triassic basement (Coira et al., 1982; Amilibia et al., 2008; Mpodozis and Cornejo, 2012); (iii) the Western Cordillera, with the Miocene to Holocene magmatic arc (De Silva et al., 2006; Kay and Coira, 2009); (iv) the internally-drained Altiplano/Puna plateau, with an average elevation of 4000 m (Isacks, 1988; Allmendinger et al., 1997); (v) the doubly vergent thrust belt of the Eastern Cordillera, which uplifts late Proterozoic to Paleozoic metasedimentary and sedimentary rocks (Sempere et al., 1990; Reutter et al., 1994; Kley and Monaldi, 2002; Hongn et al., 2010), (vi) the active eastward-tapering sedimentary wedge of Paleozoic to Neogene rocks of the Sub-Andean fold-and-thrust belt, north of 24°S, and the Santa Bárbara basement-involved fault system, south of 24°S (Mingramm et al., 1979; Allmendinger et al., 1983; Roeder, 1988; Sheffels, 1990; Baby et al., 1992, 1995; Dunn et al., 1995; Kley and Reinhardt, 1994; McQuarrie, 2002); and, (vii) the foreland basin, filled with wedge-shaped Neogene clastic strata of up to 6 km of thickness, known as the Chaco Plains (Uba et al., 2005, 2006). This basin is underlayed by the Brazilian craton, which has been a stable nucleus of South America since the Proterozoic (Litherland et al., 1985).

The Coastal Range is characterized by the presence of a pronounced high-velocity seismic wave anomaly to a depth of 60 km (Heit et al., 2008). To the east, geophysical analyses indicate petrophysical properties of the crust below the Altiplano, Puna and Eastern Cordillera (high Vp/Vs, high attenuation, high conductivity), which may reflect a hydrated partially-melted crust at a depth of 15-25 km, known as the Altiplano Low-Velocity Zone ALVZ (Wigger et al., 1994; Graeber and Asch, 1999; Yuan et al., 2000; Schurr et al., 2003; Haberland and Rietbrock, 2001; Oncken et al., 2003; Heit et al., 2008). The high topography of the Altiplano/Puna plateau is isostatically supported by both a 60-to-75-km-thick continental crust (Yuan et al., 2000; Beck and Zandt, 2002; McGlashan et al., 2008; Tassara and Echaurren, 2012) and a thermally-thinned lithosphere underlain by a low-density asthenosphere (Froidevaux and Isacks, 1984; Schurr et al., 1999; Prezzi et al., 2014; Ibarra et al., 2019). The lithosphere is proposed to be thermally thinned because of the removal of a dense and thickened, gravitationally-unstable, mantle lithosphere via delamination (Kay and Kay, 1993; Kay et al., 1994b; Garzione et al., 2017; Chen et al., 2020) or other dynamic

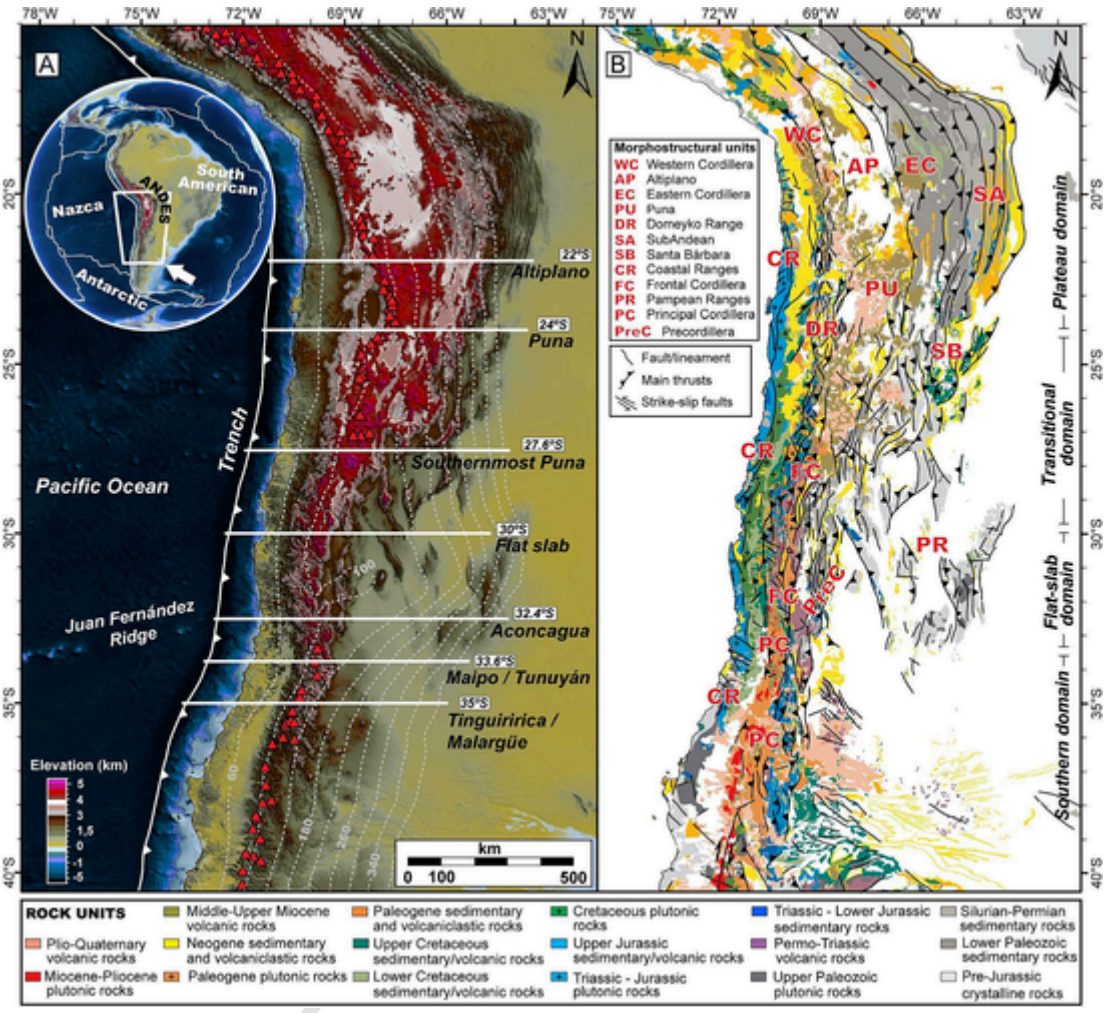

Fig. 2. Tectonic setting, main geological units and structural features of the Central Andes. A) DEM-derived topographic map highlighting the contrasting surface expression of the Andes in this portion of the margin. Grey dashed lines correspond to 40-km depth slab contours (Tassara and Echaurren, 2012) and red triangles to the active volcanic front. White East-West lines are the seven crustal-scale structural cross-sections analyzed in this work (Figs. 3 to 9). B) Simplified geological map (modified from Gómez et al., 2019), showing the main geological units, morphostructural units (red labels) and structural configuration of the Andean margin. (For interpretation of the references to colour in this figure legend, the reader is referred to the web version of this article.)

mechanisms. The thickness of the crust was mainly achieved by Cenozoic tectonic shortening, linked to eastward displacement of megathrust sheets (Sheffels, 1990; Schmitz and Kley, 1997; McQuarrie, 2002; McQuarrie et al., 2005). The crust below the Eastern Cordillera and Sub-Andean Ranges reaches a thickness of 40 km (Schmitz and Kley, 1997).

According to the most widely accepted structural model, the flexurally-strong lithosphere representing the Brazilian shield (Watts et al., 1995) is being underthrusted beneath the Sub-Andean Ranges and the Eastern Cordillera, as is evidenced by seismicity extending ~120 km west from the thrust front (Cahill and Isacks, 1992; Asch et al., 2006). To the west, seismicity is diffuse, and, in the Puna/Altiplano plateau, focal mechanisms show components of strike-slip and normal faulting (Allmendinger et al., 1997; Asch et al., 2006).

To the south, the Andes narrows from ~500 km in the Andean plateau to ~200 km at 35°S, and the crustal thickness diminishes from >65 km at 30°S to <55 km in the south (e.g. Introcaso et al., 1992; Fromm et al., 2004; Gans et al., 2011; Tassara and Echaurren, 2012). The Chilean/Pampean flat-slab segment (28°-32.5°S) is characterized by a relatively shallow subduction angle (Isacks and Barazangi, 1977; Anderson et al., 2007) and a lack of active arc-related magmatism resulting from the eastward migration of the asthenospheric wedge (Pilger, 1981; Kay et al., 1988; Ramos et al., 2002). At these latitudes, the orogen comprises, from west to east, the following five morphotectonic provinces: (i) the Coastal Range, which underlies the modern forearc and is composed of Paleozoic and early Mesozoic accretionary belts (Díaz-Alvarado et al., 2019), and Jurassic to Lower Cretaceous plutonic and volcanic rocks (Mpodozis and Ramos, 1989); (ii) the Principal Cordillera, characterized by thick Jurassic and Cretaceous marine and continental sedimentary sequences deformed within fold-and-thrust belts (Ramos et al., 1996b); (iii) the Frontal Cordillera, which consists of Proterozoic to Devonian metamorphic rocks, Carboniferous-Permian marine sedimentary rocks and Permian-Triassic volcanic and plutonic rocks (del Rey et al., 2019); (iv) the Precordillera which corresponds to a fold-and-thrust belt composed of Paleozoic sedimentary rocks (Astini and Thomas, 1999; Mardonez et al., 2020); and (v) the Pampean Ranges, which are characterized by east and west- vergent uplifted basement blocks (Ramos et al., 2002).

South of 32.5°S, the slab has a sub-horizontal subduction angle transitionally smoothing to a normal subduction geometry as it gets south of 34°S (Cahill and Isacks, 1992), where it reaches an angle of 27° (Nacif et al., 2015). In the transitional zone (32.5°-34°S), the Frontal Cordillera, the Precordillera and the Pampean Ranges gradually disappear, while the magmatic arc becomes active together with the development of the east-directed Malargue fold-and-thrust belt. Along the

32.5° to 35°S segment, horizontal shortening and crustal thickness decrease southward (Giambiagi et al., 2012).

3. Geological background of the transects

3.1. The Altiplano transect (22°S)

Previous to 45 Ma, deformation was localized in the magmatic arc, along the proto-Domeyko Range (Fig. 3), in a crustal-scale pop-up structure bounded by east- and west-directed reverse faults (Marinovic and Lahsen, 1984; Andriessen and Reutter, 1994; Reutter et al., 1996; Sempere et al., 1997; Maksaev and Zentilli, 1999; Ladino et al., 1999; Tomlinson et al., 2001, 2018; Muñoz et al., 2002; Victor et al., 2004; Mpodozis and Cornejo, 2012; Bascuñán et al., 2016; Tomlinson et al., 2018; Henriquez et al., 2019; López et al., 2020), as well as strike-slip faults along the Atacama fault system (Reutter et al., 1996; Riquelme et al., 2003; Farías et al., 2005).

During the middle Eocene (45-40 Ma), the crust achieved a thickness of >45 km below the Domeyko Range (Haschke et al., 2002). The uplift of this range is constrained by thermochronology (Maksaev and Zentilli, 1999; Avdievitch et al., 2018) and the development of the Calama basin which received sediments from the west (Blanco et al., 2003). A rapid cooling of the Coastal Range is suggested to be related to forearc uplift and exhumation (Juez-Larré et al., 2010; Reiners et al., 2015; Stalder et al., 2020). During this period, movement along the Khenayani-Uyuni fault system (Martínez et al., 1994; Sempere et al., 1990; Scheuber et al., 2006) occurred in the western Altiplano, prior to the deposition of the Late Oligocene- Middle Miocene San Pedro and San Vicente Formations in the Salar de Atacama and Lípez basins, respectively (Blanco et al., 2003; Elger et al., 2005). The proto-Eastern Cordillera was deformed by east-directed faults (Lamb et al., 1997). This uplift is registered in the sedimentary provenance of the foreland basin (Horton and DeCelles, 2001).

Between 40 and 35 Ma, shortening was focused on the Western Cordillera, as well as on the westernmost Altiplano and Eastern Cordillera (Kennan et al., 1995; Sempere et al., 1997; Horton, 1998, 2005; Horton and DeCelles, 2001; DeCelles and Horton, 2003; McQuarrie et al., 2005; Elger et al., 2005; Ege et al., 2007). The Calama basin continuously received sediments from the west and south (Blanco et al., 2003). The Domeyko Range became affected by strike-slip faults, such as the dextral movement of the West Fault (Maksaev and Zentilli, 1988, 1999; Mpodozic et al., 1993; Lindsay et al., 1995; Tomlinson et al., 2010) associated with a mylonitic fabric over plutonic complexes (Tomlinson et al., 2018).

During the 35-30 Ma period, the Lípez basin continued receiving sediments from both the west and east (Baby et al., 1990), with the continuous uplift of the Western Cordillera (Scheuber et al., 2006), the Eastern Cordillera controlled by the west- and east-directed faults (Roeder, 1988; Mon and Hongn, 1991; Baby et al., 1992; Kley et al., 1997; Allmendinger et al., 1997; McQuarrie and DeCelles, 2001; McQuarrie, 2002; McQuarrie et al., 2005; Hongn et al., 2007; Anderson et al., 2018) and the east-directed faults affecting the central Altiplano (Elger et al., 2005). During this phase, between 36 and 33 Ma, the giant Chuquicamata porphyry system was syntectonically emplaced at the Domeyko Range through the dextral strike-slip of the West Fault (Lindsay et al., 1995; Reutter et al., 1996; Tomlinson et al., 2010, 2018; Mpodozis and Cornejo, 2012).

Between 30 and 21 Ma, extensional deformation was localized in the Calama (Blanco, 2008) and Salar de Atacama basins (Flint et al., 1993; Jordan et al., 2007), associated with a sinistral/normal movement of the West Fault system (Tomlinson et al., 2018). Contractional

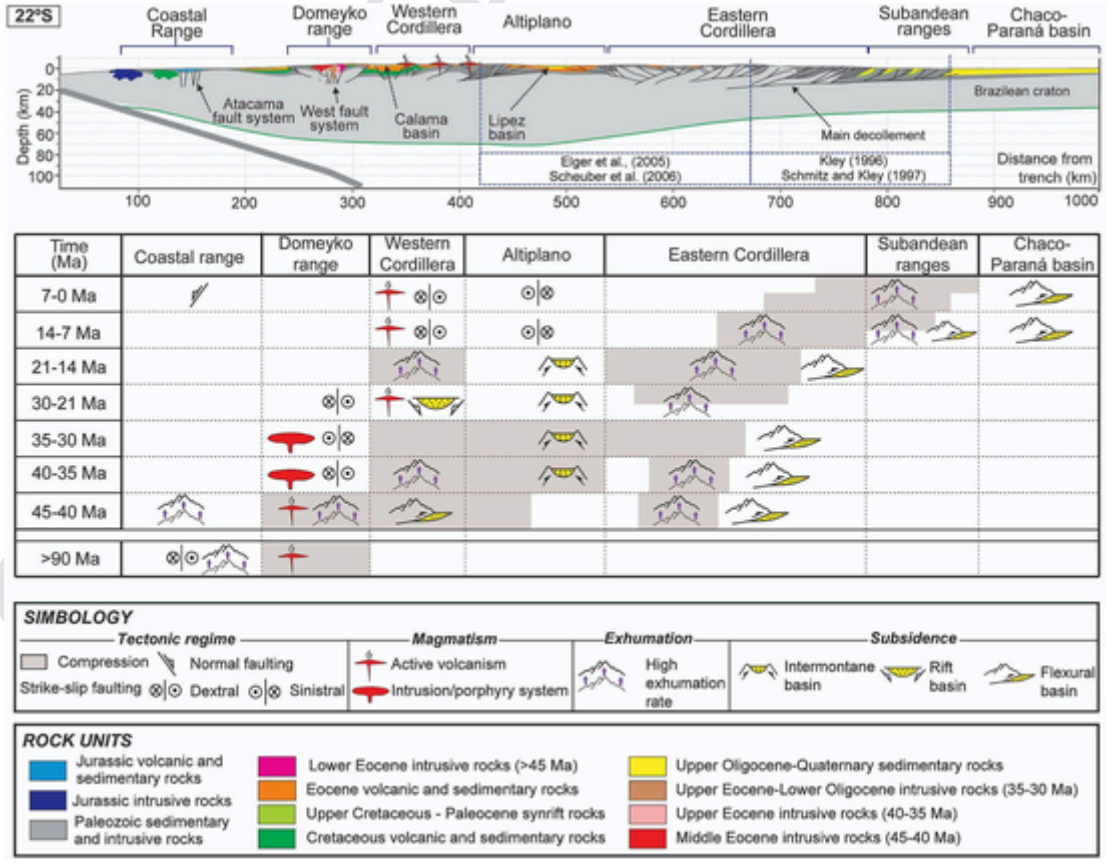

Fig. 3. Geological cross-section along the 22°S, constructed with previous geological data and partial balanced cross-sections (Schmitz and Kley, 1997; Elger et al., 2005), and chart describing the different deformational stages affecting the transect area according to published data.

deformation was only focused on the Eastern Cordillera with a peak of deformation between 25 and 17 Ma (Elger et al., 2005).

Between 21 and 14 Ma, the Eastern Cordillera experienced contractional deformation and main exhumation (Kley, 1996; Horton, 1998; McQuarrie, 2002; Müller et al., 2002; Strecker et al., 2007). The Khenayani-Uyuni fault system got deactivated (Gubbels et al., 1993). Arid paleosols of the middle Miocene in the Salar de Atacama basin are overlain by late Miocene ignimbrites (Cowan et al., 2004; Jordan et al., 2014) suggesting a minimum age for the contractional deformation in the Domeyko Range and Western Cordillera.

Between 14 and 7 Ma, deformation concentrated along the eastern part of the Eastern Cordillera and, after 10 Ma, along the Sub-Andean thin-skinned fold-and-thrust belt (Mingramm et al., 1979; Allmendinger et al., 1983; Roeder, 1988; Sheffels, 1990; Baby et al., 1992, 1995; Dunn et al., 1995; Kley and Reinhardt, 1994; McQuarrie, 2002; Echavarria et al., 2003; Uba et al., 2009; Oncken et al., 2012 (Rojas Vera et al., 2019)), which absorbs ~55 km of shortening (Lamb and Hoke, 1997; Horton, 1998; Müller et al., 2002; Victor et al., 2004; Elger et al., 2005). The oldest undeformed lava covering the western and central Altiplano thrust faults was dated at ~11 Ma (Baker and Francis, 1978; Silva-González, 2004), suggesting a minimum age for the end of shortening. Strike-slip faulting affected the Western Cordillera (Giambiagi et al., 2016) and the Altiplano (Riller et al., 2001; Acocella et al., 2011; Bonali et al., 2012; Lanza et al., 2013). Likewise, deformation ceased in the Eastern Cordillera at 9-10 Ma, based on the distribution and undeformed nature of the San Juan de Oro erosional surface (Gubbels et al., 1993). The Chaco-Paraná foreland basin started to develop at 12.4 Ma (Uba et al., 2009), underlain by the Brazilian craton, a stable continental nucleus of South America since the Proterozoic (Litherland et al., 1985).

During the Late Miocene-Quaternary period (7-0 Ma), contractional deformation was concentrated along the easternmost Eastern Cordillera and the Sub-Andean ranges. Presently, the Sub-Andean ranges show active growth at its deformation front, as evidenced from seismicity and GPS data (Bevis et al., 1999; Lamb, 2000; Hindle and Kley, 2003; Brooks et al., 2011). The Atacama fault system was reactivated during the Pliocene-Quaternary as a normal fault system (González et al., 2003, 2006).

Along this transect, the main decollement has been proposed to be located below the Eastern Cordillera and Sub-Andean ranges and to be responsible for the underthrusting of the flexurally-strong Precambrian Brazilian craton (Lyon-Caen et al., 1985; Isacks, 1988; Watts et al., 1995; Allmendinger and Gubbels, 1996; Lamb et al., 1997; Allmendinger et al., 1997; Anderson et al., 2018) under the thermomechanically weakened Andean sector (Baby et al., 1997; Lamb et al., 1997; Watts et al., 1995; Beck and Zandt, 2002; Ibarra et al., 2021). This decollement, located between 20 and 8 km depth, has a regional dip of 2° to 3° to the west (Kley and Monaldi, 2002; Pearson et al., 2013), and it is rooted by a ramp into the ductile and low-strength zone (Oncken et al., 2003; Lamb et al., 1997; Lynner et al., 2018), deep in mid crustal levels. The location of this ramp has been inferred from a dislocation model for back-arc deformation presented by Brooks et al. (2011) along the Altiplano transect, and by McFarland et al. (2017) along the Puna.

3.2. The Puna transect (24°S)

Prior to 45 Ma, the inversion of several back-arc basins took place (Fig. 4), such as the Mesozoic Domeyko basin (Ramirez and Gardeweg, 1982; Mpodozis et al., 2005; Arriagada et al., 2006; Marinovic, 2007; Mpodozis and Cornejo, 2012; González et al., 2020) and the Salar de

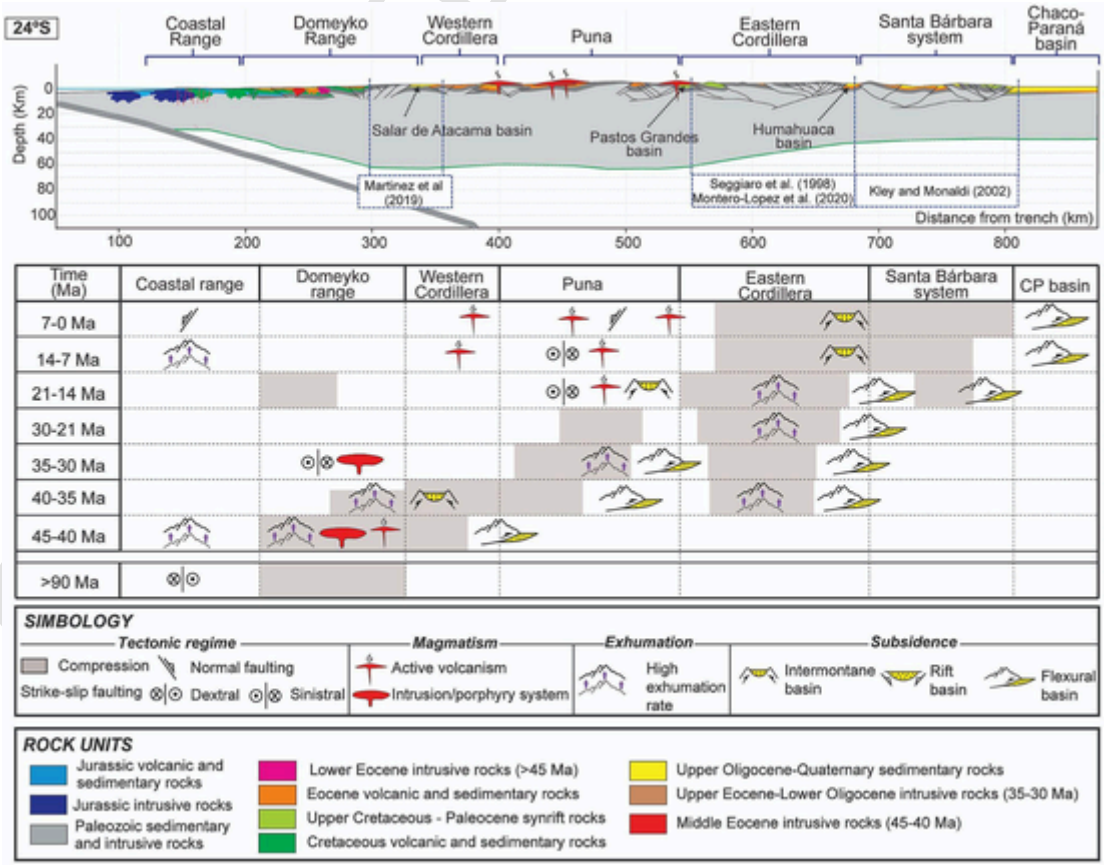

Fig. 4. Geological cross-section along the 24°S, constructed with previous geological data and balanced cross-sections (Seggiaro et al., 1998; Kley and Monaldi, 2002; Montero-López et al., 2020), and chart describing the different deformational stages affecting the transect area according to published data.

Atacama/Salar de Punta Negra foreland basin (Jordan et al., 2007; Martínez et al., 2019, 2020). This generated a thick crust below the Domeyko Range (40 to 45 km, Haschke et al., 2002; Haschke and Gunther, 2003; Amilibia et al., 2008; González et al., 2020), while the Salta rifting produced a thin crust below the actual Santa Bárbara range (Salfity and Marquillas, 1994; Comínguez and Ramos, 1995; Marquillas et al., 2005; Kley et al., 2005).

During the middle Eocene (45-40 Ma), the inversion of the Atacama basin in the Domeyko Range took place (Maksaev and Zentilli, 1999; Carrapa and DeCelles, 2008; Reiners et al., 2015), with the generation and/or reactivation of strike-slip and reverse faults and sedimentation in the Salar de Atacama basin (Mpodozis and Cornejo, 2012). During the 40-35 Ma period, shortening was focused on the eastern Domeyko Range (Maksaev and Zentilli, 1999; Amilibia et al., 2008) and the proto-Puna (Haschke et al., 2005; Carrapa and DeCelles, 2008 (Henriquez et al., 2020)). At the end of this period, strike-slip faults affected the Domeyko Range (Niemeyer and Urrutia, 2009), associated with the intrusion of giant porphyry copper bodies, such as the Escondida cluster (38-35 Ma) (Kay et al., 1999; Mpodozis and Cornejo, 2012; Hervé et al., 2012). The distal foreland experienced the first basement uplift of the Eastern Cordillera (Andriessen and Reutter, 1994; Seggiaro et al., 1998; del Papa, 1999; del Papa et al., 2013; Coutand et al., 2001; Deeken et al., 2006; Hongn et al., 2007, 2010; Payrola et al., 2009; Pearson et al., 2013; Montero-López et al., 2016), delimiting basins with internal drainage such as the Humahuaca basin (del Papa et al., 2013; Montero-López et al., 2020). This uplift had a Basin-and-Range or Pampean Range style (Coutand et al., 2001) with reactivation of pre-existing faults affecting the pre-Mesozoic basement (Hongn et al., 2010).

During the 35-30 Ma period, contractional deformation was concentrated in the eastern Puna (Quade et al., 2015) and the Eastern Cordillera (Deeken et al., 2006; Pearson et al., 2013). Afterwards, during the 30-21 Ma period, the Eastern Cordillera continued to uplift (Coutand et al., 2006; Deeken et al., 2006; Pearson et al., 2013). During the next stage, between 21 and 14 Ma, there was an eastward shift of thrusting from the plateau into the foreland (Deeken et al., 2006; Pearson et al., 2012). At the end of this stage, broken foreland basins with internal drainage conditions characterized the Puna and Puna/Eastern Cordillera border (Siks and Horton, 2011; DeCelles et al., 2015a; Pingel et al., 2019). Paleoaltimetric studies in the Arizaro basin at the central Puna suggest that uplift preceded the filling of the basin (Canavan et al., 2014; Quade et al., 2015). To the west, in the Domeyko Range, a low-intensity contractional event was registered after 17 Ma (Soto et al., 2005).

During the 14-7 Ma period, the uplift of the eastern sector of the Eastern Cordillera took place (Deeken et al., 2006).This phase is marked by the collapsed calderas on the plateau (Coira et al., 1982; De Silva, 1989a) and sinistral strike-slip deformation along NW-SE trending lineaments, such as the Olacapato-El Toro fault system (Riller et al., 2001; Acocella et al., 2011; Bonali et al., 2012; Lanza et al., 2013; Petrinovic et al., 2010, 2021); as well as intermontane sedimentation in the Puna region (del Papa and Petrinovic, 2017; Pingel et al., 2019).

During the last stage (7-0 Ma), the Santa Barbara system developed as a bivergent thick-skinned fold-and-thrust belt (Allmendinger et al., 1983; Reynolds et al., 2000) controlled by pre-existing Cretaceous normal faults (Kley and Monaldi, 2002). Between 7 and 3.5 Ma, extensional faults were active in the southern Puna(Schoenbohm and Strecker, 2009), as well as in the Atacama fault system (González et al., 2003, 2006).

3.3. The Southernmost Puna transect (27.6°S)

During the Late Cretaceous (Fig. 5), a compressional event thickened the crust in the present forearc and the westernmost sector of the Frontal Cordillera (Mpodozis et al., 1995; Kay and Mpodozis, 2001; Martínez et al., 2016, 2021). During the middle to upper Eocene (45-38 Ma), the eastern Coastal Range and the western Frontal Cordillera started to uplift (Cornejo et al., 1993; Tomlinson et al., 1993, 1994;

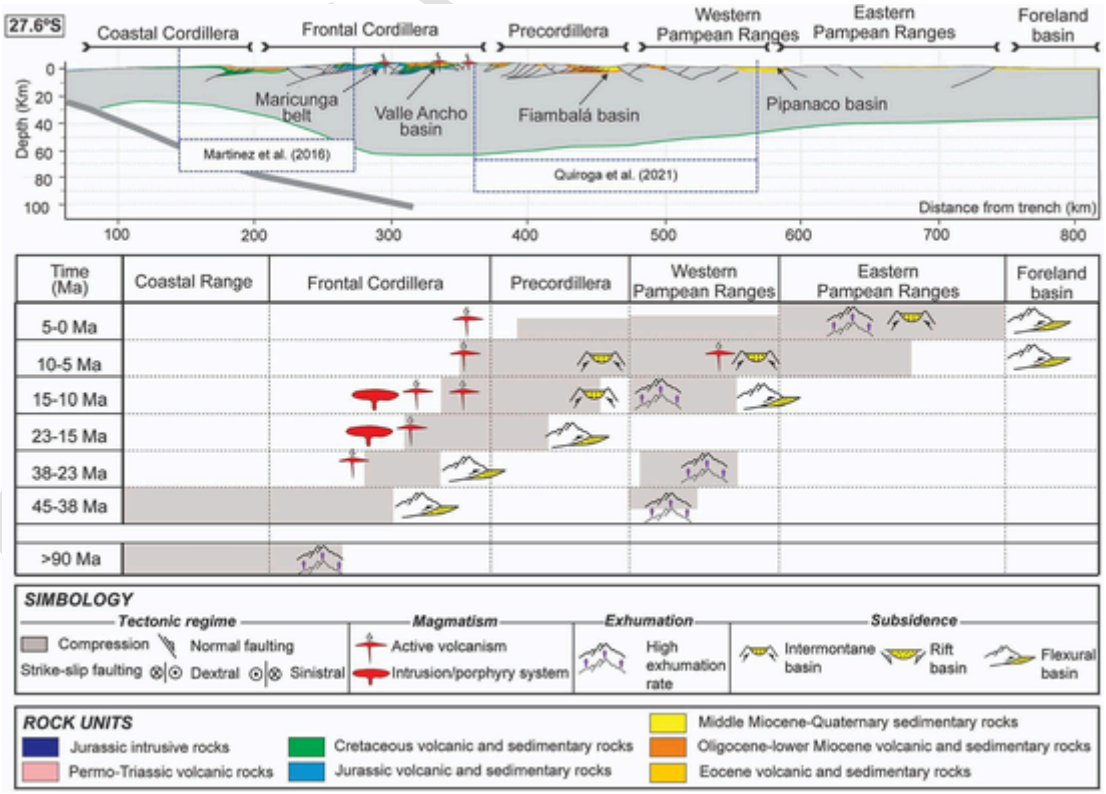

Fig. 5. Geological cross-section along the 27.6°S, constructed with previous geological data and balanced cross-sections (Martínez et al., 2016; Quiroga et al., 2021), and chart describing the different deformational stages affecting the transect area according to published data.

Martínez et al., 2016, 2021). Sediments reached the foreland basin located in the central and eastern Frontal Cordillera and southernmost Puna at ~38 Ma (Zhou et al., 2017; Montero-López et al., 2020), coevally to the onset of the Pampean Ranges uplift, according to thermochronological data (Coutand et al., 2001; Mortimer et al., 2007). The waning of contractional activity in the western Frontal Cordillera occurred at the end of this phase (Cornejo et al., 1993; Tomlinson et al., 1993, 1994).

During the upper Eocene-Oligocene (38-23 Ma), the crust thickened and reached 45 km below the Maricunga volcanic belt (Kay and Mpodozis, 2001; Mpodozis et al., 2005), located in the western Frontal Cordillera. . A short period of extension took place during the Oligocene, evidenced by local extensional basins contemporaneous with the volcanism developed along the Maricunga belt (Mpodozis et al., 2018). At the end of this period (~26 Ma), contractional deformation affected the easternmost sector of the western Frontal Cordillera (Mpodozis et al., 2018; Martínez et al., 2016; Quiroga et al., 2021). The proximal foreland basin associated with this stage corresponds to the Valle Ancho basin (Mpodozis et al., 1997). During this stage, the distal foreland registered another pulse of uplift and exhumation (Coutand et al., 2001).

During the early Miocene (23-15 Ma), a compressional phase affected the eastern Frontal Cordillera (Mpodozis et al., 1995, 2018; Coutand et al., 2001) and the Fiambalá basin started to receive sediments (Safipour et al., 2015; Deri et al., 2019). The crust achieved a thickness > 50 km (Kay and Mpodozis, 2001). Deformation propagated to the east, reaching the Fiambalá basin during the middle Miocene (15-10 Ma, Carrapa et al., 2008; Safipour et al., 2015), at the time when voluminous stratovolcanic complexes were emplaced at the Maricunga belt. The crust achieved its maximum thickness in this stage (>60 km; Kay et al., 1994a, 2013; Mpodozis et al., 1995), and the volcanic arc migrated eastward to its present position, close to the border between the Frontal Cordillera and the Precordillera (Mpodozis and Kay, 2009; Goss et al., 2013).

At 13 Ma, the western sector of the Pampean Ranges started to uplift (Carrapa et al., 2006, 2008, 2011; Davila and Astini, 2007; Mortimer et al., 2007; Dávila, 2010; Seggiaro et al., 2014; Safipour et al., 2015). This is registered in the sedimentary fill of the intermontane basins (Strecker et al., 1989; Muruaga, 1998; Bossi et al., 2001; Mortimer et al., 2007; Bossi and Muruaga, 2009; Bonini et al., 2017). During the late Miocene, deformation was focused in the Fiambalá basin, which continued to receive sediments (Carrapa et al., 2008; Quiroga et al., 2021), while the eastern sector of the Pampean Ranges started to uplift (Sobel and Strecker, 2003; Mortimer et al., 2007; Bossi and Muruaga, 2009), showing a doubly vergent thrusting style (Cristallini et al., 2004). Back-arc volcanism of 9.5-6 Ma corresponds to the Farallón Negro volcanic complex located in the Pampean Ranges (Sasso, 1997; Harris et al., 2004; Halter et al., 2004). The Aconquija range started to uplift during the middle Miocene, ~12-9 Ma to the present (Löbens et al., 2013; Zapata et al., 2019, 2020), and since ~3 Ma the orographic barrier conditions were established (Sobel and Strecker, 2003; Zapata et al., 2019).The generation of a broken foreland is marked by deposition of sedimentary sequences in isolated basins (Bossi et al., 2001; Mortimer et al., 2007; Bossi and Muruaga, 2009).

3.4. The flat-slab transect (30°S)

Prior to 45 Ma (Fig. 6), the forearc and backarc crust had a normal thickness (Jones et al., 2016). The magmatic arc was present in the Frontal Cordillera and forearc region was affected by the Atacama fault

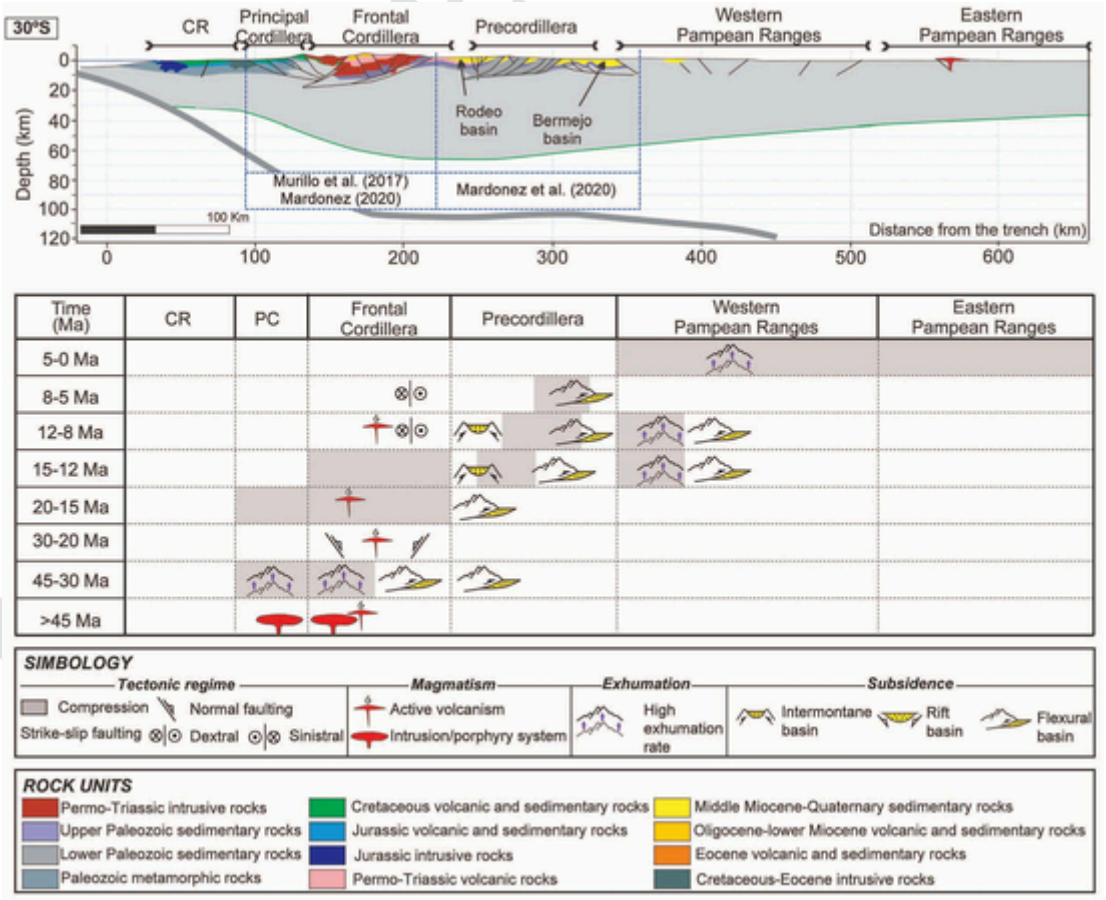

Fig. 6. Geological cross-section along the 30°S, constructed with previous geological data and balanced cross-sections (Murillo et al., 2017; Mardonez, 2020; Mardonez et al., 2020), and chart describing the different deformational stages affecting the transect area according to published data.

system (Arabasz, 1971). During the middle Eocene, thrusts and back-thrusts uplifted both the Principal Cordillera (Moscoso and Mpodozis, 1988; Emparan and Pineda, 1999) and the western sector of the Frontal Cordillera (Martin et al., 1997; Cembrano et al., 2003; Lossada et al., 2017; Murillo et al., 2017; Rodríguez et al., 2018). This uplift occurred simultaneously to deposition of distal sediments in the present Precordillera (Fosdick et al., 2017; Reat and Fosdick, 2018). Between 30 and 20 Ma, extension in the back-arc region (Winocur et al., 2015; González et al., 2020) controlled the extrusion of volcanic-arc deposits (Doña Ana arc) in the Frontal Cordillera (Maksaev et al., 1984; Jones et al., 2016; Murillo et al., 2017).

During the early Miocene, 20-15 Ma, the western Frontal Cordillera was uplifted through the east-directed Baños del Toro fault system (Moscoso and Mpodozis, 1988; Martin et al., 1995, 1997, Giambiagi et al., 2017). The eastern Frontal Cordillera started to uplift (Beer et al., 1990;(Rodríguez Fernández et al., 1999) Heredia et al., 2002;(Hoke et al., 2014) Mackaman-Lofland et al., 2019, Mardonez et al., 2020, Mackaman-Lofland et al., 2020,), related to flexural subsidence in the Rodeo basin (Reynolds et al., 1990) and basins located nowadays inside the Precordillera (Levina et al., 2014; Suriano et al., 2015;). New low-temperature thermochronological data indicate reactivation of pre-existing faults in the westernmost Pampean Ranges (Ortiz et al., 2021).

Between 15 and 12 Ma, an eastward jump of the deformational front is marked by both thrusting in the western Precordillera (Suriano et al., 2017) and initial sedimentation in the Bermejo basin (Johnson et al., 1986; Jordan et al., 2001; Fosdick et al., 2015; Capaldi et al., 2020). In the Frontal Cordillera, contractional deformation was sealed by the Cerro Las Tórtolas volcanism (Maksaev et al., 1984; Murillo et al., 2017) but the eastern part of this range continued to be uplifted by a deeply-seated ramp (Allmendinger et al., 1990; Mardonez et al., 2020).

The back-arc volcanism was placed in the Rodeo basin and in the central Precordillera (Poma et al., 2017).

During 12-8 Ma period, the central Precordillera and western Pampean Ranges were deformed and uplifted (Jordan et al., 1993; Coughlin et al., 1998; Levina et al., 2014; Allmendinger and Judge, 2014; Fosdick et al., 2015), while deformation ceased in the western Precordillera. This event is associated with a pronounced flexural subsidence in the Bermejo basin (Mardonez et al., 2020). The magmatic arc, with a geochemical signature indicating a thick crust, was established at the Rodeo basin and eastern Precordillera (Gualcamayo igneous complex; Poma et al., 2017; D'nnunzio et al., 2018). Contraction deformation continued, between 8 and 5 Ma, with reverse faulting in the central Precordillera, during ongoing uplift of the Pampean Ranges (Jordan and Allmendinger, 1986; Ramos et al., 2002; Fosdick et al., 2015).

The Plio-Quaternary was marked by the last uplift of the Central Precordillera, deformation of the eastern Precordillera (Zapata and Allmendinger, 1996), and continuing uplift of the Pampean Ranges (Ortiz et al., 2015, 2021). Arc magmatism migrated towards the east to the Pampean Ranges, where it finally waned (Ramos et al., 2002). Neotectonic activity is present in the Rodeo basin (Siame et al., 2005; Perucca and Martos, 2012; Fazzito et al., 2013; Perucca and Vargas, 2014) and the Pampean Ranges (Costa et al., 2001; Perucca et al., 2018).

3.5. The Aconcagua transect (32.4°S)

During the Early Cretaceous, the crust was thin (< 33 km) below the Mesozoic marine basin, at the present-day Principal Cordillera, and it has a normal thickness (35-38 Ma) below the Pampean Ranges (Fig. 7) (Perarnau et al., 2012). During the Late Cretaceous a compressional

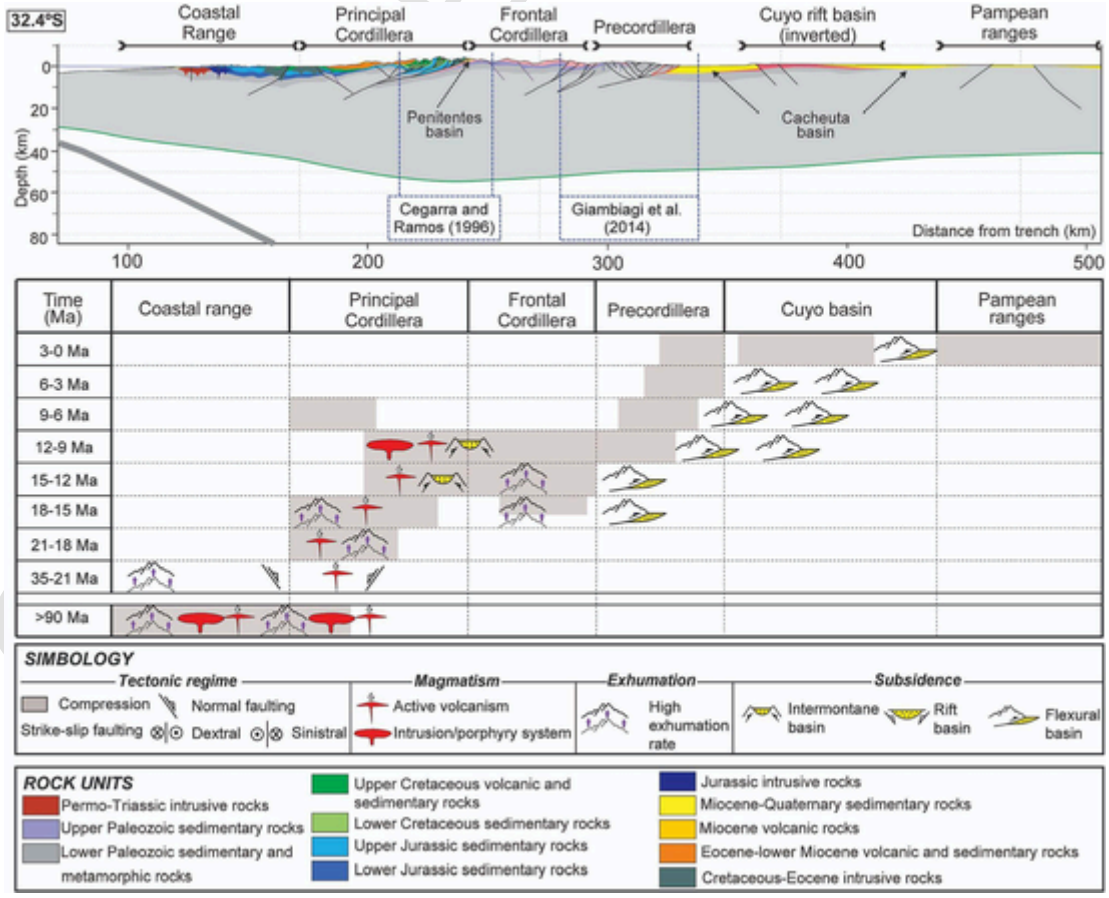

Fig. 7. Geological cross-section along the 32.4°S, constructed with previous geological data and balanced cross-sections (Cegarra and Ramos, 1996; Giambiagi et al., 2014), and chart describing the different deformational stages affecting the transect area according to published data.

event affected the western Principal Cordillera and Coastal Range (Arancibia, 2004; Jara and Charrier, 2014; Rodríguez et al., 2018), but crustal thickness in the eastern Principal Cordillera remained normal (35 km; Carrapa et al., 2022). Afterward, during the late Eocene-early Miocene, extensional relaxation with mild horizontal extension took place (Charrier et al., 2005, 2009; Mpodozis and Cornejo, 2012; Piquer et al., 2016; Mackaman-Loftand et al., 2019; Boyce et al., 2020); while the Coastal Range experienced uplift (Stalder et al., 2020). The Miocene-Present contraction started at ~21-18 Ma, as registered in the western sector of the Principal Cordillera (Jara and Charrier, 2014) with high exhumation (Rodríguez et al., 2018; Stalder et al., 2020) and in the synorogenic record of the Cacheuta basin (Irigoyen et al., 2000; Buelow et al., 2018).

At 18 Ma, the Aconcagua fold-and-thrust belt started to develop as a thin-skinned belt in the eastern sector (Cegarra and Ramos, 1996; Martos et al., 2022) and a thick-skinned belt in its western sector with the inversion of pre-existing normal faults of the Abanico basin (Fock et al., 2006; Mardones et al., 2021). During this stage, the volcanic arc migrated from the Farellones arc (23-17 Ma) in western Principal Cordillera (Charrier et al., 2002; Nyström et al., 2003), to the Aconcagua arc (15-8 Ma) in the eastern Principal Cordillera (Ramos et al., 1996a). Uplift of the Frontal Cordillera took place during this time (~17 Ma; Buelow et al., 2018; Lossada et al., 2020).

During the 12 to 9 Ma period, the Aconcagua FTB continued to deform below a crust of 44 km (Carrapa et al., 2022). Both Frontal Cordillera and Precordillera raised during this period (Ramos et al., 2004; Giambiagi et al., 2011(Hoke et al., 2014)), in agreement with sedimentological and provenance data from the Cacheuta basin (Buelow et al., 2018). Afterward, deformation is only concentrated in the eastern Precordillera, while the western Principal Cordillera experienced a reactivation (Farías et al., 2008). During the next period, between 6 and 3 Ma, the deformation migrated to the present thrust front in the easternmost Precordillera (Richard, 2020).

During the late Pliocene to Quaternary, horizontal shortening was accommodated along the easternmost sector of the eastern Precordillera, and the Cacheuta basin experienced uplift and denudation (Buelow et al., 2018) and active reverse faulting (Cortés et al., 1999; Costa et al., 2000, 2015; Richard et al., 2019; Rimando et al., 2019). Towards the east, the uplift of the Pampean Ranges formed the broken foreland (Jordan et al., 1983; Ramos et al., 2002), where opposite-directed faults, controlled by inherited anisotropies, localize Quaternary deformation (Costa et al., 2019). These faults are interpreted to be deeply rooted into the lower crust (Perarnau et al., 2012).

3.6. The Maipo/Tunuyán transect (33.6°S)

During the late Eocene to early Miocene times (Fig. 8), a protracted extensional event affected the western sector of the Principal Cordillera and generated the Abanico intra-arc basin (~35-21 Ma, Charrier et al., 2002; Muñoz et al., 2006; Piquer et al., 2017), associated with a ~ 30-35 km thick continental crust (Nyström et al., 2003; Kay et al., 2005; Muñoz et al., 2006). The Cenozoic compressional event started at 21-18 Ma, with the early inversion of the Abanico basin (Godoy et al., 1999; Charrier et al., 2002; Fock et al., 2006;(Rodríguez et al., 2012) Piquer et al., 2016), and was coeval with the development of the Farellones volcanic arc (Vergara et al., 1999). In the foreland, the back-arc volcanism of the Contreras Formation predated the formation of the Alto Tunuyán foreland basin (Giambiagi and Ramos, 2002), with a geochemical signature related to a thin or normal crust (Ramos et al., 1996b).

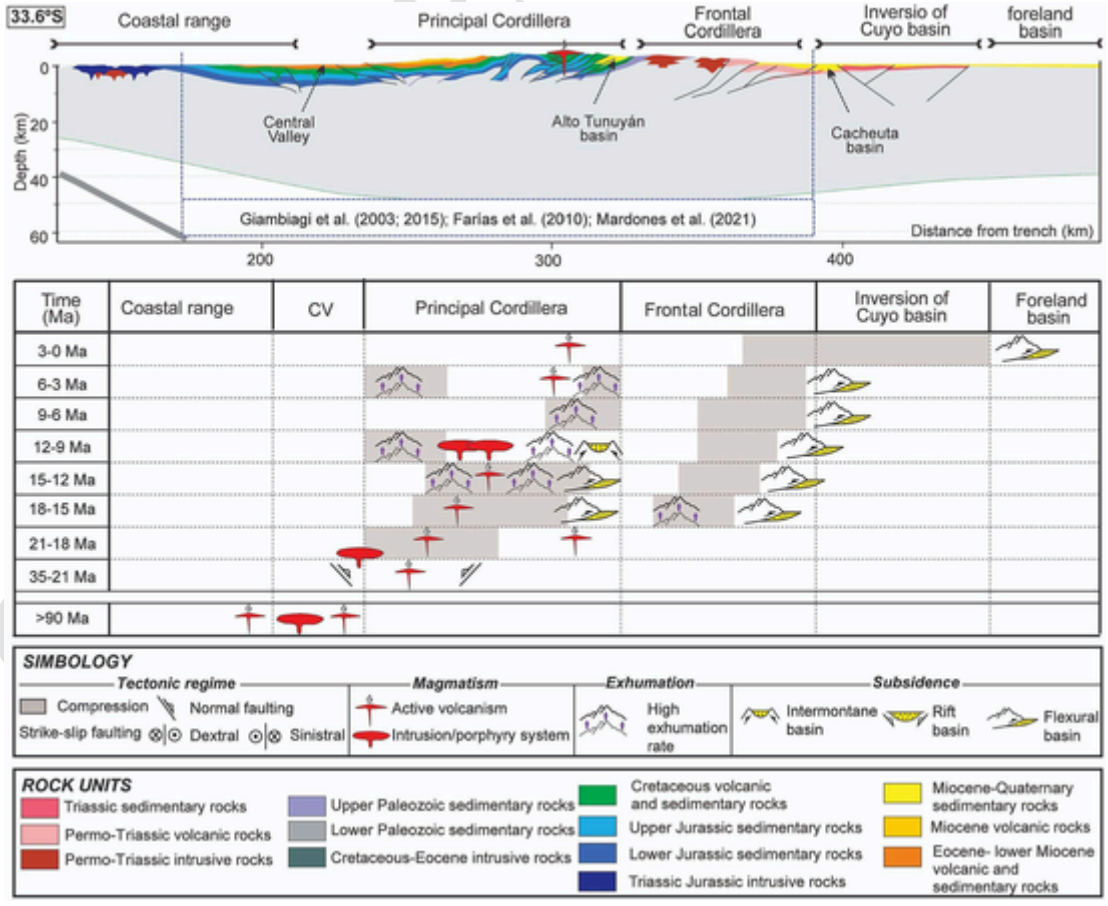

Fig. 8. Geological cross-section along the 33.6°S, constructed with previous geological data and balanced cross-sections (Giambiagi et al., 2003, 2015a; Farías et al., 2010; Mardones et al., 2021), and chart describing the different deformational stages affecting the transect area according to published data.

Uplift of the Aconcagua fold-and-thrust belt (Giambiagi and Ramos, 2002) and the Frontal Cordillera (Buelow et al., 2018; Lossada et al., 2020) initiated during the 18-15 Ma period. Both ranges produce flexural subsidence in the Alto Tunuyán intermontane basin (Porras et al., 2016) and in the Cacheuta basin (Irigoyen et al., 2000; Buelow et al., 2018).

During the middle Miocene (15-12 Ma), shortening was mainly absorbed in the Aconcagua FTB (Cegarra and Ramos, 1996). Both the Alto Tunuyán (Giambiagi et al., 2003; Porras et al., 2016) and Cacheuta (Buelow et al., 2018) basins continued to receive sediments. During the 12-9 Ma period, the volcanic activity practically waned, and plutons and porphyries intruded the Miocene Farellones volcanic arc (Kay and Kurtz, 1995; Kurtz et al., 1997; Kay et al., 2005; Deckart et al., 2010). Sedimentary provenance analysis (Irigoyen et al., 2000; Giambiagi et al., 2003; Porras et al., 2016; Buelow et al., 2018) indicates that, during the late Miocene (9-6 Ma), an important uplift of the eastern Frontal Cordillera took place. The ~2 km of topographic uplift in the Alto Tunuyán basin has been related to the addition of lower crustal material (Hoke et al., 2014). However, western Principal Cordillera was still active, and was responsible for the back-thrust activity (Farías et al., 2008) and exhumation (Maksaev et al., 2004).

Magmatic activity resumed during the Pliocene at its current locus along the High Andean drainage divide. Shortening was absorbed in the eastern Frontal Cordillera, with generation of frontal thrusts affecting the Cacheuta basin deposits (Irigoyen et al., 2000) and the inversion of the Triassic Cuyo basin (Giambiagi et al., 2015b). During the upper Pliocene – Quaternary, shortening was accommodated in the Frontal Cordillera (García and Casa, 2015) and the westernmost sector of the Principal Cordillera with movements along the San Ramón fault (Vargas et al., 2014; Yáñez et al., 2020). Between 6 Ma and the present, a significant increase in exhumation rates along the western slope of the Andes has been attributed to a drastic change in climate (Stalder et al., 2020).

3.7. The Tinguiririca/Malargüe transect (35°S)

Uplift of the westernmost part of the Principal Cordillera occurred during the late Cretaceous (Fig. 9) (>90 Ma, Tunik et al., 2010; Mescua et al., 2013, 2014), but it is not until the middle Miocene (16-13 Ma) that deformation and uplift propagated eastward (Baldauf, 1997), producing the inversion of early Mesozoic inherited normal faults of the Neuquén basin extension (Mescua et al., 2014). This contraction produced flexural subsidence in the Malargüe foreland basin (Horton et al., 2016). The 13-10 Ma period recorded further advance of the deformation towards the foreland (Giambiagi et al., 2008; Mescua et al., 2014; Fuentes et al., 2016; Horton et al., 2016). Out of sequence activity in the westernmost structures (El Fierro fault system, Godoy et al., 1999) took place likely during this stage, although the chronology of this reactivation in the inner sector is not clear.

The main structures along the mountain front, such as the Malargüe fault, started their activity between 10 and 6 Ma (Silvestro et al., 2005; Boll et al., 2014; Fuentes et al., 2016), while out-of-sequence uplift and exhumation were recorded in the western Principal Cordillera around 8 Ma (Spikings et al., 2008). Out-of-sequence deformation was observed for the Las Leñas fault in the middle sector of the fold-and-thrust belt likely between 6 and 3 Ma (Kozlowski et al., 1993; Bande et al., 2020). During the late Pliocene-Quaternary, shortening was transferred to the easternmost sector of the Malargüe FTB, at the present orogenic front (Silvestro et al., 2005; Fuentes et al., 2016).

4. Methodology

4.1. Thermomechanical structure

To better understand how orogenic-scale deformation occurs and which kinematic model best explains the observed geological data, we first construct a representation of the thermomechanical structure un-

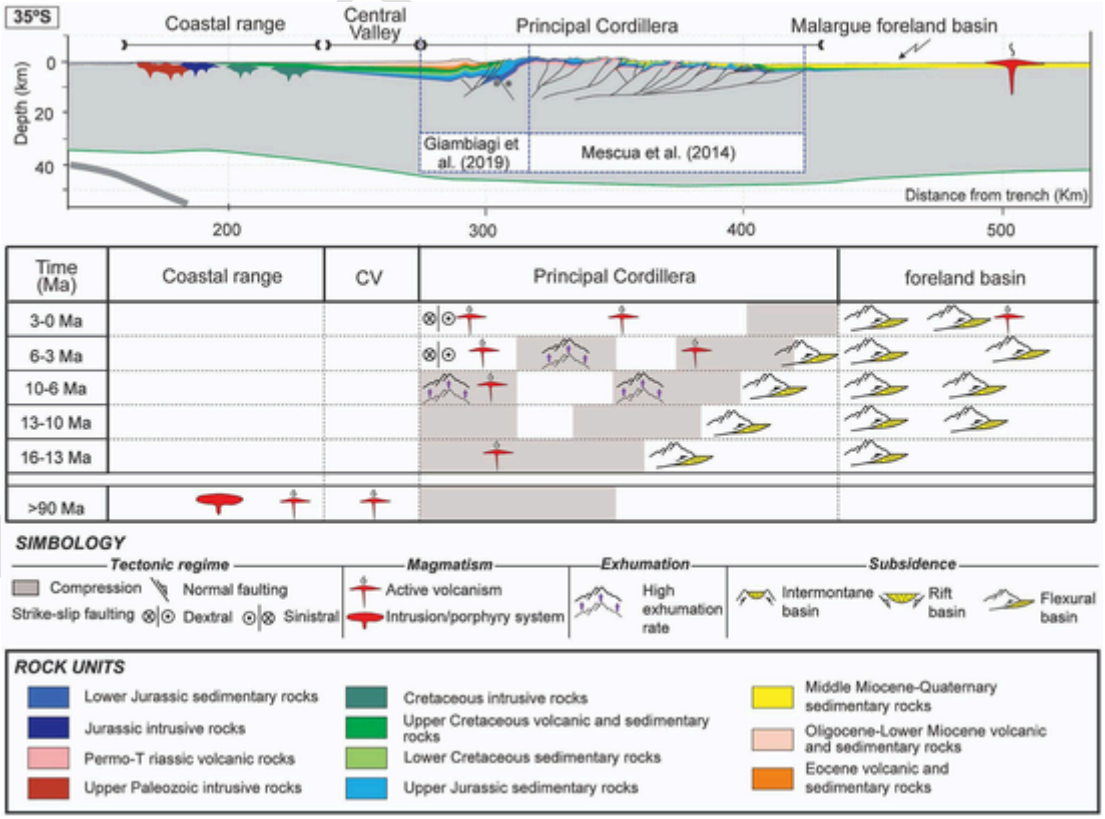

Fig. 9. Geological cross-section along the 35°S, constructed with previous geological data and balanced cross-sections (Mescua et al., 2014; Giambiagi et al., 2019), and chart describing the different deformational stages affecting the transect area according to published data.

derneath the Central Andes. This model considers the geometries of geophysically-constrained lithospheric discontinuities and simple analytical expressions for temperature and brittle-elasto-ductile rheology.

We start from the 1D steady-state heat conduction equation with volumetric heat production. For the boundary conditions, we follow previous studies (Fox-Maule et al., 2005) by assuming that temperature T_b at a certain depth Z_b is independently known and that radiogenic heat decays exponentially with depth from a surface value H_0. Under these assumptions, a convenient form of the 1D geothermal gradient describing the variation of temperature T with depth Z can be derived:

$$T(Z) = \frac{Qm}{k}Z - \frac{H_0 Z_i}{k}\left(Z_i\left(1 + exp^{\frac{-Z}{Z_i)}}\right) + Z\,exp^{\frac{-Z_m}{Z_i)}}\right) \quad (1)$$

Here, k is thermal conductivity, Z_i is the depth scale for exponential radiogenic decay, Z_m is Moho depth and Q_m is heat flow at the Moho, which can be defined as:

$$Q_m = \frac{1}{Z_b}\left[T_b k - H_0 Z_i\left(Z_i - \exp^{\frac{(-Z_m}{Z_i)}}\left(Z_i + Z_m\right)\right)\right] \quad (2)$$

In order to provide values of Z_i, Z_m and the pair (T_b, Z_b), we consider the outputs of the geophysically-constrained 3D density model of the Andean margin (Tassara and Echaurren, 2012). This model was constructed by forward modeling of the Bouguer gravity anomaly under the geometric constraints imposed by published seismic results. The main output of this model is the geometry for the subducted slab, the Lithosphere-Asthenosphere Boundary (LAB) underneath the continental plate, the continental Moho that we assume equal to Z_m, and the intracrustal density discontinuity (ICD) separating dense lower crust from light upper crust. As radioactive elements are concentrated in the upper crust, we assume in our thermal model that the depth to the ICD defines the parameter Z_i. Considering E-W cross-sections for the computation of the model, and for those points located eastward of the Slab-LAB intersection, we impose that:

$$T_b = T_p + GZ_b \quad (3)$$

Where T_p is mantle potential temperature, G is an adiabatic gradient and Z_b is defined by the depth to the LAB. A similar relation holds for points of the cross section located westward from the Slab-LAB intersection (Molnar and England, 1990), for which Z_b corresponds to the slab depth:

$$T_b = \frac{\left(Q_0 + \sigma V\right)Z_b}{k\left(1 + \frac{\sqrt{Z_b V sin\alpha}}{\kappa}\right)} \quad (4)$$

Here, α is the average subduction angle, κ is thermal diffusivity, and σ is shear stress at the interplate fault. The slab heat flow Q_0 depends on the age of the slab at the trench t (which we take from Müller et al., 2016) and is defined as:

$$Q_0 = \frac{kT_p}{\sqrt{\pi\kappa t}} \quad (5)$$

Ensuring continuity of the temperature field between the eastern and western domains (i.e., equaling eqs. 3 and 4), a value of σ at the Slab-LAB intersection can be prescribed. Assuming a linear decrease to zero of this parameter toward the trench axis along the cross section, eq. 4 can be fully evaluated.

Values of the physical parameters included in eqs. 1 to 5 (Table A1.1 in Supplementary Material 1) were selected as averages for the study region and/or assuming common values from the literature (i.e., Turcotte and Schubert, 2014).

After computing the values of Tb in eqs. 3 and 4, they can be replaced in eq. 2 and then in eq. 1 to define the 1D geotherm for each point of the EW cross section. The 1D temperature distribution T(Z) at these points is then used to prescribe the ductile yield strength σ_d with depth Z:

$$\sigma_d(Z) = \frac{\dot{\varepsilon}}{A}^{1/n} \exp\frac{H}{nRT(Z)} \quad (6)$$

Here $\dot{\varepsilon} = 10^{-15}$ s^{-1} is strain rate, R is the gas constant, and n, H and A are empirical material properties that depend on rock composition. Considering the compositional layering of the input model (Tassara and Echaurren, 2012) we assigned values to these parameters as shown in Table A1.2 in Supplementary Material 1.

We also consider that brittle yield strength σ_b increases linearly with depth Z at a constant gradient of 55 MPa/km (Burov and Diament, 1995). At a given depth, the actual yield strength (i.e., the maximum differential stress that can be elastically supported before permanent deformation is activated) will be the minimum between σ_d and σ_b. The yield strength envelope (YSE) constructed in this way predicts the potential mechanical behavior of crust and mantle. The actual brittle, elastic and/or ductile behavior results from the intersection of the YSE with a given differential stress gradient. Although the form of this gradient with depth is not known and could include in-plane tectonic stresses and flexural stresses due to plate bending (i.e., Burov and Diament, 1995), we preferred to use a simple constant value of differential tectonic stress σe = 100 MPa, which is at the upper bound of values estimated along the Andean margin (Coblentz and Richardson, 1996; Tassara, 2005; Flesch and Kreemer, 2010). Into this framework, areas with yield strength higher than this value are expected to behave elastically and transmit stresses, while areas with lower strength may deform either in a brittle (upper crust) or ductile (lower crust and mantle) manner (Fig. 10).

By implementing the method described above to the seven transects analyzed by us, we obtain thermomechanical transects like those of Fig. 10, which are then used to constraint the present-day crustal structure in our kinematic structural models.

4.2. Crustal structure and kinematic modeling with thermomechanical constraints

Our models assume that upper crustal faults are preferentially rooted in a shallow, sub-horizontal decollement located inside a low-strength zone ($\sigma_d < \sigma_e$) derived from the thermo-mechanical model described above. The base of this shallow low-strength zone corresponds to the base of the upper crust in all of our thermomechanical transects for regions above the hot orogenic axis (Fig. 10), and it is defined by the depth to the ICD in the density model of Tassara and Echaurren (2012). The roof of the shallow low-strength zone is marked by the depth to the isotherm for which $\sigma_d = \sigma_e$. For the selected upper crustal material in our model (Table A1.2 in Supplementary Material 1), this isotherm is given by a temperature of ~250 °C. Similarly, the roof of the deep low-strength mid-lower crust is defined by the 550 °C isotherm.

For each section, geological background and published partial balanced cross-sections are first used to construct a geometric model of the time-zero stage (T0, >45 Ma) and a final (present-day) non-restored section with contacts between different lithologies, dips and outcropping faults and folds. We then use the academic license of MOVE suite (Petroleum Experts) for forward modeling several successive deformation stages that are constrained by stratigraphic, structural, sedimentological, thermochronological and geochemical observations. We sequentially deform the upper crustal layers by imposing horizontal shortening at the western border of the modal to reach the final present-day stage (Supplementary Material 2). For each stage we use the pub-

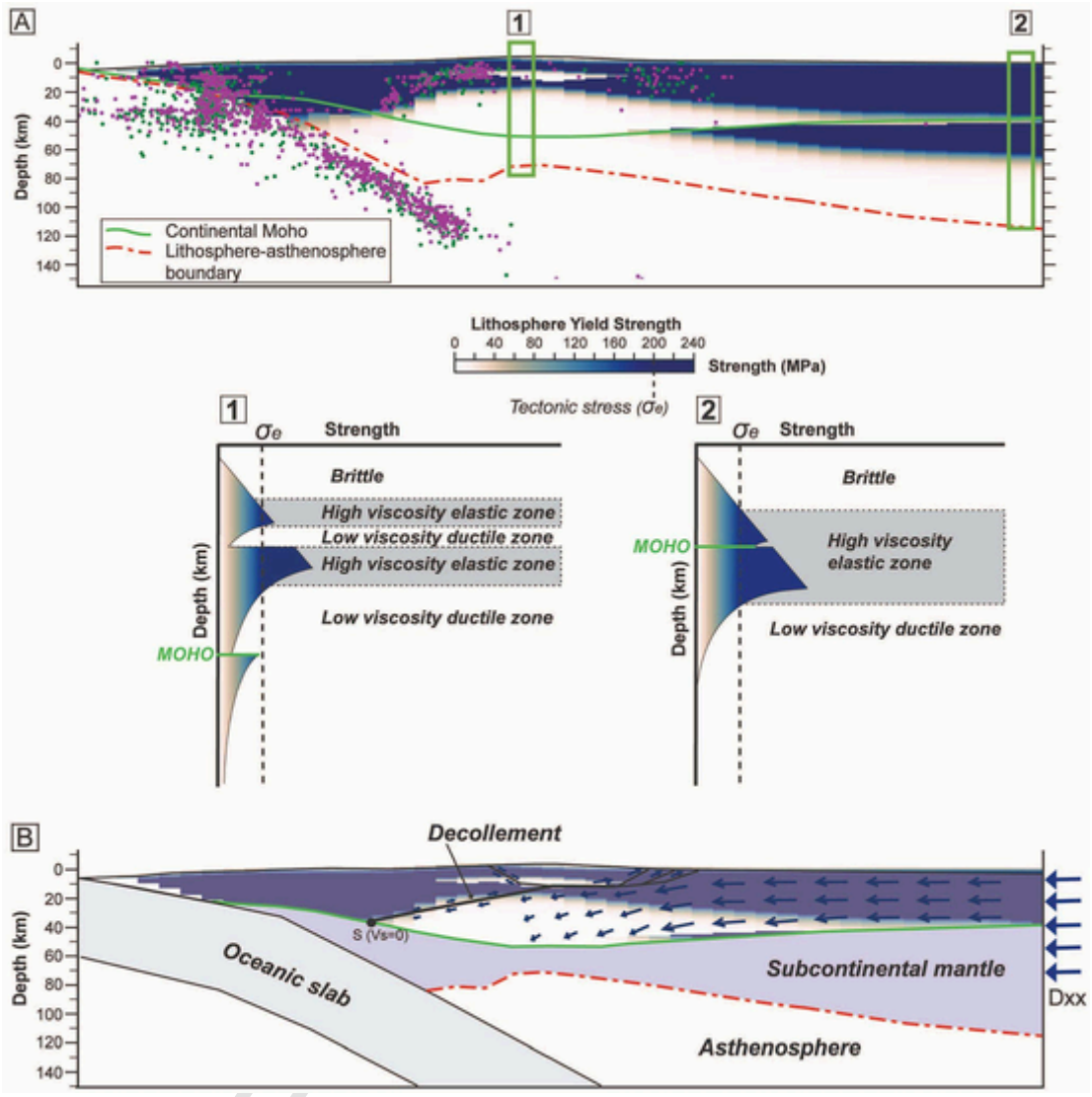

Fig. 10. A) Modeled thermomechanical structure, showing a rheologically-stratified lithosphere with contrasting high- and low-strength zones, in blue and red colors respectively, and schematic yield-strength envelopes for different sectors of the orogen: (1) the thickest sector of the orogen, characterized by the presence of a thin low-strength zone located in the upper crust, and (2) the continental shield characterized by mechanically-coupled crust and uppermost mantle. Areas with strength higher than the main tectonic stress (σ_e) are expected to behave elastically and transmit stresses, while areas with lower strength may deform either in a brittle (upper crust) or ductile (middle-to-lower crust) manner. Decollements are interpreted to be located inside the upper crustal low-strength zone, which presents a ductile behavior. B) Kinematic model, with thermomechanical constraints, proposed to construct the regional and balanced cross-sections. In this model, the crust is thickened by imposing a fixed subduction zone and assigning a westward motion of the continental plate towards the trench. (For interpretation of the references to colour in this figure legend, the reader is referred to the web version of this article.)

lished geological data described in section 3 and create or reactivate faults accordingly. This allows us to constrain the amount of shortening that we impose to the kinematic model. The final stages (the last 15 My of the model) consider the upper-middle crustal low-strength zone as a decollement zone.

An estimation of the crustal root thickness for each evolutionary stage is obtained from published paleo-crustal thicknesses and from our kinematic reconstruction of the different stages. The initial inferred crustal thickness and the area-balancing on a crustal-scale is used to explain the thickening of the crust by tectonic shortening, as has been proposed by previous models (Baby et al., 1997; Allmendinger and Gubbels, 1996; Allmendinger et al., 1997; Kley and Monaldi, 1998). We assign a velocity gradient between the continental plate and the fixed slab-forearc interface and apply a westward motion of the South American plate (Fig. 10B). This is achieved with an artificial line at the base of the Moho which has no geological significance and has been designed for the purpose of kinematical modeling (Supplementary Material 2). Displacement is transmitted along this base using the trishear algorithm until the singularity point S below the Cordilleran axis. At this point, shortening is transmitted to a ramp-flat master decollement, modeled with the fault parallel flow algorithm as a passive master fault.

Crustal material from the craton is gradually incorporated into the orogenic system, and this forms the crustal root. Consequently, this constructs topography by isostatic adjustments. In our models, the material is not lost by erosion at the subduction zone, neither by crustal delamination or by the movement of material along strike, nor is it gained by magmatic addition. Through this method, plain strain along the transects is assumed.

The incorporation of isostatic-flexural compensation for the added topographic load and crustal root after each modeled deformation step permits the creation of basin space and Moho adjustments. To achieve this, flexural-isostatic adjustments to the lithosphere due to local load changes are made, assuming a default value for the Young's modulus $E = 7 \times 10^{10}$ Pa and the effective elastic thickness (Te) calculated in

Tassara et al. (2007), Prezzi et al. (2009) and Ibarra et al. (2019, 2021). Our models produce enough foreland subsidence to accommodate the observed foreland stratigraphy.

4.3. Shortening estimation

We applied two approaches to estimate crustal shortening of each cross-section: forward modeling to reconstruct the observed surface structure, as explained in the previous section, and crustal area balance between initial and final crustal thicknesses. Regarding the cross-section reconstruction, we defined two end-member models for each initial crustal geometry, with a thinner or thicker initial crust according to published geological and geochemical data, and used a mean value in our kinematic modeling. This allows us to assign an error for each estimated crustal shortening (Table 1). The undeformed foreland thicknesses and Mesozoic rifting events are used to constrain the back-arc sector of the crust for the T0. For the second approach, we used crustal area balance between initial and final Moho geometries (C in Fig. 11), and the isostatic compensation of the Moho depth (red and violet dashed lines) due to the topographic load (A in Fig. 11) and sedimentation in the forearc and foreland basins (B in Fig. 11). To calculate the topographic load, we produced topographic swath profiles with a bin width of 10 km and used the mean elevation (Pérez-Peña et al., 2017). The flexural/isostatic compensation is calculated with the 2D Decompaction module from MOVE, using average densities of 2.4-2.6 g/cm^3, 2.6-2.8 g/cm^3 and 3.3 g/cm^3 for the sedimentary deposits, upper crust and mantle, respectively, and a Young's Modulus of 70 GPa.

The amounts of shortening, calculated with the reconstruction approach, are 4-15% lower than the crustal area balance approach (Table 1). This indicates that the estimations of shortening are conservative (Sheffels, 1990) and additional shortening, such as the internal strain of the basement blocks (McQuarrie and Davis, 2002), layer-parallel shortening (Yonkee and Weil, 2010) and/or strike-slip movement of crustal material along NW sinistral or NE dextral faults (Riller et al., 2012) must be considered. This difference in crustal shortening comparing both methods fall within the proposed range for magmatic addition (Lamb and Hoke, 1997; Haschke and Gunther, 2003; Carrapa et al., 2022). Nevertheless, if we consider the subduction erosion proposed for the southern study sector (33-36°S; Kay et al., 2005; Stern, 2020) shortening calculated by the crustal area balance should increase and may compensate for the magmatic addition.

Table 1
Maximum, media and minimum values of crustal thickness used in the forward model set up for each transect. A. Values of shortening (maximum, media and minimum) calculated from crustal area balance between initial and final crustal thicknesses. B. Values of shortening calculated from the forward-kinematic modeling. A vs B. Percentage of variation between A and B.

Latitude		Initial crustal thickness							**A** Shortening (km) (area)	error	**B** Shortening (km) (forward)	**A** vs **B**
22°S		CR	Domeyko	WC	Altiplano	EC	SA	foreland				
	maximum	32	53	48	46	43	35	33.5	258			
	media	32	47	43	42	39	35	33	325	± 67	285	14%
	minimum	32	40	38	38	35	35	32.5	392			
24°S		CR	Domeyko	WC	Puna	EC	SS	foreland				
	maximum	32	50	42	40	38	33	35	235			
	media	32	45	40	38	36	33	34.5	270	± 35	230	15%
	minimum	32	40	38	36	35	33	34	305			
27.6°S		CR	WFC	EFC	PRE-C	PR	foreland					
	maximum	24-33	33-50	40-44	40	39	35		194			
	media	24-32	32-40	38-42	38.5	38	35		214	± 20	194	9.5%
	minimum	24-31	31-30	35-40	37	37	35		234			
30°S		CR	PC	FC	PRE-C	PR	foreland					
	maximum	29-34	34-44	40-42	44	40	36		171			
	media	29-33.5	34-40	38-40	40	39	35-36		155	± 16	137	12%
	minimum	29-33	33-36	36-38	36	38	35		139			
32.4°S		CR	WPC	EPC	FC	PRE-C	foreland					
	maximum	24-31	31-38	34-35	34	34-35	37-39		116			
	media	24-30	30-36	33-35	33-34	34	37-38		104	± 12	94	10%
	minimum	24-29	29-34	32-34	33	33-34	36-38		92			
33.6°S		CR	WPC	EPC	FC	foreland						
	maximum	26-34	36-40	35	35-37	35-37			65			
	media	26-34	34-40	35	35	35-36			73	± 9	69	5%
	minimum	26-34	34-38	34	34-35	34-36			82			
35°S		CR	WPC	EPC	foreland							
	maximum	36-38	37-35	35-36	36-40				39			
	media	35-36	35-33	34-35	35-39				46	± 8	44	4%
	minimum	33-34	32-34	33-34	35-38				54			

CR, Coastal Range
WC, Western Cordillera
PC, Principal Cordillera
WPC, Western Principal Cordillera
EPC, Eastern Principal Cordillera
EC, Eastern Cordillera
FC, Frontal Cordillera
WFC, Western Frontal Cordillera
EFC, Eastern Frontal Cordillera
SS, Subandean Ranges
Pre-C, Precordillera
PR, Pampean Ranges

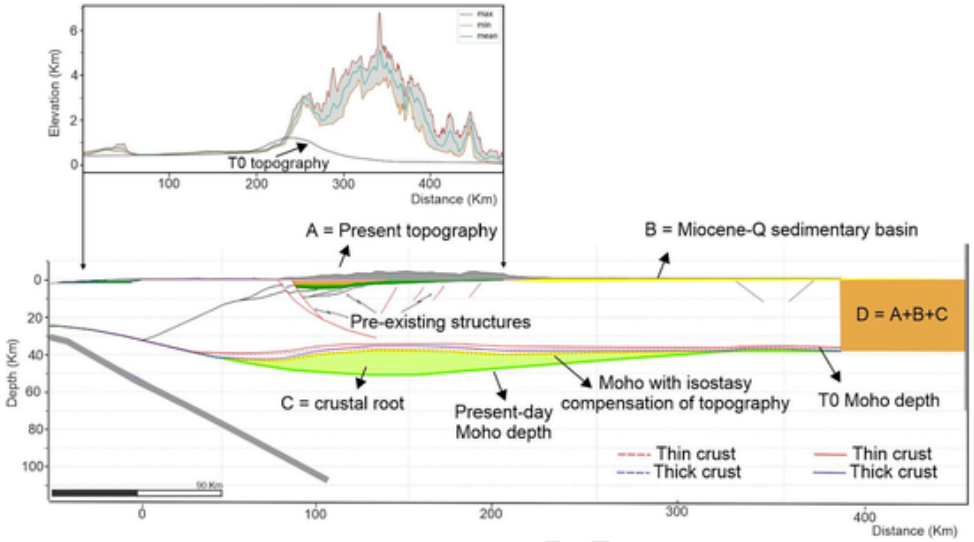

Fig. 11. Shortening estimation by applying two-end models of initial crustal thickness: thin crust in red, thick crust in blue (full line for the pre-isostatic compensation of actual topography, dashed line for the compensated Moho). Topography for the T0 is estimated by assuming isostatic compensation of the crust. The crustal material that is incorporated into the orogenic system from the east (orange rectangle) is equal to the area of the crustal root (in light green), the area between the Present (upper diagram) and T0 topography (in grey), after flexural/isostatic compensation, and the area filled with Cenozoic sedimentary basin deposits (in yellow), after flexural/isostatic compensations. (For interpretation of the references to colour in this figure legend, the reader is referred to the web version of this article.)

4.4. Geodynamic modeling of the upper-plate lithospheric shortening

To evaluate how the thermomechanical structure of the crust evolves during the different stages of crustal shortening and uplift, we developed a general 2D geodynamic model of upper-plate lithospheric shortening by using the geodynamic code ASPECT (Advanced Solver for Problems in Earth's ConvecTion; Bangerth et al., 2019). As we focus on the evolution of crustal deformation within the South American plate, we simply simulate the dynamics of shortening from the forearc to the foreland and neglect the subduction process to the west. This setup depicts a general and simple lithospheric structure, without considering lateral variations of material properties and the particular features of each transect.

The resolution of the 2D model domain (Fig. 12) is 500 m per element in the lithosphere at 0–100 km depth and 7 km at 100–240 km depth. This variable resolution allows saving computational time while ensures a refined depiction of the lithospheric deformation pattern. Regarding the model geometry and parameters, we modified the initial setup presented in Barrionuevo et al. (2021; for more details see Supplementary Material 3). In particular, the lithospheric structure corresponds to the aforementioned thermomechanical structure under the Central Andes (Fig. 10), with a thicker zone in the westernmost part, corresponding to the forearc.

The continental lithosphere is divided into three layers with different rock properties, which are based on laboratory-derived rheological parameters used in previous numerical studies (e.g., Liu and Currie, 2016; Supplementary Material 3). The continental crust is between 35 and 40 km thick and the maximum depth of the LAB is 100 km. The upper continental crust (CUC) has a wet Black Hills quartzite rheology (Gleason and Tullis, 1995). The lower crust (CLC) uses the same rheology as the upper crust but is five times stronger than the wet quartzite,

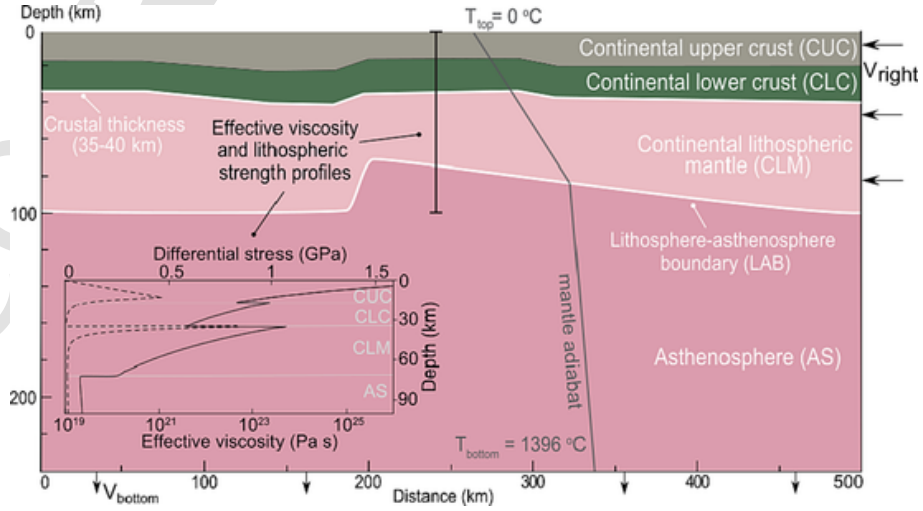

Fig. 12. Geodynamic initial model setup. Material flows in from the lithosphere at the right-hand boundary (Vright) and flows out from the bottom boundary (Vbottom) to maintain mass balance, which is used to simulate lithospheric shortening. The diagram shows an example of the initial effective viscosity (black solid line) and lithospheric strength (black dashed line) profiles from the surface to 100 km depth calculated using the initial thermal structure (grey line) and a strain rate of 10^{-15} s^{-1}. Note that strain rate varies during model evolution. Material parameters are given in Supplementary Material 3.

assuming that it is drier and less silicic. The continental lithospheric mantle (CLM) is represented by dry olivine; and the Asthenosphere (AS) corresponds to wet olivine with constant water content (Hirth and Kohlstedt, 2003).

The top boundary condition is zero traction with a 10-km-thick sticky air layer. This weak and light layer is used to approximate the free surface in a way that allows the formation and evolution of the faulting on the surface. To drive lithospheric shortening, we imposed a constant horizontal shortening rate of 1 cm/yr along the lithosphere at the right-hand boundary, which is an average estimate for the Central Andes from the late Cenozoic (Oncken et al., 2006). We added a small outflux velocity to the bottom boundary to maintain the mass balance. The temperature remains at 0 °C at the surface and 1396 °C at the bottom. The initial temperature increases linearly from the surface to the bottom of the lithosphere and then adiabatically between the lithosphere-asthenosphere boundary and the bottom of the model (Fig. 12). The side boundaries have conductive geotherms and no horizontal heat flux.

5. Results

5.1. Thermomechanical structure

The output model is an assembly of 1D vertical yield strength profiles distributed across each of the seven E-W studied transects with a resolution of 0.2° in longitude, which allows us to predict the strength layering inside the upper plate (as in Fig. 10A). The results show that, in the continental shield (column 2 in Fig. 10), a cold and strong crust is mechanically coupled with the mantle, while in the thermally-weakened arc region (column 1 in Fig. 10), the mantle and thick lower crust have no strength presenting a ductile behavior and rigidity is only concentrated in the colder mid-upper crust. The model also shows localized sub-horizontal low-strength zones inside the dominantly rigid upper crust, which we propose may act as decollements where crustal faults are rooted. The westward-dipping and sharp rheologic contrast between the rigid forearc and ductile orogenic lower-crust may act as a ramp for these decollements as has been already proposed (Tassara, 2005; Farías et al., 2010; Giambiagi et al., 2015a; Comte et al., 2019).

For each of our studied transects, Fig. 13A shows the temperature distribution inside the upper plate that is produced by our model and compares the modeled surface heat flow against available measurements compiled from the literature. This comparison demonstrates that, despite the simplicity of our analytical formulation of the thermal regime in a subduction environment, the model is able to reproduce the observed heat flow sufficiently well and can be considered a valid representation of the temperature field for each transect. The rheological-mechanical structure of the transects in Fig. 13B show that most of the upper-middle crust has a brittle-elastic behavior, particularly for the cold and rigid forearc and foreland regions, and a ductile behavior below the thermally-weakened arc region. However, in the Altiplano/Puna transects, a ductile behavior is also predicted by the model below the Western Cordillera, Eastern Cordillera and Sub-andean ranges, within a thin layer (< 7 km) at mid-crustal depths (5-15 km), as well as for the entire middle and lower crust zone (i.e., deeper than 7 km) below the Altiplano/Puna plateau and the western sector of the Eastern Cordillera. This upper-crust ductile layer is also observed in the normal subduction segments below Principal and Frontal Cordilleras, and it is mostly controlled by the existence of a relatively shallow LAB underneath the orogenic axis.

The flat-slab domain (30° and 32.4°S transects) is characterized by a relatively shallow subduction angle (Cahill and Isacks, 1992; Tassara and Echaurren, 2012) and a lack of active arc-related magmatism, resulting from the eastward migration of the asthenospheric wedge (Pilger, 1981; Kay et al., 1988). Here, the thermomechanical model suggests that the upper crustal low-strength layer is rather thin, due to the cold flat-slab thermal structure implied by a deep LAB (Fig. 13).

As has been mentioned above, the roof of the low-strength zones in the upper and lower crust are controlled in our thermomechanical model respectively by the depth to the 250° and 550 °C isotherms. In the Supplementary Material 1, we present a sensitivity analysis for each transect showing how the depth to these isotherms vary with possible changes of H_0 (±2 μW/m3), k (±1.5 W/m°K) and T_p (±250 °C) around their selected mean values (Table A.1 in Supplementary Material 1). For both isotherms, the effect of changing k and H_0 is much larger than changes in T_p, mostly for regions of thick upper crust. The shallower 250 °C isotherm is less sensitive to these changes than the deeper 550 °C isotherm. For those particular regions where the base of the upper crust is deeper than the 250 °C (delimiting shallow low-strength zones), we can conclude that the applied changes in thermal parameters imply maximum variations in the depth to the 250 °C of ±5 km. Moreover, even in the coolest models (i.e., lowest values of H_0 and T_p, highest value of k), this isotherm is still shallower than the base of the upper crust, implying that the shallow low-strength zones are a robust feature of our model. The position for the roof of the deeper low-strength zone is less well constrained since the 550 °C isotherm can exhibit variations of ±10 km around the mean depth.

This sensitivity analysis is also useful for discussing the possible effect that uncertainties in the depth of the LAB could have in the derived thermomechanical structure. In the conceptual framework of our thermal model, the LAB depth plays the primary role in controlling the thermal structure of the conductive lithosphere in the eastern part (arc and backarc region) of the cross sections. The commonly smooth geometry of the LAB in the model of Tassara and Echaurren (2012) is loosely constrained by available S-wave seismic tomographies at the time of publication (Feng et al., 2004, 2007), measured surface heat flow and the weak gravity effect of the relatively small density anomaly between lithospheric and asthenospheric mantle. Seismic images of the LAB published after Tassara and Echaurren (2012) along the Andean margin are scarce and mostly based on S-wave receiver functions (i.e., Ammirati et al., 2013; Heit et al., 2014; Haddon and Porter, 2018). They show a general coincidence with the LAB geometry used by us, although some differences up to ±15 km could locally exist underneath the Altiplano-Puna plateau and Pampean Ranges. Changes in LAB depth for a given value of T_p are identical to changes in T_p for a given LAB depth. Particularly, the explored changes of ±250 °C in T_p along a typical continental geotherm at mantle depths are identical to variations of the order of ±20 km in the LAB depth. Such variations are larger than differences between seismically constrained LAB models and the one used by us, and therefore they contribute with an uncertainty of less than ±2.5 km in the depth of the 250 °C isotherm and ± 5 km for the 550 °C isotherm. This implies that possible local-scale errors in the used geometry of the LAB with respect to seismic models would have a minor effect on the resulting thermomechanical structure of each transect.

We must recall that our thermal model is fully based on a steady-state conductive geotherm. For the forearc, the analytical formulation of Molnar and England (1990) does include the effect of heat advection by the subducted slab, but our model does not incorporate advective contributions associated to the motion of crustal material due to backarc shortening (as done for instance by Springer, 1999) or by magma and/or fluid injection underneath the magmatic arc. In this sense, this can be considered a reference conductive thermal model and we recognize that in the case of an interconnected crustal-scale magmatic plumbing systems like those envisaged by several authors (i.e., Cashman et al., 2017; Burchardt et al., 2022) the temperature at upper crustal levels can be largely augmented with respect to the conductive reference. This can actually be the reason behind a slightly reduced heat flow predicted by our model when compared against measurements near the active volcanic arc in Fig. 13A. In this scenario, the effect on the rheological stratification of the upper crust would be likely

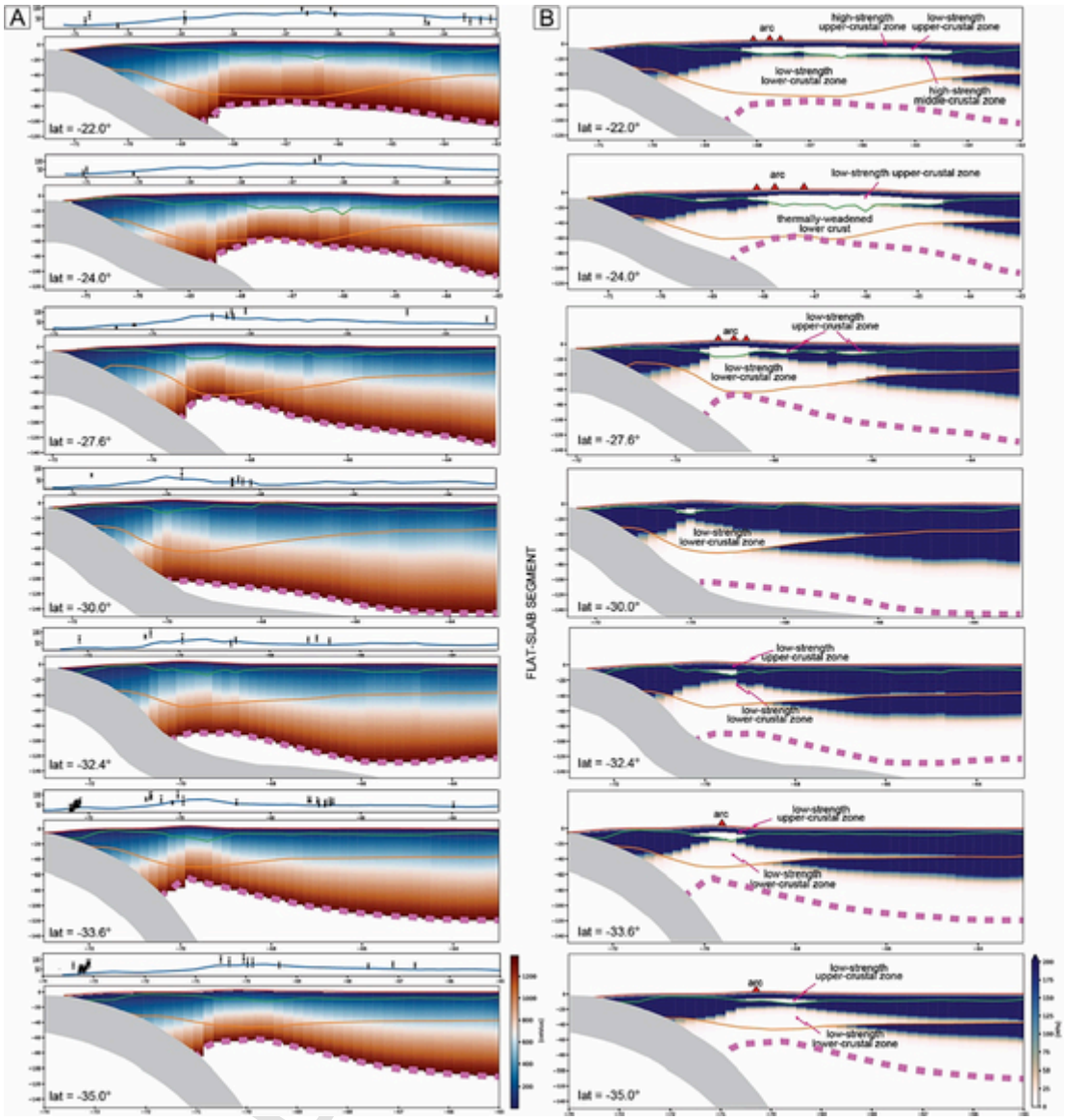

Fig. 13. Thermal (A) and mechanical (B) structure resulting from the analytical model. For each of the seven modeled transects (see latitude at the bottom left corner), panel A shows the temperature distribution inside the upper plate (see color scheme at the right hand of the 35°S transect). Upper insets above each transect compares the surface heat flow resulting from the model (continuous blue line) with measured values and their uncertainties (in mW/m2) as compiled from the literature (Yamano and Uyeda, 1990; Uyeda and Watanabe, 1982; Henry and Pollack, 1988; Hamza and Muñoz, 1996; Bialas and Kukowski, 2000; Muñoz and Hamza, 1993; Grevemeyer et al., 2003, 2005, 2006; Kudrass et al., 1995; Springer and Förster, 1998; Hamza et al., 2005; Flueh and Grevemeyer, 2005; Collo et al., 2018). Panel B shows the derived strength layering inside the overriding upper plate. Colors indicate yield strength (see color scheme at the right hand of the 35°S transect) showing strong regions (high-strength layers) in blue-green and weak zones (low-strength layers) in brownish-to-white colors. In both panels the continuous green and red lines mark respectively the geometry of the Intracrustal Density Discontinuity (ICD) and Moho, dashed purple line is the Lithosphere-Asthenosphere Boundary (LAB) and the gray area is the subducted slab, which geometries are from Tassara and Echaurren (2012). Vertical exaggeration x1.5. (For interpretation of the references to colour in this figure legend, the reader is referred to the web version of this article.)

similar to what our sensitivity tests show when increasing H_0 and T_p or reducing k, which produce a shallowing of the roof of the upper crustal low strength zone by some kilometers.

5.2. Kinematic models with thermomechanical constraints

In the following, we describe the structural forward modeling that results in the present configuration constrained by the thermomechanical models. We describe the main deformational events in different crustal domains that constraint the activity of different decollements. Data of this section are summarized in Table 2 and in Supplementary Material 2.

5.2.1. The Altiplano transect (22°S)

The Altiplano (22°S) is modeled with two decollements, the Altiplano/Puna (APD), and the Main Andean (MAD), in agreement with previously proposed models suggesting a complete disconnection between main deep structures (Elger et al., 2005; Martinod et al., 2020). We configure the time zero (**T0**, >45 Ma, Fig. 14) with a previous contraction in the proto-Domeyko Range and strike-slip movement along the Atacama fault system. We model the first stage **T1** (45-40 Ma) with movement along the APD associated with 35 km of shortening distributed between the Domeyko Range and the Khenayani-Uyuni fault system in Western Cordillera. The proto-Eastern Cordillera is deformed by east-directed faults. The APD is located below the plateau, at a depth between 8 and 18 km, and is connected at depth with a west-dipping

Table 2 (*continued*)

Summary of the phases of construction of the transects analyzed in the Southern Central Andes and the associated crustal shortening (Sh) and thickening (Zm) for every step of the forward modeling. Numbers next to the foreland basins correspond to the studies of: 1) Elger et al., 2005; 2) Uba et al., 2006; 3) Alonso, 1992; Carrapa and DeCelles, 2008; 4) Siks and Horton, 2011; Pingel et al., 2019; 5) Carrapa et al., 2008; 6) Dávila et al., 2012; 7) Beer et al., 1990; Re et al., 2003; Ruskin and Jordan, 2007; Fosdick et al., 2017; 8) Reat and Fosdick, 2018; Mardones et al., 2021; 9) Richard, 2020; 10) Giambiagi et al., 2003; Porras et al., 2016; 11) Buelow et al., 2018; 12) Horton et al., 2016.

Transect	Phase	Time (Ma)	Active decollement	Deformed morphostructural units	Sh (km)	Zm (km)	Foreland basin thickness (m)
Altiplano 22°S	T1	45 - 40	Altiplano - Puna	*Domeyko Range, Western and Eastern Cordilleras*	35	53	1000
	T2	40 - 35	Altiplano - Puna	*Western Cordillera, Altiplano*	50	58	2000
	T3	35 - 30	Altiplano - Puna, Main Andean	*Altiplano, Western and Eastern Cordillera*	40	63	3000 (Lípez basin)
	T4	30 - 21	Main Andean	*Eastern Cordillera*	30	67	4200 (Lípez basin) (1) (2)
	T5	21 - 14	Main Andean	*Eastern Cordillera*	55	70	5000 (Lípez basin) 250 (Chaco basin)
	T6	14 - 7	Main Andean	*Eastern Cordillera, Sub Andean ranges*	55	71	5500 (Lípez basin) 750 (Chaco basin)
	T7	7 - 0	Main Andean	*Sub Andean ranges*	60	73	6000 (Chaco basin)
				TOTAL SHORTENING	**325**		
Puna 24°S	T1	45 - 40	—	*Domeyko Range*	30	52	1500
	T2	40 - 35	Altiplano - Puna	*Domeyko Range, Puna, Eastern Cordillera*	45	55	2000 (Pastos Grandes basin) 400 (Humahuaca/ Cianzo basin)
	T3	35 - 30	Altiplano - Puna	*Puna, Eastern Cordillera*	30	60	
	T4	30 - 21	Altiplano - Puna	*Eastern Cordillera*	30	61	3000 (Pastos Grandes basin) 1800 (Humahuaca/ Cianzo basin)
	T5	21 - 14	Altiplano - Puna Main Andean	*Domeyko Range, Puna, Eastern Cordillera*	45	63	3100 (Humahuaca/ Cianzo basin)
	T6	14 - 7	Main Andean	*Eastern Cordillera*	50	63	4300 (Pastos Grandes basin) 5000 (Humahuaca/ Cianzo basin)
	T7	7 - 0	Main Andean	*Santa Barbara system*	40	63	4500 (Pastos Grandes basin) (3) 6000 (Humahuaca/ Cianzo basin) (4)
				TOTAL SHORTENING	**270**		
Southern-most Puna 27.6°S	T1	45 - 38	Frontal Cordillera	*Frontal Cordillera, Pampean Ranges*	49	46	
	T2	38 - 23	Frontal Cordillera	*Frontal Cordillera, Pampean Ranges*	30	49	
	T3	23 - 15	Frontal Cordillera, Eastern Main	*Frontal Cordillera*	50	56	1400 (Fiambalá basin)
	T4	15 - 10	Eastern Main	*Frontal Cordillera, Pampean Ranges*	40	62	3700 (Fiambalá basin) 1000 (Pipanaco basin)
	T5	10 - 5	Eastern Main, Pampean Ranges	*Pampean Ranges*	32	63	4700 (Fiambalá basin) 2000 (Pipanaco basin)
	T6	5 - 0	Pampean Ranges	*Pampean Ranges*	24	63	5700 (Fiambalá basin) 3500 (Pipanaco basin)
				TOTAL SHORTENING	**225**		(5) (6)
Flat slab 30°S	T1	45 - 30	—	*Principal and Frontal Cordillera*	38	48	800 50
	T2	30 - 20	—		-3	50	150
	T3	20 - 15	Frontal Cordillera	*Frontal Cordillera*	40	58	2200 (Rodeo basin) 650 (Bermejo basin)
	T4	15 - 12	Frontal Cordillera, Precordillera	*Frontal Cordillera, Precordillera*	20	64	2600 (Rodeo basin) 1800 (Bermejo basin)
	T5	12 - 8	Precordillera	*Precordillera, Pampean Ranges*	22	65	3100 (Rodeo basin) 2950 (Bermejo basin)
	T6	8 - 5	Precordillera	*Precordillera, Pampean Ranges*	17	66	3500 (Rodeo basin) 5500 (Bermejo basin)
	T7	5 - 0	Pampean Ranges	*Precordillera, Pampean Ranges*	21	66	(7) (8)
				TOTAL SHORTENING	**155**		
Aconcagua 32.4°S	T1	21 - 18	—	*Principal Cordillera*	17	42	100
	T2	18 - 15	Principal Cordillera	*Principal and Frontal Cordillera*	20	50	700 (Cacheuta basin)
	T3	15 - 12	Principal Cordillera	*Principal and Frontal Cordillera*	17	52	1400 (Cacheuta basin)
	T4	12 - 9	Principal Cordillera, Frontal Cordillera	*Principal and Frontal Cordillera, Precordillera*	14	52	1800 (Cacheuta basin)
	T5	9 - 6	Frontal Cordillera	*Precordillera*	13	52	2600 (Cacheuta basin)
	T6	6 - 3	Frontal Cordillera	*Precordillera*	12	52	3500 (Cacheuta basin)
	T7	3 - 0	Frontal Cordillera	*Precordillera, Pampean Ranges*	11	52	4700 (Cacheuta basin) (9)
				TOTAL SHORTENING	**104**		
Maipo/ Tunuyán 33.6°S	T1	21 - 18	—	*Principal Cordillera, Coastal Ranges*	8	44	(10) 200 (11)
	T2	18 - 15	—	*Principal and Frontal Cordilleras*	10	47	100 (Tunuyán basin) 650 (Cacheuta basin)
	T3	15 - 12	Principal Cordillera	*Principal Cordillera*	17	49	1000 (Tunuyán basin) 1200 (Cacheuta basin)
	T4	12 - 9	Principal Cordillera, Frontal Cordillera	*Principal and Frontal Cordilleras*	15	51	1400 (Tunuyán basin) 1800 (Cacheuta basin)
	T5	9 - 6	Principal Cordillera Frontal Cordillera	*Principal and Frontal Cordilleras*	12	51	1800 (Tunuyán basin) 2100 (Cacheuta basin)
	T6	6 - 3	Frontal Cordillera	*Frontal Cordillera*	6	51	2400 (Cacheuta basin)
	T7	3 - 0	Frontal Cordillera	*Frontal Cordillera*	5	51	2800 (Cacheuta basin)
				TOTAL SHORTENING	**73**		
Tinguiririca/ Malargue 35°S	T1	16 - 13	Main	*Principal Cordillera*	9	44	400 (Malargue basin) (12)
	T2	13 - 10	Main	*Principal Cordillera*	9	46	800 (Malargue basin)
	T3	10 - 6	Main	*Principal Cordillera*	12	47	800 (Malargue basin)
	T4	6 - 3	Main	*Principal Cordillera*	8	48	500 (Malargue basin)
	T5	3 - 0	Main	*Principal Cordillera*	8	48	2500 (Malargue basin)
				TOTAL SHORTENING	**46**		

Transect	Phase	Time (Ma)	Active decollement	Deformed morphostructural units	Sh (km)	Zm (km)	Foreland basin thickness (m)
Altiplano 22°S	T1	45 - 40	Altiplano - Puna	Domeyko Range, Western and Eastern Cordilleras	35	53	1000
	T2	40 - 35	Altiplano - Puna	Western Cordillera, Altiplano	50	58	2000
	T3	35 - 30	Altiplano - Puna, Main Andean	Altiplano, Western and Eastern Cordillera	40	63	3000 Lípez basin
	T4	30 - 21	Main Andean	Eastern Cordillera	30	67	4200 Lípez basin (1) (2)
	T5	21 - 14	Main Andean	Eastern Cordillera	55	70	5000 250 Chaco basin
	T6	14 - 7	Main Andean	Eastern Cordillera, Sub Andean ranges	55	71	5500 750 Chaco basin
	T7	7 - 0	Main Andean	Sub Andean ranges	60	73	6000 Chaco basin
				TOTAL SHORTENING	325		
Puna 24°S	T1	45 - 40	—	Domeyko Range	30	52	1500
	T2	40 - 35	Altiplano - Puna	Domeyko Range, Puna, Eastern Cordillera	45	55	2000 Pastos Grandes basin 400 Humahuaca/ Cianzo basin
	T3	35 - 30	Altiplano - Puna	Puna, Eastern Cordillera	30	60	Pastos Grandes basin Humahuaca/ Cianzo basin
	T4	30 - 21	Altiplano - Puna	Eastern Cordillera	30	61	3000 Pastos Grandes basin 1800 Humahuaca/ Cianzo basin
	T5	21 - 14	Altiplano - Puna Main Andean	Domeyko Range, Puna, Eastern Cordillera	45	63	Pastos Grandes basin 3100 Humahuaca/ Cianzo basin
	T6	14 - 7	Main Andean	Eastern Cordillera	50	63	4300 Pastos Grandes basin 5000 Humahuaca/ Cianzo basin
	T7	7 - 0	Main Andean	Santa Barbara system	40	63	4500 Pastos Grandes basin 6000 Humahuaca/ Cianzo basin (3) (4)
				TOTAL SHORTENING	270		
Southern-most Puna 27.6°S	T1	45 - 38	Frontal Cordillera	Frontal Cordillera, Pampean Ranges	49	46	
	T2	38 - 23	Frontal Cordillera	Frontal Cordillera, Pampean Ranges	30	49	
	T3	23 - 15	Frontal Cordillera, Eastern Main	Frontal Cordillera	50	56	1400 Fiambalá basin Pipinaco basin
	T4	15 - 10	Eastern Main	Frontal Cordillera, Pampean Ranges	40	62	3700 1000 Pipinaco basin
	T5	10 - 5	Eastern Main, Pampean Ranges	Pampean Ranges	32	63	4700 2000 Pipinaco basin
	T6	5 - 0	Pampean Ranges	Pampean Ranges	24	63	5700 Fiambalá basin 3500 Pipinaco basin (5) (6)
				TOTAL SHORTENING	225		
Flat slab 30°S	T1	45 - 30	—	Principal and Frontal Cordillera	38	48	800 50
	T2	30 - 20	—		-3	50	Rodeo basin 150 Bermejo basin
	T3	20 - 15	Frontal Cordillera	Frontal Cordillera	40	58	2200 Rodeo basin 650 Bermejo basin
	T4	15 - 12	Frontal Cordillera, Precordillera	Frontal Cordillera, Precordillera	20	64	2600 Rodeo basin 1800 Bermejo basin
	T5	12 - 8	Precordillera	Precordillera, Pampean Ranges	22	65	3100 Rodeo basin 2950 Bermejo basin
	T6	8 - 5	Precordillera	Precordillera, Pampean Ranges	17	66	3500 5500 Bermejo basin
	T7	5 - 0	Pampean Ranges	Precordillera, Pampean Ranges	21	66	(7) (8)
				TOTAL SHORTENING	155		
Aconcagua 32.4°S	T1	21 - 18	—	Principal Cordillera	17	42	100
	T2	18 - 15	Principal Cordillera	Principal and Frontal Cordillera	20	50	700 Cacheuta basin
	T3	15 - 12	Principal Cordillera	Principal and Frontal Cordillera	17	52	1400 Cacheuta basin
	T4	12 - 9	Principal Cordillera, Frontal Cordillera	Principal and Frontal Cordillera, Precordillera	14	52	1800 Cacheuta basin
	T5	9 - 6	Frontal Cordillera	Precordillera	13	52	2600 Cacheuta basin
	T6	6 - 3	Frontal Cordillera	Precordillera	12	52	3500 Cacheuta basin
	T7	3 - 0	Frontal Cordillera	Precordillera, Pampean Ranges	11	52	4700 Cacheuta basin (9)
				TOTAL SHORTENING	104		
Maipo/ Tunuyán 33.6°S	T1	21 - 18	—	Principal Cordillera, Coastal Ranges	8	44	(10) 200 (11)
	T2	18 - 15	—	Principal and Frontal Cordilleras	10	47	100 Tunuyán basin 650 Cacheuta basin
	T3	15 - 12	Principal Cordillera	Principal Cordillera	17	49	1000 Tunuyán basin 1200 Cacheuta basin
	T4	12 - 9	Principal Cordillera, Frontal Cordillera	Principal and Frontal Cordilleras	15	51	1400 Tunuyán basin 1800 Cacheuta basin
	T5	9 - 6	Principal Cordillera Frontal Cordillera	Principal and Frontal Cordilleras	12	51	1800 Tunuyán basin 2100 Cacheuta basin
	T6	6 - 3	Frontal Cordillera	Frontal Cordillera	6	51	2400 Cacheuta basin
	T7	3 - 0	Frontal Cordillera	Frontal Cordillera	5	51	2800 Cacheuta basin
				TOTAL SHORTENING	73		
Tinguiririca/ Malargue 35°S	T1	16 - 13	Main	Principal Cordillera	9	44	400 Malargue basin (12)
	T2	13 - 10	Main	Principal Cordillera	9	46	800 Malargue basin
	T3	10 - 6	Main	Principal Cordillera	12	47	800 Malargue basin
	T4	6 - 3	Main	Principal Cordillera	8	48	500 Malargue basin
	T5	3 - 0	Main	Principal Cordillera	8	48	2500 Malargue basin
				TOTAL SHORTENING	46		

(10° to 20°) shear zone, previously highlighted by the ANCORP project (Oncken et al., 2003). Flexural subsidence is generated in Calama and Lipez basins.

During the next stage (**T2**, 40-35 Ma), 50 km of shortening is focused on the Western Cordillera, the easternmost Altiplano and the Eastern Cordillera. The Domeyko Range becomes affected by dextral strike-slip faults, such as the West Fault, but it is passively uplifted by the ramp of the APD decollement. Flexural subsidence is generated in the Lípez basin and the foredeep basins during **T2** and **T3** (35 to 30 Ma), resulting from the uplift of the Western Cordillera, Eastern Cordillera and central Altiplano. During **T3**, the West Fault system changed its strike-slip movement from dextral to sinistral, while deformation of the western Eastern Cordillera propagated westward together with the development of the Main Andean decollement (MAD). Our thermomechanical model suggests that the MAD extends westward, below the Eastern Cordillera, where a sharp contact between high and low strength zones exists. In our kinematic model, we extend this decollement toward the west, until 66.3°W and 65.9°W, in the Altiplano and Puna transects, respectively, where it roots into a ductile shear zone. This zone is a low-strength zone that reaches shallow depths below the Western Cordillera, Altiplano/Puna and Eastern Cordillera, and includes the mid-crustal zone of low-seismic velocity, called the Altiplano Low Velocity Zone by Yuan et al. (2002).

Between 30 and 21 Ma, **T4** stage, extensional deformation is localized in the Calama and Salar de Atacama basins, associated with a sinistral/normal movement of the West Fault system. Contractional defor-

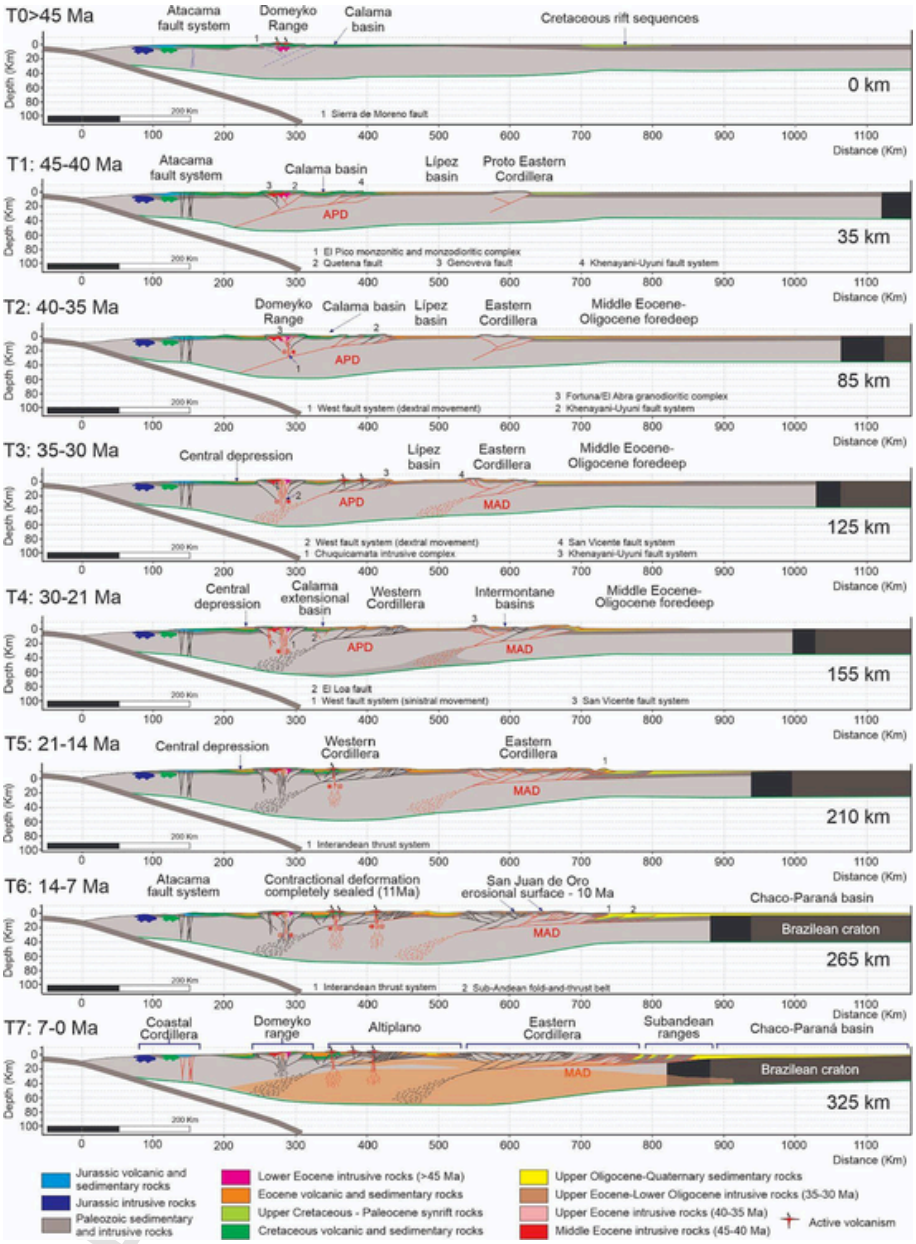

Fig. 14. Forward modeling of the Altiplano transect (22°S). Time 0 has been set to pre-45 Ma. By this time, deformation has been focused only in the Domeyko Range. During the next stages (T1 to T7), the crust is shortened by incorporating the equivalent of the crustal area (in black) into the crustal root, while the subduction zone is fixed. The length of the black area indicates the amount of crustal shortening achieved in each stage, calculated from the kinematic forward modeling +14% (14% is the difference between the crustal area balance and the kinematic forward modeling shortening estimates, see Table 1). APD: Altiplano/Puna decollement, and MAD: Main Andean decollement. Red and black lines indicate active and inactive faults, respectively. Orange color in T7 indicates low-strength zones according to the thermomechanical model. (For interpretation of the references to colour in this figure legend, the reader is referred to the web version of this article.)

mation is focused only on the Eastern Cordillera, achieving 35 km of shortening.

During stage **T5** (21-14 Ma), 55 km of shortening are accommodated along the MAD, associated with deformation and main exhumation of the Eastern Cordillera. The Khenayani-Uyuni fault system gets deactivated, and regional strike-slip faults crosscut the previous thrusts. During stage **T6** (14-7 Ma), deformation concentrated along the eastern sector of the MAD, below the eastern part of the Eastern Cordillera and the Sub-Andean ranges, which absorbs ~55 km of shortening. Flexural subsidence is created in the Chaco-Paraná foreland basin starting at 12.4 Ma.

During the last stage **T7** (7-0 Ma), the Sub-Andean belt is modelled as a thin-skinned fold-and-thrust belt connected to a shallow-dipping decollement at 8-14 km depth, with 60 km of shortening focused in the eastern segment of the MAD.

5.2.2. *The Puna transect (24°S)*

For the time zero (**T0**, Fig. 15), we model the inversion of the Mesozoic Domeyko basin, the Salar de Atacama/Salar de Punta Negra foreland basin. This inversion generates a thick crust below the Domeyko Range (40 to 45 km), while a thinner than normal crust is present below the actual Santa Bárbara range as a result of the Cretaceous Salta rift.

During the next step (**T1**, 45-40 Ma), the Domeyko system and the westernmost Western Cordillera are shortened 30 km and the foredeep basin subsides 1500 m. During **T2** (40-35 Ma), 45 km of shortening is

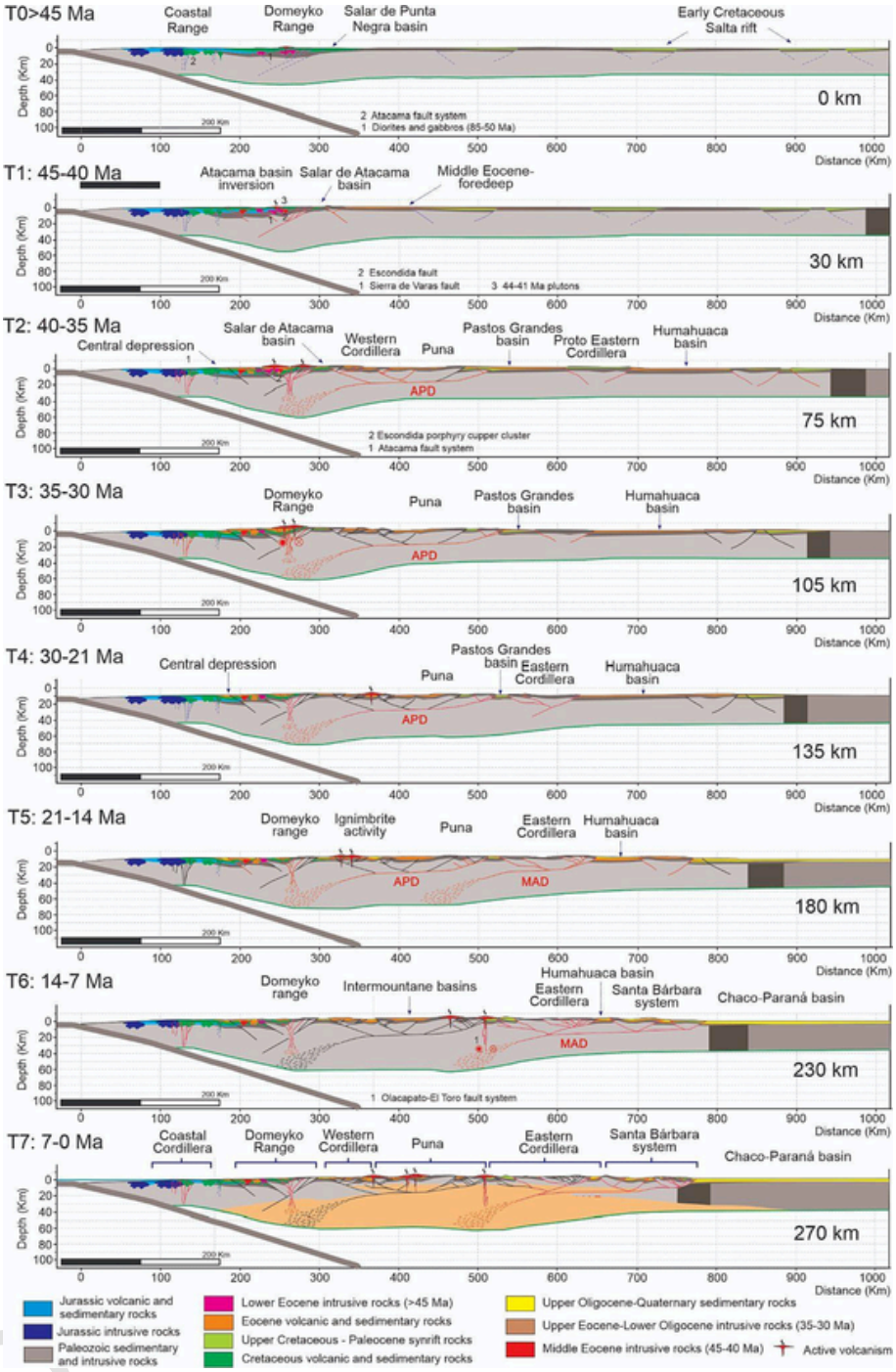

Fig. 15. Forward modeling of the Puna transect (24°S). Time T0 has been set to pre-45 Ma. By this time, deformation has been focused only in the Domeyko Range. Pre-existing faults are in dashed violet lines. During the next stages (T1 to T7), the crust is shortened by incorporating the equivalent of the crustal area (in black) into the crustal root, while the subduction zone is fixed. The length of the black area indicates the amount of crustal shortening achieved in each stage, calculated from the kinematic forward modeling +15% (15% is the difference between the crustal area balance and the kinematic forward modeling shortening estimates, see Table 1). APD: Altiplano/Puna decollement, MAD: Main Andean decollement. COT: Calama-Olacapato-El Toro fault system. Red and black lines indicate active and inactive faults, respectively. Orange color in T7 indicates low-strength zones according to the thermomechanical model. (For interpretation of the references to colour in this figure legend, the reader is referred to the web version of this article.)

focused on the eastern Domeyko Range, Western Cordillera and the proto-Puna. The Puna is deformed with east-directed thrusts and west-directed back-thrusts rooted into the APD. At the end of this stage, strike-slip faults affect the Domeyko Range.

The first uplift of the Eastern Cordillera is modeled with the reactivation of pre-existing faults, during T2, which generate flexural subsidence in delimiting basins such as Salinas Grandes and Humahuaca basins. During **T3** (35-28 Ma), the APD propagates eastward with deformation concentrated in the eastern Puna. During this stage, the crust achieves its maximum thickness below the Domeyko system, and the crustal root expands laterally towards the east.

During **T4** (28-21 Ma), 35 km of shortening is focused on the easternmost Puna and Eastern Cordillera. During the next stage (**T5**, 21-14 Ma), there is an eastward shift of thrusting, with 45 km of shorten-

ing concentrated along the MAD. During **T6** (14-7 Ma), the uplift of the westernmost Eastern Cordillera is modeled with movement along the MAD ramp. By this time, the APD becomes completely deactivated, while sinistral strike-slip faulting affects the Puna and the Eastern Cordillera. During the last stage **T7** (7-0 Ma), 40 km of shortening is absorbed along the MAD, associated with the development of the Santa Barbara system as a bivergent thick-skinned fold-and-thrust belt.

5.2.3. The Southernmost Puna transect (27.6°S)

The core of the 27.6°S transect is modeled with movement along the Frontal Cordillera (FCD) and Eastern Main (EMD) decollements (Fig. 13). The incipient development of a shallow low-strength zone below the Pampean Ranges, inferred from the thermomechanical transect, is used to propose the existence of the active Pampean Range decollement (PRD) below this mountain belt. The EMD corresponds to a low-angle, west-dipping decollement placed in the upper ductile zone and rooted into the lower ductile low-strength zone.

Time **T0** (Fig. 16) is modeled with a thick crust in the present forearc and the westernmost sector of the Frontal Cordillera (35-40 km thick), produced by the Late Cretaceous contractional period. During stage **T1** (45-38 Ma), the FCD is active and is responsible for the uplift of the western Frontal Cordillera. This creates flexural subsidence in the Eocene foreland basin. At the end of this stage, a first uplift of the Pampean Ranges is modelled with reverse reactivation of deeply-seated faults.

During stage **T2** (38-23 Ma), the crust reaches 45 km below the Maricunga volcanic belt. The uplift of the Frontal Cordillera generates flexural subsidence in the Valle Ancho basin. During this stage, the Pampean Ranges register another pulse of uplift and exhumation. At the beginning of stage **T3** (23-15 Ma), shortening is focused on the eastern Frontal Cordillera, with movement along the FCD, where the crust achieves a thickness of >50 km, and in the Puna and Precordillera, with movement along the EMD. As a result, the Fiambalá basin starts to subside.

Deformation propagates to the east, reaching the Fiambalá basin during stage **T4** (15-10 Ma), and faults of the westernmost sector of the Pampean Ranges reactivate. The crust thickens up to 60 km below the Southern Puna. Deformation is focused in the Precordillera and the eastern sector of the Pampean Ranges during the next stage (**T5**, 10-5 Ma). During the next stage **T6** (10-0 Ma), both EMD and PRD decollements are active and contractional deformation is focused on the eastern Precordillera and both western and eastern Pampean Ranges.

5.2.4. The flat-slab transect (30°S)

The 30°S transect is modeled with two disconnected decollements: the Frontal Cordillera (FCD) and the Precordillera (pCD) decollements, following Mardonez et al. (2020) and Mardonez et al. (2020). The pCD is rooted into the ductile lower crust through an upper-crust ramp previously proposed by Ammirati et al. (2018) with receiver function analysis.

Time zero (**T0** > 45 Ma, Fig. 17) is modeled with a normal forearc and back-arc crust. The first stage of shortening (**T1**, 45-30 Ma) is modeled with 38 km of shortening and the generation of a back-to-back tectonic wedge with thrusts and back-thrusts uplifting both the Principal Cordillera and the western sector of the Frontal Cordillera. Subsidence is restricted to the Rodeo basin and Precordillera. During **T2** (30-20 Ma), extension, focused on the arc region, is modeled with two east-dipping normal faults in the Frontal Cordillera. During stage **T3** (20-15 Ma), the western Frontal Cordillera is uplifted through the east-directed Baños del Toro fault system rooted into the FCD. This uplift creates flexural subsidence in the Rodeo basin and Precordillera.

During **T4** (15-12 Ma), an eastward jump of the deformational front is modeled with thrusting in the western Precordillera with the generation of the pCD. This generates subsidence in the Bermejo basin. At the beginning of this phase, the FCD is still active, but it gets deactivated at the end of the phase. During **T5** (12-8 Ma), the central Precordillera and western Pampean Ranges are deformed and uplifted, while deformation ceases in the western Precordillera. This event is associated with a pronounced flexural subsidence in the Bermejo basin. The foreland is deformed by west- and east-dipping main faults, related to the uplift of the Pampean Ranges, but these faults are not interconnected to a decollement level.

During the next stage (**T6**, 8-5 Ma), horizontal shortening is absorbed by reverse faults in the central Precordillera, during ongoing uplift of the Pampean Ranges and flexural subsidence in the Bermejo basin. The last stage **T7** (5-0 Ma) is marked by deformation of the eastern Precordillera which is modeled with a shallow decollement connected eastward with an east-dipping ramp responsible for the uplift of the Pampean Ranges.

5.2.5. The Aconcagua transect (32.4°S)

This transect is modeled with two decollements located below the Principal Cordillera (PCD) and the Frontal Cordillera (FCD). Time zero (**T0** > 21 Ma, Fig. 18) is modeled from an initially thin crust below the Mesozoic marine basin (30 to 33 km), and a normal crust below the Pampean Ranges (35 to 38 km). Afterwards, we simulate the Late Cretaceous contractional event with 17 km of shortening focused along a west-dipping decollement, and the early Oligocene-early Miocene extension with 3 km of horizontal extension following previous studies in the western Principal Cordillera (Charrier et al., 2005, 2009; Mpodozis and Cornejo, 2012; Piquer et al., 2016; Mackaman-Lofland et al., 2020; Boyce et al., 2020; and references therein). The Miocene-Present contraction (**T1**, 21-18 Ma) is modeled with a ramp-flat-ramp decollement below the Coastal Range and the Principal Cordillera.

In the next phase (**T2**, 18-15 Ma), the PCD ramps upwards into the basal layers of the Mesozoic sequence and forms the Aconcagua fold-and-thrust belt is created. The foreland is shortening with the generation of east-transported faults in the Frontal Cordillera. During the **T3** period (15-12 Ma), deformation is mainly focused in the PCD and the faults uplifting the Frontal Cordillera. This period is modeled with movement along both PCD and FCD decollements.

Stage **T4** (12-9 Ma) is modeled with movement along the PCD and FCD. The FCD propagates eastward uplifting the western sector of the Precordillera. By the end of this stage, the Aconcagua fold-and-thrust belt becomes deactivated. During the **T5** stage (9-6 Ma), contractional deformation is concentrated along the FCD, promoting the uplift of the eastern Precordillera while the PCD experiences a reactivation. During the next stage **T6** (6-3 Ma), the deformational front migrates to the easternmost Precordillera.

During the last stage (**T7**, 3-0 Ma), horizontal shortening is accommodated along the easternmost sector of the FCD, the Cacheuta basin experiences uplift and denudation, and the Pampean Ranges uplift creating a broken foreland.

5.2.6. The Maipo/Tunuyán transect (33.6°S)

In a similar way to the 32.4°S transect, the 33.6°S transect (Fig. 13) is modeled with two decollements: the Principal Cordillera (PCD) and the Frontal Cordillera (FCD) decollements. The PCD has a ramp-flat geometry and is responsible for the uplift and exhumation of the western Principal Cordillera. Below the Aconcagua fold-and-thrust belt, it flattens and generates the Aconcagua orogenic wedge. The time zero (**T0**, Fig. 19) corresponds to the late Eocene to early Miocene extensional event that generates the Abanico intra-arc basin.

The Cenozoic compressional event starts between 21 and 18 Ma (**T1**), with the inversion of the Abanico basin. We model this stage with movement along both west- and east-directed faults, which uplift the western Principal Cordillera. During stage **T2** (18-15 Ma), the Aconcagua fold-and-thrust belt starts to develop, and the Frontal Cordillera has its first uplift. Both ranges produce flexural subsidence in the Alto Tunuyán and Cacheuta basins.

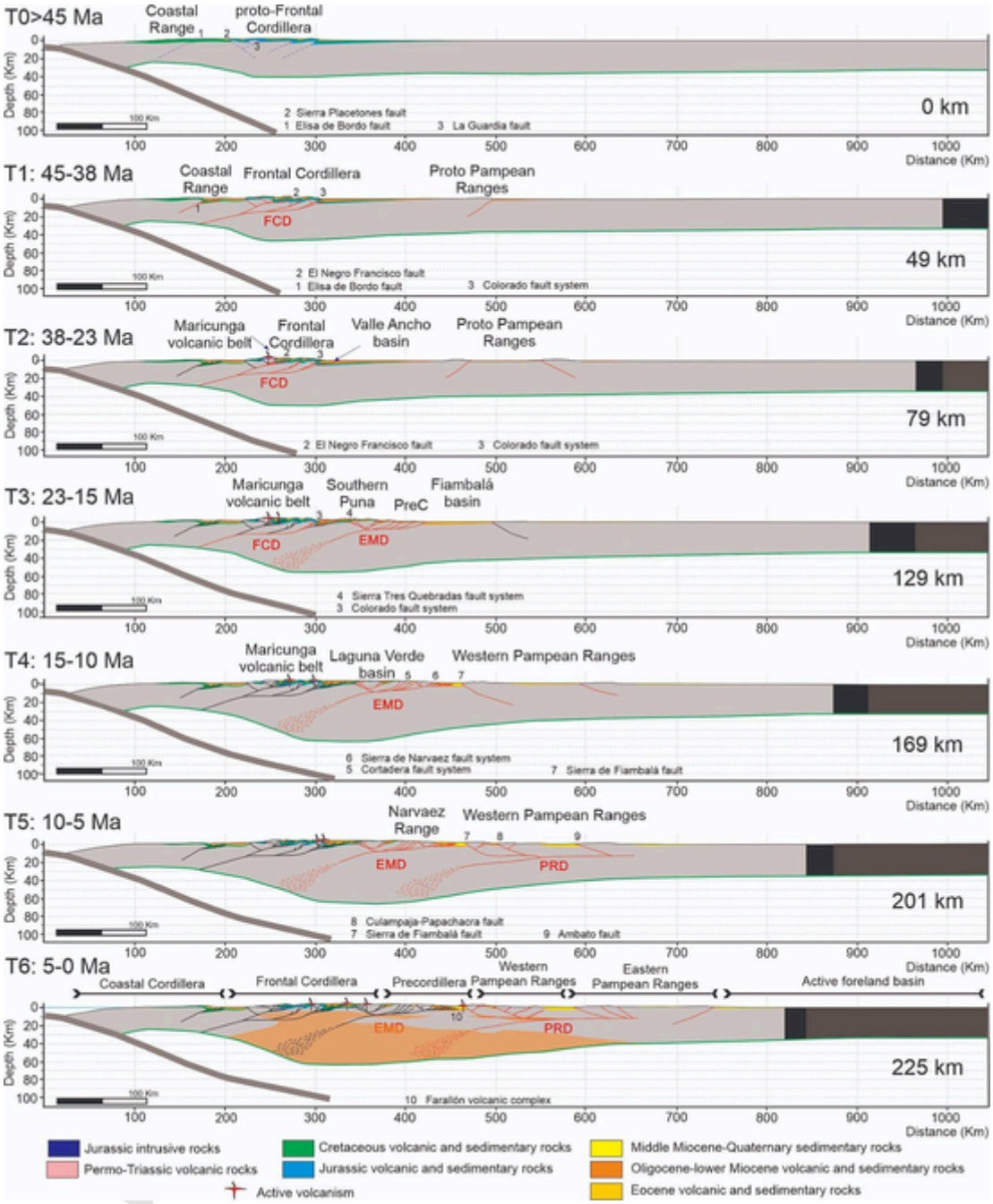

Fig. 16. Forward modeling of the Southernmost Puna transect (27.6°S). Time 0 has been set to pre-45 Ma. By this time, deformation was focused only on the Coastal Range and the Domeyko Range. During the next stages (T1 to T6), the crust is shortened by incorporating the equivalent of the crustal area (in black) into the crustal root, while the subduction zone is fixed. The length of the black area indicates the amount of crustal shortening achieved in each stage, calculated from the kinematic forward modeling +9.5% (9.5% is the difference between the crustal area balance and the kinematic forward modeling shortening estimates, see Table 1). FCD: Frontal Cordillera decollement, EMD: Eastern Main decollement, PRD: Pampean Ranges decollement, PreC: Precordillera. Red and black lines indicate active and inactive faults, respectively. Orange color in T7 indicates low-strength zones according to the thermomechanical model. (For interpretation of the references to colour in this figure legend, the reader is referred to the web version of this article.)

During **T3** (15-12 Ma), shortening is mainly absorbed in the Aconcagua FTB by movement along the PCD. During **T4** (12-9 Ma), both the PCD and the FCD are active through back-thrusting and out-of-sequence faults. During **T5** (9-6 Ma), there is an important uplift of the eastern Frontal Cordillera along the FCD. However, the PCD is still active, and is responsible for the back-thrust activity and exhumation of the western Principal Cordillera.

During **T6** (6-3 Ma), the PCD becomes inactive, and shortening is absorbed in the eastern Frontal Cordillera, with generation of frontal thrusts affecting the Cacheuta basin and the inversion of the Triassic Cuyo basin. During the last stage (**T7**, 3-0 Ma), shortening is accommodated in the FCD and the westernmost sector of the PCD with movements along the San Ramón fault.

5.2.7. The Tinguiririca/Malargüe transect (35°S)

The 35°S transect is modeled with one gently-west-dipping main decollement (MD), located between 10 and 15 km in depth. This decollement has a ramp-flat geometry, similar to the PCD we model in the 32.6° and 33.6°S transects. The ramp is located below the western-

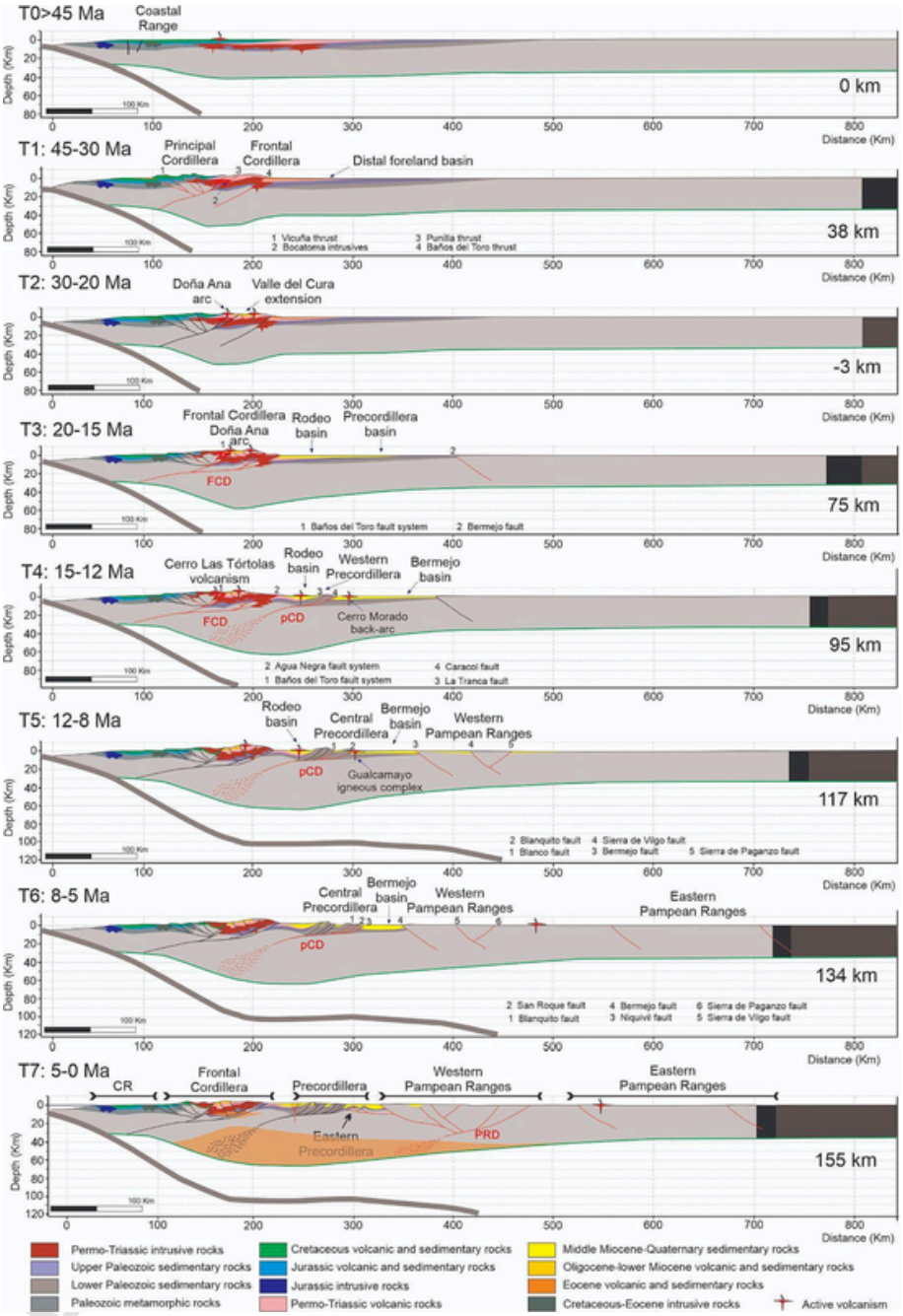

Fig. 17. Forward modeling of the flat-slab transect (30°S). Time 0 has been set to pre-45 Ma. By this time, deformation has been focused only on the Coastal Range. During the next stages (T1 to T7), the crust is shortened by incorporating the equivalent of the crustal area (in dark grey) into the crustal root, while the subduction zone is fixed. Active faults are in red. Inactive faults, developed in previous stages, are in black. The length of the black area indicates the amount of crustal shortening achieved in each stage, calculated from the kinematic forward modeling +12% (12% is the difference between the crustal area balance and the kinematic forward modeling shortening estimates, see Table 1). FCD: Frontal Cordillera decollement, pCD: Precordillera decollement. Orange color in T7 indicates low-strength zones according to the thermomechanical model. (For interpretation of the references to colour in this figure legend, the reader is referred to the web version of this article.)

most sector of the Principal Cordillera, while the flat segment is underlying the Malargüe fold-and-thrust belt. Time zero (**T0**, Fig. 20) corresponds to the Late Cretaceous deformation, modeled with a 35-to-40-km-thick crust, below the arc and back-arc region.

During **T1** (16-13 Ma), the MD is created, and the Mesozoic normal faults are reactivated. This contraction produces flexural subsidence in the Malargüe foreland basin. The following period (**T2**, 13-10 Ma) records further advance of the deformation towards the foreland modeled with an eastward prolongation of the main decollement. Out of sequence activity in the westernmost structures takes place likely during this stage.

Deformation propagates eastward during **T3** (10-6 Ma) and **T4** (6-3 Ma), but out-of- sequence deformation is modeled inside the fold-and-thrust belt. Finally, the last period **T5** (3-0 Ma) corresponds to 9 km of shortening transferred from the main decollement the faults along the orogenic front.

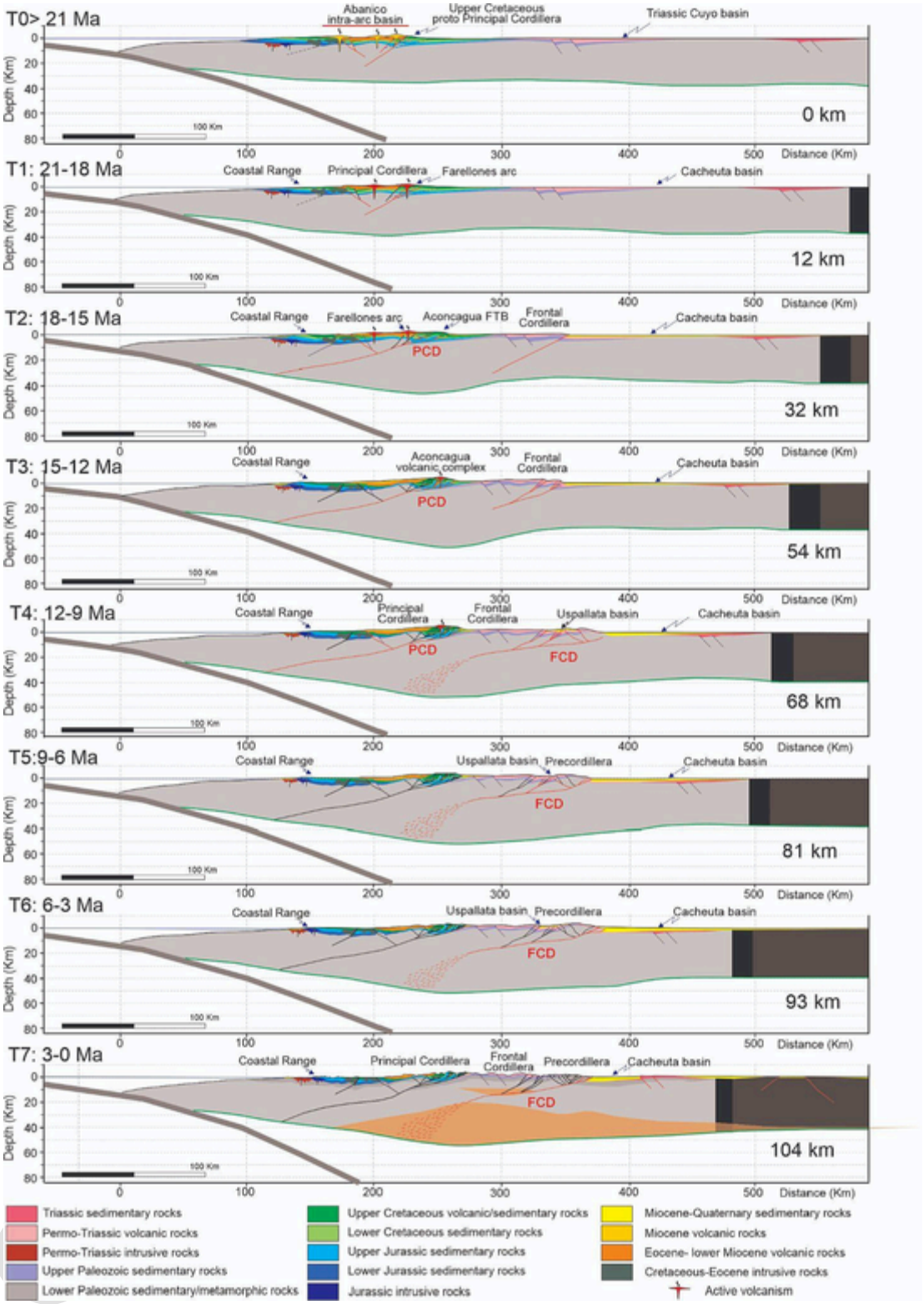

Fig. 18. Forward modeling of the Aconcagua transect (32.4°S). Time 0 has been set to pre-21 Ma. We model Time 0 with extension along the Triassic Cuyo basin, Upper Cretaceous contraction, focused in the western sector of the Principal Cordillera, and Oligocene – early Miocene extension, generating the Abanico intra-arc basin. During the next stages (T1 to T7), the crust is shortened by incorporating the equivalent of the crustal area (in black) into the crustal root, while the subduction zone is fixed. Active faults are in red, inactive faults are in dashed black lines. The length of the black area indicates the amount of crustal shortening achieved in each stage, calculated from the kinematic forward modeling +10% (10% is the difference between the crustal area balance and the kinematic forward modeling shortening estimates, see Table 1). PCD: Principal Cordillera decollement, FCD: Frontal Cordillera decollement. Orange color in T7 indicates low-strength zones according to the thermomechanical model. (For interpretation of the references to colour in this figure legend, the reader is referred to the web version of this article.)

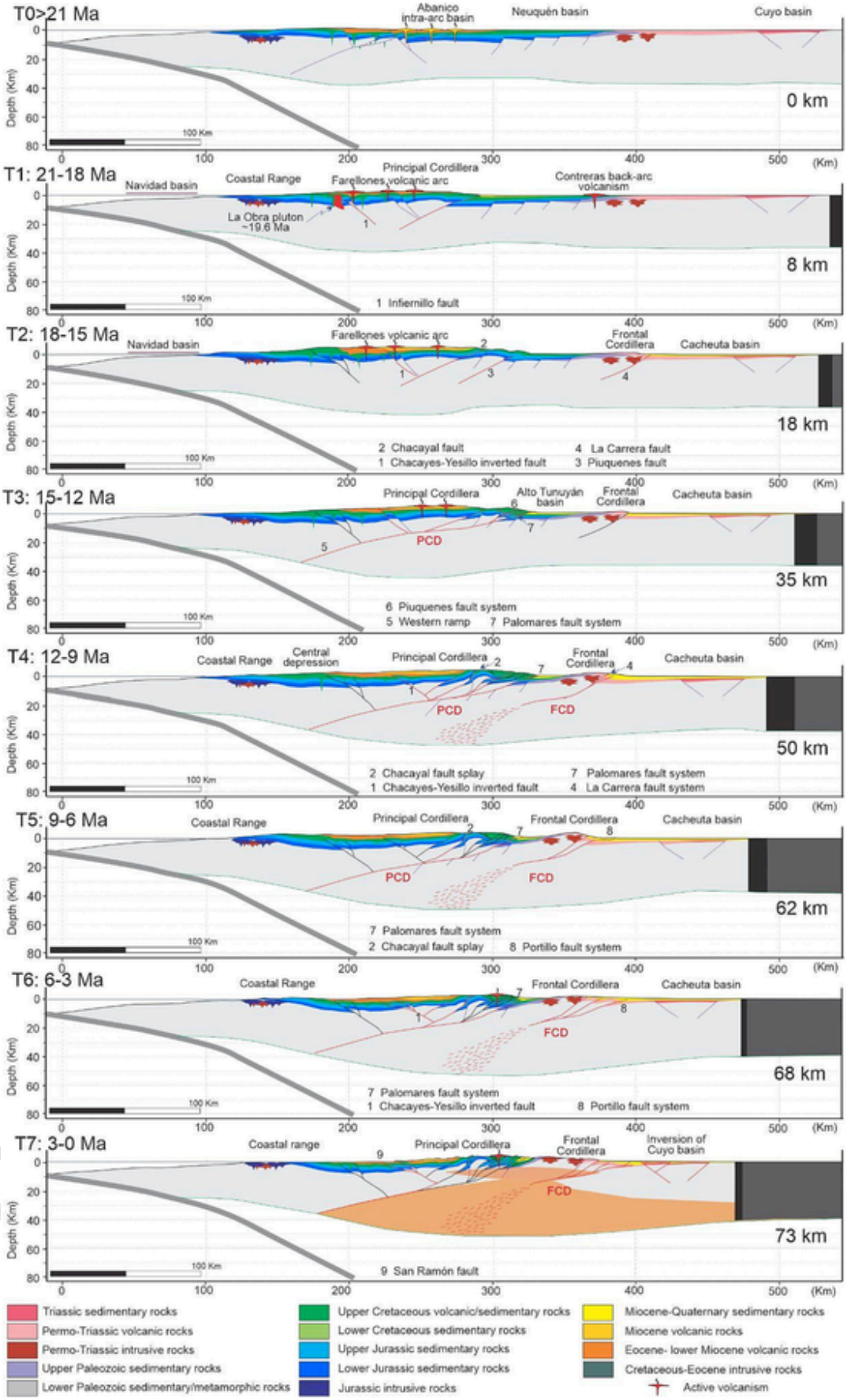
T0>21 Ma
Abanico intra-arc basin
Neuquén basin
Cuyo basin
0 km
T1: 21-18 Ma
Navidad basin
Coastal Range
Principal Cordillera
Farellones volcanic arc
Contreras back-arc volcanism
La Obra pluton ~19.6 Ma
8 km
1 Infiernillo fault
T2: 18-15 Ma
Navidad basin
Farellones volcanic arc
Frontal Cordillera
Cacheuta basin
18 km
2 Chacayal fault
1 Chacayes-Yesillo inverted fault
4 La Carrera fault
3 Piuquenes fault
T3: 15-12 Ma
Principal Cordillera
Alto Tunuyán basin
Frontal Cordillera
Cacheuta basin
PCD
35 km
6 Piuquenes fault system
5 Western ramp
7 Palomares fault system
T4: 12-9 Ma
Coastal Range
Central depression
Principal Cordillera
Frontal Cordillera
Cacheuta basin
PCD
FCD
50 km
2 Chacayal fault splay
1 Chacayes-Yesillo inverted fault
7 Palomares fault system
4 La Carrera fault system
T5: 9-6 Ma
Coastal Range
Principal Cordillera
Frontal Cordillera
Cacheuta basin
PCD
FCD
62 km
7 Palomares fault system
2 Chacayal fault splay
8 Portillo fault system
T6: 6-3 Ma
Coastal Range
Frontal Cordillera
Cacheuta basin
FCD
68 km
7 Palomares fault system
1 Chacayes-Yesillo inverted fault
8 Portillo fault system
T7: 3-0 Ma
Coastal range
Principal Cordillera
Frontal Cordillera
Inversion of Cuyo basin
FCD
73 km
9 San Ramón fault
Depth (Km)
100 Km
(Km)
Triassic sedimentary rocks
Permo-Triassic volcanic rocks
Permo-Triassic intrusive rocks
Upper Paleozoic sedimentary rocks
Lower Paleozoic sedimentary/metamorphic rocks
Upper Cretaceous volcanic/sedimentary rocks
Lower Cretaceous sedimentary rocks
Upper Jurassic sedimentary rocks
Lower Jurassic sedimentary rocks
Jurassic intrusive rocks
Miocene-Quaternary sedimentary rocks
Miocene volcanic rocks
Eocene- lower Miocene volcanic rocks
Cretaceous-Eocene intrusive rocks
Active volcanism

Fig. 19. Forward modeling of the Maipo transect (33.6°S), modified from Giambiagi et al. (2015a). Time 0 has been set to pre-21 Ma and modeled with extension along the Triassic Cuyo basin and the Jurassic Neuquén basin, Upper Cretaceous contraction, focused in the western sector of the Principal Cordillera, and Oligocene – early Miocene extension, generating the Abanico intra-arc basin. During the next stages (T1 to T7), the crust is shortened by incorporating the equivalent of the crustal area (in black) into the crustal root, while the subduction zone is fixed. Active faults are in red, inactive faults are in black lines. The length of the black area indicates the amount of crustal shortening achieved in each stage, calculated from the kinematic forward modeling +5% (5% is the difference between the crustal area balance and the kinematic forward modeling shortening estimates, see Table 1). PCD: Principal Cordillera decollement, FCD: Frontal Cordillera decollement. Orange color in T7 indicates low-strength zones according to the thermomechanical model. (For interpretation of the references to colour in this figure legend, the reader is referred to the web version of this article.)

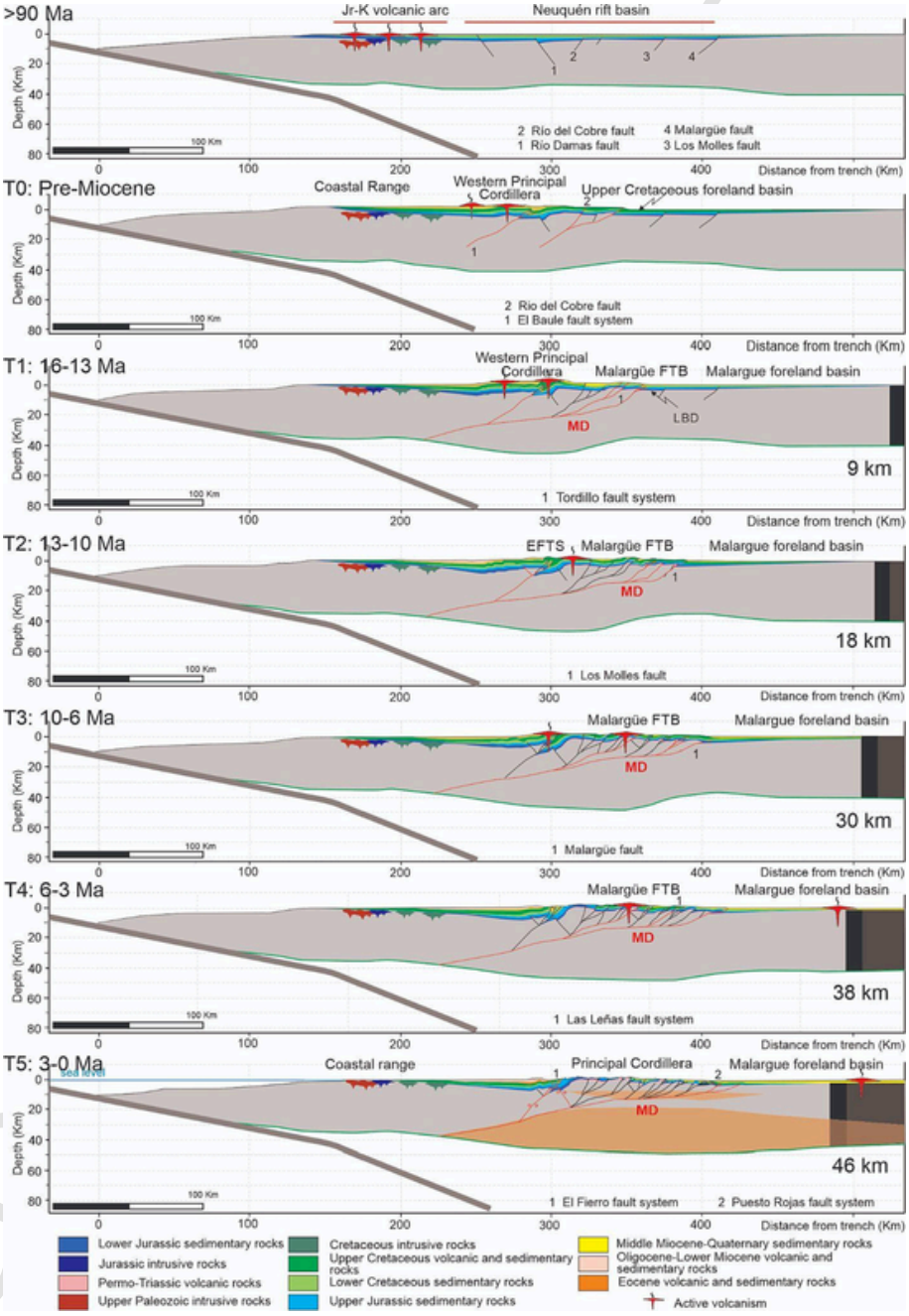

Fig. 20. Forward modeling of the Tinguiririca transect (35°S). Time 0 has been set to pre-16 Ma. We model Time 0 with extension along the Jurassic Neuquén basin, and Late Cretaceous contraction, focused in the western sector of the Principal Cordillera. During the next stages (T1 to T6), the crust is shortened by incorporating the equivalent of the crustal area (in black) into the crustal root, while the subduction zone is fixed. Active faults are in red, inactive faults are in dashed black lines. The length of the black area indicates the amount of crustal shortening achieved in each stage, calculated from the kinematic forward modeling +4% (4% is the difference between the crustal area balance and the kinematic forward modeling shortening estimates, see Table 1). MD: Main decollement. LBD: Los Blancos depocenter. Orange color in T7 indicates low-strength zones according to the thermomechanical model. (For interpretation of the references to colour in this figure legend, the reader is referred to the web version of this article.)

5.3. Geodynamic modeling of the upper-plate lithospheric shortening

The results of the deformation evolution obtained from the geodynamic model of the upper-plate lithospheric shortening are shown in Fig. 21. This evolution is set up in stages related to the amount of horizontal shortening. The first stage, after 5 km of shortening, shows a pure-shear shortening mode with deformation uniformly distributed in the hottest and weakest region of the model domain (Fig. 21A-B). The two crustal shear zones show different polarities and doubly vergence of westward and eastward dipping ~45°. The left one penetrates into the deep Moho, while the right one is rooted in the shallow ductile lower crust.

After 30 km of shortening, the crust thickens to ~40-45 km and forms an upper-crustal wedge along the decollement zone within the region of the left east-vergent shear zone in the first stage (Fig. 21C). Under the wedge, a zone of lower viscosity relative to the surrounding area is formed at the base of the upper crust, while the crustal root appears in the Moho (Fig. 21D). Furthermore, pre-existing faults located near the right east-vergent shear zone in the first stage tend to reactivate with the formation of another low-viscosity zone.

The crust thickens further with continued shortening and its root becomes wider and deeper, reaching thicknesses of 55 km and > 60 km after shortening by 80 km and 135 km, respectively (Fig. 21E-H). During the 80-km-shortening stage, a new crustal shear wedge is developed farther east of the first one due to the maturation of the second low-viscosity zone along a new eastward decollement (Fig. 21E-F).

At 135 km of shortening (Fig. 21G-H), a third low-viscosity zone is evolving as the decollement propagates eastward, resulting in deformation migrating toward the cold foreland without crustal root. Meanwhile, a high-topography hinterland with the thickest crust in the system has grown over the two crustal wedges formed in the first three wedge stages.

Our geodynamic model effectively reproduces the general evolution of crustal deformation as observed with the kinematic models described above for the Southern Central Andes. However, it is important to note that a major limitation in our model is the absence of any phase transformation processes, such as crustal eclogitization, which could be an essential driver for delamination and resultant lithospheric thinning (Krystopowicz and Currie, 2013). In addition, it is also necessary to consider the subduction dynamics in the west and the lateral variation between transects in future geodynamic models.

6. Discussion

6.1. Integrated model of crustal anatomy of the Southern Central Andes

The critical wedge theory (Dahlen et al., 1984; Dahlen and Barr, 1989) assumes that the overall shape of the fold-and-thrust belt can be reproduced by a wedge of rocks having a brittle behavior and frictionally sliding above a basal decollement. This analogy has been widely applied where a sedimentary cover is detached from the underlying basement along a shallow decollement, forming a thin-skinned thrust belt such as the Sub-Andean belt (22°S transect) or the Argentinean Precordillera (30°S transect). However, how far these decollements extend into the hinterland is a matter of debate (Martinod et al., 2020). At a greater depth, when the belt widens and the elevation of the hinterland increases, the wedge acquires a dimension where the premise of frictional behavior is difficult to achieve (Dahlen and Barr, 1989; Willett et

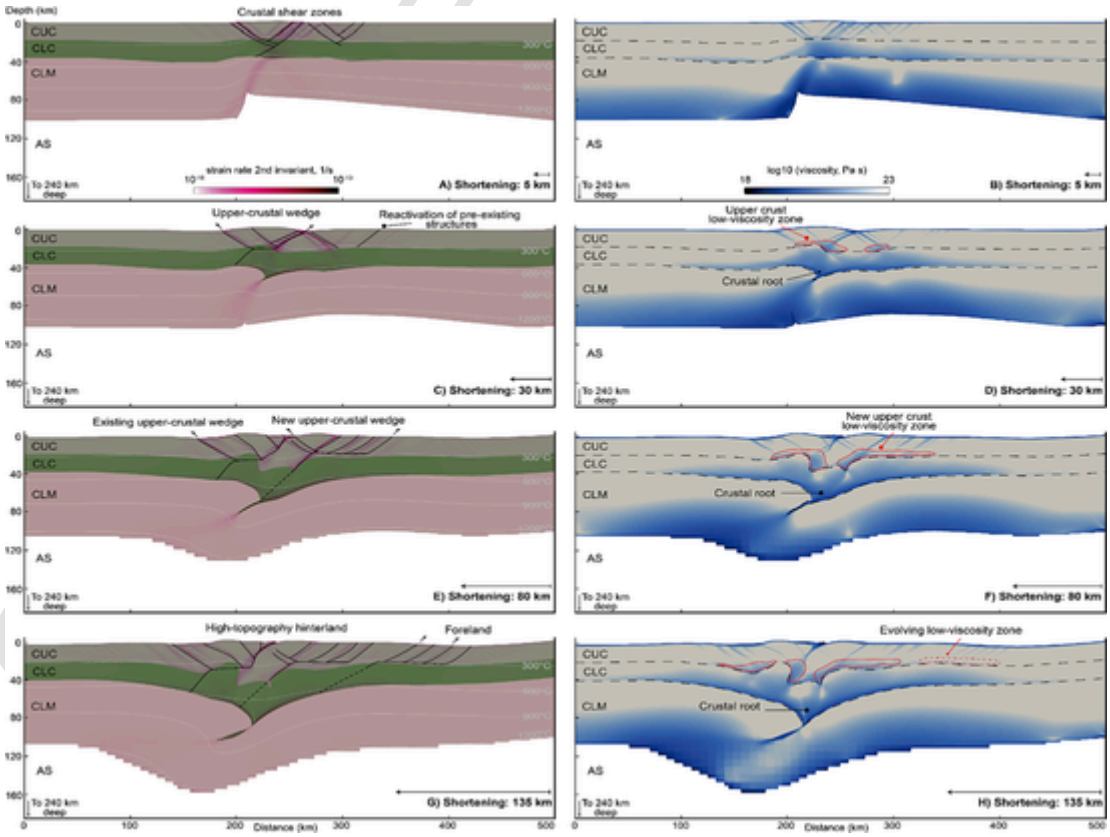

Fig. 21. Geodynamic model results showing the evolution of deformation and viscosity. A-B) After 5 km of shortening, the deformation is uniformly distributed in crustal shear zones dipping 45°. C-D) By 30 km of shortening, an upper crustal wedge is developed along the east-vergent decollement, accompanied by the formation of a low-viscosity zone at its bottom. E-F) After 80 km of shortening, a new crustal shear wedge accommodates deformation farther east. G-H) At 135 km of shortening, the deformation migrates eastward from the hot high-topography hinterland to the cold foreland. CUC: continental upper crust; CLC: continental lower crust; CLM: continental lithospheric mantle; AS: Asthenosphere.

al., 1993; Jamieson and Beaumont, 2013). Our thermomechanical and geodynamic models suggest that, at a certain depth, the decollement would be located in a low-strength, thermally activated, creeping shear zone (Willett et al., 1993), where the critical taper-wedge model may not apply. These shear zones are the product of vertical variations in crustal strength. The high-strength upper- and middle-crustal zones with competent elastic behavior are separated by a sub-horizontal region of low strength, located at the base of the upper crust (Figs. 13 and 21). According to our model, the role of this weak, low-strength zone is crucial to the development of a nearly flat decollement and has to be evaluated to propose a kinematic model for the construction of the orogenic system. Our results suggest that the active decollements (Fig. 22, red lines) are the ones located at the easternmost portion of the orogenic system at surface, while their westward extension at depth are rooted into the middle-lower ductile crust (Fig. 21), where the crust is thick enough to promote crustal flow.

Moreover, along- and across-strike variations in the Cenozoic geological history of the Southern Central Andes compiled in our forward kinematic models, as well as the results from the geodynamic model, indicate that these active decollements were the last ones to be generated. This pattern suggests that the eastward-transport kinematic models are the most suitable to explain the tectonic development of the orogenic system, as a whole. Moreover, it agrees with the substantial difference in the amount of crustal shortening absorbed on the western and eastern slopes of the orogenic system (Echaurren et al., 2022). It also agrees with the models proposed for the Altiplano by Elger et al. (2005) and Oncken et al. (2012), characterized by two disconnected decollements instead of a single, eastward-growing crustal wedge (McQuarrie, 2002, 2005). This interpretation is also shared by Martinod et al. (2020), who suggest that the widest sector of the Central Andes does not correspond to the eastward expansion of a single orogenic wedge, but rather to the presence of two distinct crustal wedges, a western one deforming the Western Cordillera and the Altiplano/Puna plateau, and an eastern one affecting the Eastern Cordillera and foreland ranges. Our geodynamic model reinforces this suggestion, favoring the generation of two independent crustal wedges, with the eastern wedge being the youngest.

According to our model, there is a marked along-strike, southward decrease in crustal shortening and crustal thickness from 22 to 35°S, reflected in a reduction of more than seven times in the magnitude of Cenozoic shortening (from ~325 to 46 km) and three times in the crustal root width (from ~526 to 170 km) (Fig. 22, Table 1). It is noteworthy that this trend is not coupled with the first-order segmentation of the Andes controlled by dip changes in the oceanic slab (e.g., Kay et al., 2009; and references therein), but agrees with the gradual and systematic decrease in the Eocene-Present crustal shortening values from the axis of the Andean orocline to the south (Isacks, 1988; Somoza et al., 1996; Kley, 1999; Prezzi and Alonso, 2002; Allmendinger et al., 2005; Arriagada et al., 2006; Giambiagi et al., 2012; Eichelberger et al., 2013; Horton, 2018).

When comparing our calculated shortening achieved during the middle-late Eocene (45-35 Ma), the Oligocene-early Miocene (35-20 Ma), the middle Miocene (20-10 Ma) and the late Miocene-Quaternary (10-0 Ma), a similar steady southward decay is identified (Fig. 22B). However, when comparing the shortening rates for the different time periods (Fig. 23), it is observed that the southward-decreasing shortening absorbed by the Southern Central Andes is not equally distributed during the Cenozoic. Instead, during the first Cenozoic contraction period (middle-late Eocene, 45-32 Ma), shortening was partitioned into rates of 7-10 mm/yr and ~ 2 mm/yr at the 22 and 27°S transects, respectively. Furthermore, the middle-late Eocene compressional phase only affects the segment north of 30°S (Oncken et al., 2012; Lossada et al., 2017; Faccenna et al., 2017). Interestingly, the shortening rates for the northern transects (22-32°S) converge to maximum values of ~6-8 mm/yr during the second Cenozoic contraction period (15-10 Ma) that, except for the northernmost transect at 22°S, decrease at similar rates during the Pliocene-Quaternary (Fig. 23).

This suggests that the present-day crustal anatomy of the Southern Central Andes is the result of a superposition of first-, second- and third-order controls. The first-order controls are responsible for the steady decrease, from the axis of the Andean orocline (20°S) to the south, of the amount of shortening and crustal thickening, as well as the width of the crustal root. It is also responsible for the different onset of deformation during the first Cenozoic event. One of these controls might be the subduction rate relative to the convergence rate that controls the advancing or retreating subduction type (Heuret and Lallemand, 2005; Doglioni et al., 2007). This ratio is related to variations in the slab thickness, controlled by the age of the Nazca plate at the trench (Yáñez and Cembrano, 2004; Capitanio et al., 2011). At the central part of the Andean orogen, where the slab is the oldest (50 Myr), the thick slab drives more traction towards the trench at the base of the continental plate (Capitanio et al., 2011), explaining the strong symmetry of the Central Andes. The ratio may also be controlled by sub-lithospheric dynamic processes such as subduction-induced mantle flow (Wdowinski and O'Connell, 1991; Schellart et al., 2007; Faccenna et al., 2017), and the resistance to slab retreat which is most significant in the center of the subduction zone (Husson et al., 2012; Schellart, 2017).

All these processes promote both the onset of Cenozoic contraction and the highest shortening rates at the axis of the Central Andes. Second-order controls, such as the convergence velocity and obliquity (Pardo-Casas and Molnar, 1987; Somoza, 1998; Quiero et al., 2022), are well correlated with the two periods of orogenic construction, the middle-late Eocene and the Miocene. Both contractional pulses occurred between periods of quasi-stationary convergence rates and changing tectonic conditions: while the first event took place during increasing convergence and orthogonality, the second one occurred simultaneously to convergence rates decreasing from a maximum value achieved after the break-up of the Farallon plate into the Nazca plate (Fig. 23C). Potential controlling factors over the diminishing of convergence rates during the second period include the anchoring of the Nazca plate at the 660 km-mantle discontinuity, taking place ~10-8 Myr after the breakup of the Farallon plate (Quinteros and Sobolev, 2013). Given the correlation of this latter event with the decrease of shortening rates, an additional control has been assigned to the increase of gravitational potential energy as the cordillera grows and shear stresses increase at the interplate megathrust (Norabuena et al., 1999; Iaffaldano et al., 2006; Quiero et al., 2022). During the second event of Andean orogenesis, different segments between 22 and 33°S show similar shortening rates, regardless of both their different previous orogenic development and their link with slab dynamics. While subduction and deep-mantle dynamics are first- and second-order controlling factors of the onset of Cenozoic contraction, our data suggest that third-order controls are related to variations both in crustal strength of the overriding-plate and in its mechanical weakening during the orogenic construction. In turn, the latter parameters are controlled to a great extent by the inherited compositional/lithological configuration of the continental crust, as previously proposed (Allmendinger et al., 1997; Tassara and Yáñez, 2003; Tassara, 2005; Mescua et al., 2014, et al., 2016). Another third-order control that might be considered is the out-of-the plane movement of crustal material which is not contemplated by our two-dimensional approach.

6.2. Relationship between crustal anatomy and seismicity

As has been proposed for many orogens around the World (Maggi et al., 2000), most non-subduction earthquakes in the Central Andes occur in the upper-middle crustal seismogenic layer, while the orogenic lower crust is completely aseismic. Tassara et al. (2007) and Ibarra et al. (2021) highlight the correlation between large lateral gradients in strength and location of active deformation and seismicity in the Alti-

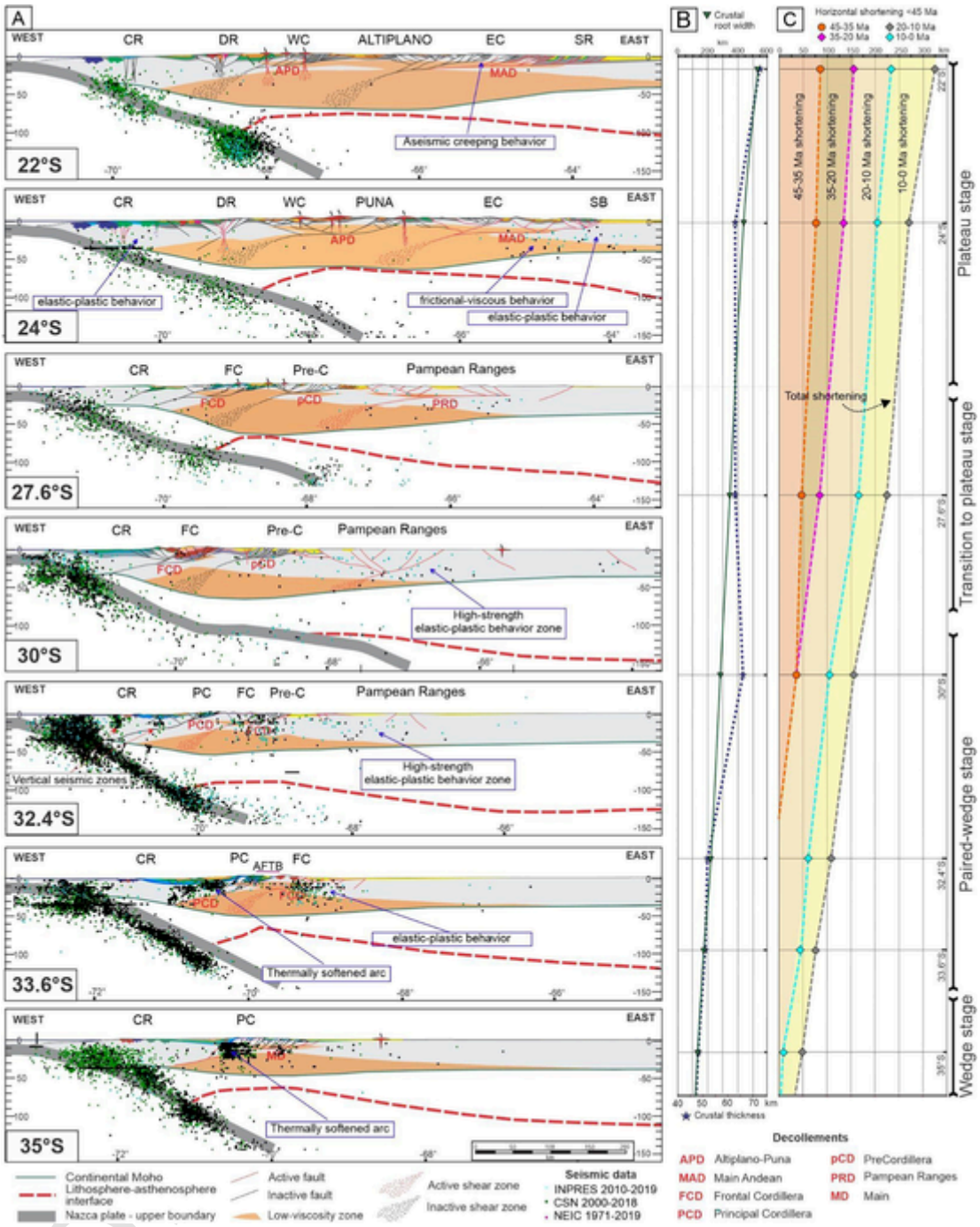

Fig. 22. A) Results for the seven kinematically-modelled transects (see locations in Fig. 1): Altiplano (22°S), Puna (24°S), Southernmost Puna (27.6°S), flat-slab (30°S), Aconcagua (32.4°S), Maipo (33.6°S) and Malargüe (35°S), with the subducted Nazca plate (grey lines), present-day Moho (green lines) and lithosphere/asthenosphere boundary (dashed red lines). Areas of predicted low strength and ductile behavior are highlighted in orange. Active decollements (in red) are located inside the uppermost part of the low-strength areas. Seismicity was selected considering a band of 0.25° width from north to south of the actual latitude and with a threshold of Mw > 2.5. CR: Coastal Range, DD: Domeyko Range, WC: Western Cordillera, EC: Eastern Cordillera, SR: Sub-Andean ranges, SB: Santa Bárbara system, PC: Principal Cordillera, FC: Frontal Cordillera, Pre-C: Precordillera. B) and C) Four parameters are compared for each of the cross-sections: (i) maximum crustal thickness, (ii) crustal root width (>45 km), (iii) total horizontal shortening (with errors), and (iv) shortening rates for the 45-35 Ma, 35-20 Ma, 20-10 Ma and 10-0 Ma periods (Supplementary Material, Table A2). The comparison of these parameters indicates a close relationship between crustal root width and total amount of shortening, and the numbers of decollements responsible for the crustal deformation. (For interpretation of the references to colour in this figure legend, the reader is referred to the web version of this article.)

plano/Puna latitudes. Of significant importance in convergent orogens is the middle-crust, high-strength zone (Royden, 1996; Vanderhaeghe et al., 2003), located below the upper low-strength zone. This zone is present below the Eastern Cordillera, the western sector of the Santa Bárbara system, the Frontal Cordillera, the Precordillera and the Malargüe FTB (Fig. 22). Our model suggests that the juxtaposition of two low- and high-strength layers promotes strain localization in the ductile, low-strength zone and the generation of a decollement. The upper and lower high-strength layers with predicted elastic/plastic behavior by our thermomechanical modeling, are subjected to high compres-

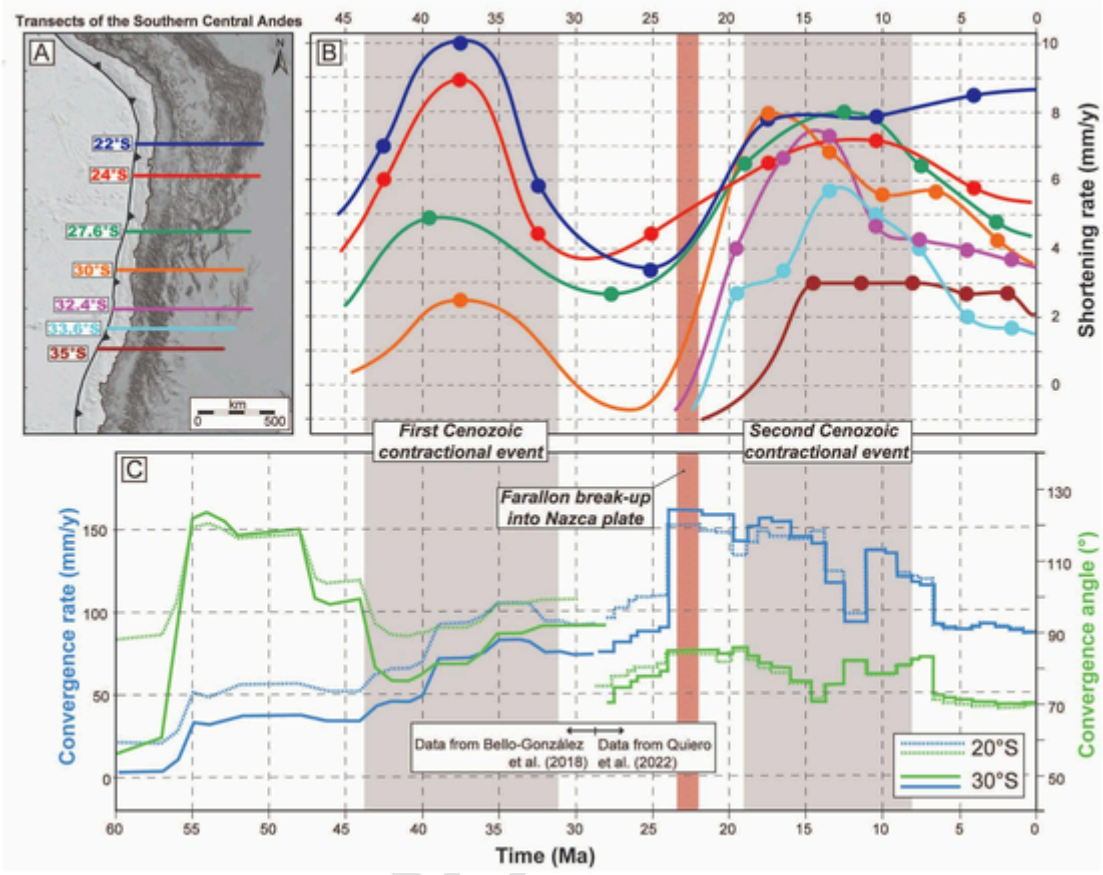

Fig. 23. A) Location of the seven cross-sections of the Southern Central Andes with color-coded symbology. B) Shortening rates vs time for the different transects. Two periods of maximum shortening rates can be clearly distinguished (gray rectangles), separated by a period of extension that affected the southern sector (30-35°S). During the first period (middle-late Eocene), there is a clear pattern of shortening rate decrease from north (22°S) to south (30°S). No Eocene deformation is registered further south. During the second period (Miocene), the shortening rate patterns are more complex indicating the superposition of different first-, second-, and third-order controls. C) Nazca-South America orthogonal convergence rates in the trench, based on relative plate motions from poles of rotations from Bello-González et al. (2018) for the 60-28 Ma period, and from Quiero et al. (2022) for the 28-0 Ma period.

sive stress and are seismically active (Fig. 22). In contrast, due to the aseismic creeping behavior of the decollements, seismicity is not concentrated along them. Few earthquakes are detected inside these low-strength zones, which are not likely related to frictional sliding, but to frictional-viscous behavior (Scholz, 1990). Seismicity inside these zones may reflect the fact that their elastic/elasto-plastic properties can sustain higher seismic strain rates than the ones necessary to activate dislocation or diffusion creep (Kirby et al., 1991).

In the western sector of the plateau transects (22-27°S), crustal seismic events are distributed within the entire crust through subvertical zones, mainly in the cold and rigid fore-arc and in the Domeyko Range (Fig. 22). Stress inversion from focal mechanisms in the fore-arc indicates a compressional region with N-S compression (González et al., 2015; Herrera et al., 2021). Neotectonic kinematic interpretation of these subvertical seismic zones in the Domeyko Range, along with focal mechanism inversion, suggest a strike-slip regime with active N to NE-striking, dextral strike-slip shear zones (Fig. 22), absorbing the parallel-to-the-trench vector of the oblique subduction (Victor et al., 2004; Cembrano and Lara, 2009; Salazar et al., 2017; Santibáñez et al., 2019; Herrera et al., 2021). In the eastern sector of the plateau transects, earthquakes are restricted to the crust that is being underthrusted under the Main Andean decollement. The area with high-strength is the most active in the foreland, reflecting a concentration of stress in the elastic/plastic field as a result of a thinner crust when compared with the crustal shield to the east.

In the 30°S transect, the flattening of the subducted slab extends for hundreds of kilometers and concentrates up to 3-5 times greater seismic energy release at the foreland as a result of the cooling of the upper lithosphere (Gutscher et al., 2000). The seismicity is located in the foreland, below the western and eastern borders of the Precordillera and the entire Pampean Ranges, at depths between 10 and 50 km (Fig. 22) (Smalley and Isacks, 1990; Pardo et al., 2002; Ramos et al., 2002; Rivas et al., 2019). Although different depths of decollements have been proposed for the Pampean Ranges (see Ramos et al., 2002; Richardson et al., 2012), the uniform distribution of crustal seismicity allow us interpreting the absence of an individual decollement in this sector.

In the 32.4° and 33.6°S transects, seismicity is concentrated in three areas in the upper-middle crust (Fig. 22): the fore-arc, the Principal Cordillera, and the foreland. In the fore-arc, seismicity is widely distributed, with a complicated mix of thrust and normal focal mechanisms (Comte et al., 2019). Below the central depression, seismicity depths delineate a west-dipping ramp rooted into the Moho, at the downdip limit of the elastic coupling along the subduction zone at ~55 km depth (Farías et al., 2010). This ramp shallows toward the east, below the Principal Cordillera, where seismicity is located at depths shallower than 20 km, and it is aligned with the N-S fault systems present in the western slope (Barrientos et al., 2004; Charrier et al., 2005; Farías et al., 2010; Nacif et al., 2017; Ammirati et al., 2019), as well as along a shallow decollement located at 10 km (Ammirati et al., 2022). The foreland is characterized as a 50 km-thick seismogenic crust suggesting that active faults extend across the crust rather than localized on upper-middle crust decollements (Meigs and Nabelek, 2010; Ammirati et al., 2018).

In the 35°S transect, the volcanic arc concentrates the majority of the crustal earthquake events (Villegas et al., 2016). Most of the re-

ported focal mechanisms in this area are strike-slip mechanisms (Alvarado et al., 2005; Comte et al., 2008; Spagnotto et al., 2015; Villegas et al., 2016), alienated along subvertical faults. In the foreland, the seismicity is distributed in the vicinity of the Malargüe thrust front, with an Mw ~ 6.0 event (5/30/1929; Lunkenheimer, 1930) and events of magnitude greater than 5.

6.3. The evolution of the decollements during the construction of the Andean orogenic system

By integrating results from the kinematic reconstructions, the present-day thermomechanical structure of the upper plate and the geodynamic numerical model, we propose the following four stages during the construction of the orogenic plateau system (Fig. 24): pre-wedge, wedge, paired-wedge and plateau stages. The pre-wedge stage resembles the small-cold orogen stage from Jamieson and Beaumont (2013) which consists of a single or back-to-back bivergent critical wedges with little or no ductile deformation. The plateau stage resembles their large-hot orogenic configuration with a central elevated plateau underlain by a weak ductile flow zone and flanked by external wedges. The wedge and paired-wedge stages represent the transition between these two-end member models.

6.3.1. Pre-wedge stage

A normal-to-slightly-thickened crust (< 40 km) with a very narrow crustal root and thick lithosphere inhibits the development of a thermally-activated shallow low-strength zone. As a result of this, no decollement is generated and deformation (< 30 km of shortening) is widely distributed throughout the crust, above the hottest part of the system (e.g., Fig. 21A-B). This stage resembles both a pure shear-dominated deformation stage with uniformly distributed plastic shear bands (Allmendinger and Gubbels, 1996; Jaquet et al., 2018) and the initial stage of a doubly vergent compressional orogen proposed by Willett et al. (1993), with the development of 45°-dipping shear zones under a symmetrical strain rate field. During this stage, pre-existing crustal anisotropies play a main role over the focus of deformation, guiding deformation through either reactivation of pre-existing contractional major faults, inversion of normal faults, or both. The model proposes that the first stage of Cenozoic uplift of the Domeyko Range, the proto-Frontal Cordillera stage and the inversion of the extensional Oligocene intra-arc basins all correspond to this pre-wedge stage.

6.3.2. Wedge stage

As the crust thickens (40-55 km) and the crustal root widens (100-200 km), a shallow low-strength zone develops in the upper-middle crust as thermal response to a simultaneous thinning of the lithosphere. This shallow low-strength zone is utilized as a sub-horizontal decollement and focuses most of the crustal deformation (30-80 km of shortening). This promotes the development of an upper-crustal wedge (e.g., Fig. 21C), tapering both towards the hinterland and the foreland. This stage resembles both the small-cold orogen that deforms by critical wedge mechanics (Jamieson and Beaumont, 2013) and the early deformation stage with topography steadily uplifted proposed by Wdowinski and Bock (1994). The decollement is formed from a prominent crustal-scale shear zone dipping towards the hottest part of the system with a top-to-foreland thrust direction (Jaquet et al., 2018) and is promoted by the asymmetric lithosphere-asthenosphere boundary (Barrionuevo et al., 2021). During this stage, pre-existing structures such as early Paleozoic shear zones, present in the foreland, may reactivate (e.g., Fig. 21D), uplifting basement blocks, such as the Pampean Ranges during the Miocene or the early uplift of the Eastern Cordillera during the Eocene. Crustal thickening requires proportional thickening of the mantle lithosphere as shown by our geodynamic model, but this must be compensated by some process capable of thinning the lid of lithosphere beneath the crustal root at a similar rate respect to the advancing crustal shortening/thickening (Pope and Willett, 1996). A continuous process has been proposed, such as ablative subduction (Tao and O'Connell, 1992; Pope and Willett, 1996) or the peeling off of the portion of dense lithospheric mantle by convective removal by the Rayleigh-Taylor gravitational instabilities developed in a thickened lithospheric mantle (Houseman et al., 1981; England and Houseman, 1989). These processes have been proposed for subduction-related orogens, such as the Colorado Plateau (Bird, 1979), the Canadian Cordillera (Bao et al., 2015), and the Altiplano-Puna Plateau (Kay and Kay, 1993; Lamb et al., 1997; Beck and Zandt, 2002; DeCelles et al., 2015b; Garzione et al., 2017).

6.3.3. Paired-wedge stage

During the widening of the crustal root (200-400 km), with a crustal thickness exceeding 55 km, the thermomechanical structure of the lithosphere fosters the development of a new decollement towards the foreland. The location and development of this new decollement is controlled by a new low-to-high strength contrast zone, and promoted by

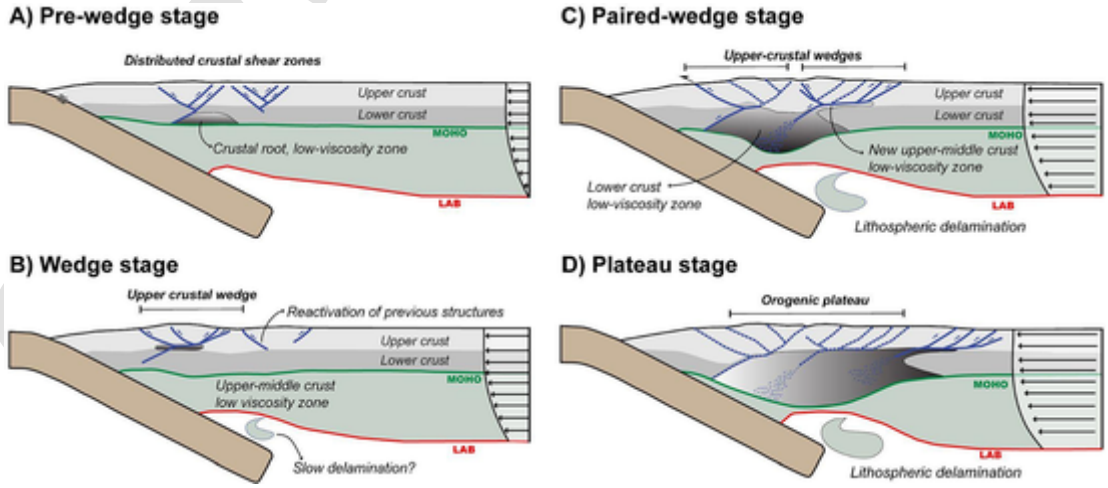

Fig. 24. Conceptual sketches representing the different proposed orogenic stages. A) Pre-wedge stage without a shallow low-strength zone, inhibiting the development of a decollement. B) Wedge stage with an upper-middle crust shallow low-strength zone, promoting the development of a decollement. C) Paired-wedge stage generated when the low-strength zone thickens and widens. The disappearance of a high contrast in strength produces the deactivation of the innermost decollement and promotes the development of a new one towards the foreland. D) Plateau stage, where the low-strength zone considerably widens, deactivating the internal orogenic decollements and fostering both the development of a new decollement along the new low-to-high strength contrast zone and the concentration of shortening towards the foreland.

thermal softening (Jaquet et al., 2018) and strain localization (Oncken et al., 2012). Even though two decollements may be simultaneously active during the early state of this stage, the western decollement eventually deactivates with progressive shortening (e.g., Fig. 21E-F). In our model, the maintenance of the crustal rheological layering, with a large strength contrast, is essential for sustaining the activity of the decollement. The thinning of the lithosphere increases the crustal temperature and produces a lack of strength contrast which promotes broadened shear zones at the western tip of the decollement, where it may become diffuse and rooted into a broader area of ductile behavior. At the eastern edge of these sub-horizontal low-strength zones, the decollement may ramp upwards and reach another rheological sub-horizontal layer contrast, such as the basement/sedimentary-cover interphase in the Precordillera (30°S). This stage represents the transition from a small-cold orogen, governed by critical wedge mechanics (wedge stage), to a large-hot orogen (plateau stage) proposed by Jamieson and Beaumont (2013). During this stage, the thinning of the continental lithosphere is promoted when the lower crust and mantle lithosphere are sufficiently soft (Morency and Doin, 2004). The broadening of the low-strength zone at the orogenic crustal root may play a critical role during this stage, promoting the decollement of the lithospheric mantle (Schott and Schmeling, 1998).

6.3.4. Plateau stage

The orogenic lithosphere weakens as the crust thickens and gets hotter, implying great temporal variations of the lithospheric strength (Jamieson and Beaumont, 2013; Chen and Gerya, 2016). Crustal thickening and lithospheric thinning leads to changes in the dominant deformational mechanism, from frictional Coulomb plasticity to thermally-activated viscous flow in the upper-middle crust (Willett et al., 1993; Jamieson and Beaumont, 2013; Jaquet et al., 2018). Moreover, the high strength contrast at mid-crustal levels may disappear, and the viscous flow of the lower crust promotes a low surface slope (Willett et al., 1993). The absence of lithospheric roots beneath the Altiplano/Puna plateau and the thinning of the lithosphere beneath the 27.6°S transect indicate that delamination or other lithospheric erosion processes should have occurred during the crustal shortening and thickening.

During this stage, a thick crust (>60 km) with a widened crustal root (>400 km) promotes the destruction of the elastic core by the expansion of the ductile low-strength zone, and, as a consequence, the demise of the internal decollement as the entire lower and middle crust becomes ductile. This stage is only achieved in the Altiplano (22°S) and Puna (24°S) transects. In these areas, active deformation is mainly concentrated along the eastern side of the Andes, where the upper crust is under-thrusted beneath the Sub Andean ranges and the Eastern Cordillera (Lyon-Caen et al., 1985; Isacks, 1988).

A fundamental feature of our model is that, although the low-strength ductile zones may extend throughout the entire width of the orogen, the decollement would vanish if there were no high contrast between a shallow high-strength zone and a deeper low-strength zone (Fig. 22).

6.3.5. Flat-slab particular case

A particular case occurs when the subduction angle substantially decreases, where the cooling effect of the subducting plate inhibits the development of the upper low-strength zone. This explains the deactivation of the decollement located below the Precordillera, at 30°S. Another particularity along the flat-slab transect is the abnormally deep brittle-ductile transition beneath the foreland (~40 km depth; Ammirati et al., 2013) associated with a highly active seismic zone at both crustal and mantle depths (Smalley et al., 1993; Alvarado et al., 2009).

7. Conclusions

In this study we investigated the crustal-scale structural evolution of the Southern Central Andes (22 -35°S), by integrating diverse previous and new geological and geophysical data with the results from new thermomechanical-numerical modeling. Our analysis of this Andean segment is focused in the last 45 Myr, when two distinct contractional episodes took place: during the middle-late Eocene and during the Miocene. These compressive pulses were unevenly distributed in space and time along the strike of the orogen, associated with different amounts of crustal shortening-thickening, uplift history, magmatism, and basin development.

Our approach consisted in the construction of seven cross sections perpendicularly to the strike of the orogen, whose deep and shallow crustal anatomy is constrained by a new thermomechanical model. Specifically, this model identifies sub-horizontal zones characterized by a high rheological contrast between crustal layers of low- and high-strength, where major decollements are most likely nucleated. This crustal arrangement was used as the final state of the structural forward modeling performed in these seven transects, from which we obtained new calculations of tectonic shortening and thickening. This coupled analysis indicates a clear reduction of the orogenic magnitude from the northern to southern ends of the Southern Central Andes (22 and 35°S), expressed as a sevenfold reduction of crustal shortening (from ~325 to 46 km) and a threefold reduction of crustal thickness (from ~526 to 170 km). This southward decrease of orogenic shortening and thickening is characterized by the presence of two independent decollements in the Altiplano-Puna plateau and only one decollement in the Principal Cordillera to the south. We complemented these results with a new geodynamic model that computes the spatio-temporal evolution of major crustal shear zones and the location of low-viscosity zones where sub-horizontal decollements are generated. This model shows an eastward migration of these parameters -toward the foreland- during increasing tectonic shortening, consistently with the deformational events described in the Southern Central Andes and the decollements constrained by the thermomechanical model.

In this contribution, we propose a novel evolutionary path for the orogenic growth of the Southern Central Andes. The initial state (pre-wedge stage) is characterized by a uniform distribution of deformation within a narrow region, at the axial zone and hottest region of the orogenic system. This stage is followed by the formation of one (wedge stage) or two (paired-wedge stage) crustal wedges associated to individual decollements that expand the mountain belt both laterally and vertically. The final state (plateau stage) corresponds to a highly broadened and thickened crustal system, where the western decollement has been deactivated and the eastern one controls a cratonward-directed tectonic transport.

Our results show a critical dependence between the localization of brittle deformation in the upper crust and the development of a mid-crustal, sub-horizontal decollement with a sharp contrast between low and high lithospheric strength. This structural arrangement can change during the formation of the crustal root and the asthenospheric thermal anti-root, with orogenic development and growth leading to the deactivation of the formerly active decollement and the generation of a new one toward the east.

Based in our integrated analysis, we identified the superposition of first-, second- and third-order controls over the evolution of the Southern Central Andes. The first-order controls correspond to subduction and sub-lithospheric dynamics correlated with the systematic decrease in the amounts of crustal shortening-thickening. Second-order controls are related to the convergence velocity and obliquity between the Nazca and South American plates. Third-order controls are associated with variations in the geologically inherited crustal strength of the overriding plate and its mechanical weakening effect during mountain building.

Data availability

The data presented in this manuscript can be found in the Supplementary Material 1 and 2, and Tables 1 and 2. The geodynamic model was run using the open-source ASPECT v2.3.0 with all model input files found here: doi.org/10.5281/zenodo.5783270. The kinematic models made with MOVE are available at doi:https://doi.org/10.5281/zenodo.6578074.

Uncited references

Eichelberger et al., 2013
Fuentes et al., 2016
Henriquez et al., 2020
Hoke et al., 2015
Rivas et al., 2020
Rodríguez Fernández et al., 1999
Rodríguez et al., 2012
Rojas Vera et al., 2019
Schoenbohm and Strecker, 2009
Smalley et al., 1993
Spagnotto et al., 2016
Vanderhaeghe et al., 2003

Declaration of Competing Interest

The authors declare that they have no known competing financial interests or personal relationships that could have appeared to influence the work reported in this paper.

Data availability

. Move files and input files for ASPECT are shared on Zenodo at: https://doi.org/10.5281/zenodo.6578074

Acknowledgments

This work was supported by the Argentine ANPCyT (PICT-2016-0269; PICT-2019-0800), the Argentina/Germany GFZ-CONICET consortium (StraTeGy), the Argentine CONICET (PIP 11220200101409CO) and the Chilean ANID project Nucleo Milenio CYCLO (NCN19_167). We thank the Computational Infrastructure for Geodynamics (geodynamics.org) for supporting the development of ASPECT. The geodynamic computation was supported by the North-German Supercomputing Alliance (HLRN). We acknowledge Midland Valley and Petex for the Academic Licence of the program MOVE to the Universidad Nacional de Cuyo. This manuscript has benefited from very helpful reviews by David Whipp, Jonas Kley, Brian Horton and Carlo Doglioni, as well as two anonymous reviewers, who are gratefully acknowledged.

Appendix A. Supplementary data

Supplementary data to this article can be found online at https://doi.org/10.1016/j.earscirev.2022.104138.

References

Acocella, V., Gioncada, A., Omarini, R., Riller, U., Mazzuoli, R., Vezzoli, L., 2011. Tectonomagmatic characteristics of the back-arc portion of the Calama-Olacapato-El Toro fault zone, Central Andes. Tectonics 30, TC3005. https://doi.org/10.1029/2010TC002854.

Allmendinger, R.W., Gubbels, T., 1996. Pure and simple shear plateau uplift, Altiplano-Puna, Argentina and Bolivia. Tectonophys. 259, 1–13.

Allmendinger, R.W., Judge, P., 2014. The Argentine Precordillera: a foreland thrust belt proximal to the subducted plate. Geosphere 10. https://doi.org/10.1130/GES01062.1.

Allmendinger, R.W., Zapata, T., 2000. The footwall ramp of the Subandean decollement, northernmost Argentina, from extended correlation of seismic reflection data. Tectonophys. 321, 37–55.

Allmendinger, R.W., Ramos, V.A., Jordan, T.E., Palma, M., Isacks, B.L., 1983. Paleogeography and Andean structural geometry, northwest Argentina. Tectonics 2, 1–16.

Allmendinger, R.W., Figueroa, D., Snyder, D., Beer, J., Mpodozis, C., Isacks, B.L., 1990. Foreland shortening and crustal balancing in the Andes at 30°S latitude. Tectonics 9, 789–809. https://doi.org/10.1029/TC009i004p00789.

Allmendinger, R.W., Jordan, T., Kay, S.M., Isacks, B., 1997. The evolution of the Altiplano-Puna plateau of the Central Andes. Annu. Rev. Earth Planet.Sci. 25, 139–174.

Allmendinger, R.W., Smalley, R., Bevis, M., Caprio, H., Brooks, B., 2005. Bending the Bolivian orocline in real time. Geology 33, 905–908. https://doi.org/10.1130/G21779.1.

Alonso, R., 1992. Estratigrafía del Cenozoico de la cuenca Pastos Grandes (Puna Salteña) con énfasis en la Formación Sijes y sus boratos. Rev. Asoc. Geol. Argentina 47, 189–199.

Alvarado, P., Beck, S., Zandt, G., Araujo, M., Triep, E., 2005. Crustal deformation in the south-central Andes backarc terranes as viewed from regional broad-band seismic waveform modelling. Geophys. J. Int. 163 (2), 580–598.

Alvarado, P., et al., 2009. Flat-slab subduction and crustal models for the seismically active Sierras Pampeanas region of Argentina. In: Kay, S.M., Ramos, V.A., Dickinson, W.R. (Eds.), Backbone of the Americas: Shallow Subduction, Plateau Uplift, and Ridge and Terrane Collision: Geological The Geological Society of America, Memoir 204. https://doi.org/10.1130/2009.1204(12).

Amilibia, A., Sàbat, F., McClay, K.R., Muñoz, J.A., Roca, E., Chong, G., 2008. The role of inherited tectono-sedimentary architecture in the development of the Central Andean mountain belt: Insights from the Cordillera de Domeyko. J. Struct. Geol. 30, 1520–1539.

Ammirati, J.-B., Alvarado, P., Perarnau, M., Saez, M., Monsalvo, G., 2013. Crustal structure of the Central Precordillera of San Juan, Argentina (31°S) using teleseismic receiver functions. J. S. Am. Earth Sci. 46, 100–109.

Ammirati, J.-B., Venerdini, A., Alcacer, J.M., Alvarado, P., Miranda, S., Gilbert, H., 2018. New insights on regional tectonics and basement composition beneath the eastern Sierras Pampeanas (Argentine back-arc region) from seismological and gravity data. Tectonophys. 740–741, 42–52. https://doi.org/10.1016/J.TECTO.2018.05.015.

Ammirati, J.-B., Easton, G., Rebolledo, S., Abrahami, R., Potin, B., Leyton, F., Ruiz, S., 2019. The crustal seismicity of the Western Andean thrust (Central Chile, 33°34°S): Implications for regional tectonics and seismic hazard in the Santiago area. Bull. Seis. Soc. America 109 (5), 1985–1999. https://doi.org/10.1785/0120190082.

Ammirati, J.-B., et al., 2022. Automated earthquake detection and local travel time tomography in the South-Central Andes (32-35°S): Implications for regional tectonics. J. Geoph. Res. Solid. Earth 127. . e2022JB'24097.

ANCORP-Working Group, 1999. Seismic reflection image revealing offset of Andean subduction-zone earthquake locations into oceanic mantle. Nature 397, 341–344.

ANCORP-Working Group, 2003. Seismic imaging of a convergent continental margin and plateau in the central Andes (Andean Continental Research Project 1996 (ANCORP'96)). J. Geophys. Res. 108 (B7). https://doi.org/10.1029/2002JB001771.

Anderson, M., Alvarado, P., Zandt, G., Beck, S., 2007. Geometry and brittle deformation of the subducting Nazca Plate, Central Chile and Argentina. Geophys. J. Int. 171, 419–434.

Anderson, R.B., Long, S.P., Horton, B.K., Thomson, S.N., Calle, A.Z., Stockli, D.F., 2018. Orogenic wedge evolution of the central Andes, Bolivia (21°S): Implications for Cordilleran cyclicity. Tectonics 37, 3577–3609. https://doi.org/10.1029/2018TC005132.

Andriessen, P.A.M., Reutter, K.-J., 1994. K-Ar and fission-track mineral age determination of igneous rocks related to multiple magmatic arc systems along the 23 latitude of Chile and NW Argentina. In: Reutter, K., Scheuber, E., Wigger, P. (Eds.), Tectonics of the Southern Central Andes. Springer, New York, pp. 141–153.

Arabasz, W.J.J., 1971. Geological and Geophysical studies of the Atacama fault zone in northern Chile. Geol. Planet. Sci. Department Ph.D. 264 pp.

Arancibia, G., 2004. Mid-cretaceous crustal shortening: evidence from a regional-scale ductile shear zone in the Coastal Range of central Chile (32°S). J.South Ame.Earth Sc. 17, 209–226.

Armijo, R., Rauld, R., Thiele, R., Vargas, G., Campos, J., Lacassin, R., Kausel, E., 2010. The West Andean Thrust, the San Ramon Fault, and the seismic hazard for Santiago, Chile. Tectonics 29. . TC2007.

Armijo, R., Lacassin, R., Coudurier-Curveur, A., Carrizo, D., 2015. Coupled tectonic evolution of Andean orogeny and global climate. Earth-Sci. Rev. 143, 1–35.

Arriagada, C., Cobbold, P.R., Roperch, P., 2006. Salar de Atacama basin: a record of compressional tectonics in the central Andes since the mid-Cretaceous. Tectonics 25, TC1008. https://doi.org/10.1029/2004TC001770.

Asch, G., Schurr, B., Bohm, M., Yuan, X., Haberland, C., Heit, B., Kind, R., Woelbern, I., Bataille, K., Comte, D., Pardo, M., Viramonte, J., Rietbrock, A., Giese, P., 2006. Seismological studies of the central and southern Andes. In: Oncken, O., Chong, G., Franz, G., Giese, P., Goetze, H.-J., Ramos, V.A., Strecker, M.R., Wigger, P. (Eds.), The Andes: Active Subduction Orogeny. Springer, Berlin, pp. 443–457. ISBN: 978-3-662-51783-3.

Astini, R., Thomas, W., 1999. Origin and evolution of the Precordillera terrane of western Argentina: A drifted Laurentian orphan. In: Ramos, V., Keppie, J. (Eds.), Laurentia-Gondwana Connections before Pangea. Geol. Soc. Ame. Spec. Paper, 336, pp. 1–20.

Avdievitch, N.N., Ehlers, T.A., Glotzbach, C., 2018. Slow long-term exhumation of the west central Andean plate boundary, Chile. Tectonics 37, 2018. https://doi.org/10.1029/2017TC004944.

Avouac, J.-P., 2008. Dynamic processes in extensional and compressional settings - mountain building: from earthquakes to geological deformation. In: Treatise on Geophysics. Vol.6. Elsevier, Amsterdam, ISBN 978-0-444-52748-6, pp. 377–439.

https://resolver.caltech.edu/CaltechAUTHORS:20110111-120419364.
Baby, P., Sempere, T., Oller, J., Barrios, L., Hérail, G., Marocco, R., 1990. Un bassin en compression d'age oligomiocene dans le Sud de l'Altiplano bolivien. CR Acad. Sci. Paris 311 (Ser. II), 341–347.
Baby, P., Herail, H., Salinas, R., Sempere, T., 1992. Geometry and kinematic evolution of passive roof duplexes deduced from crosssection balancing: example from the foreland thrust system of the southern Bolivian Subandean Zone. Tectonics 11, 523–536.
Baby, P., Moretti, I., Guillier, B., Limachi, R., Mendez, E., Oller, J., Specht, M., 1995. Petroleum system of the northern and central Bolivian sub-Andean zone. In: Tankard, A.J., Suarez, R., Welsink, H.J. (Eds.), Petroleum Basins of South America: Am. Assoc. Petrol. Geol. Memoir, 62, pp. 445–458.
Baby, P., Rochat, P., Herail, H., Mascle, G., 1997. Neogene shortening contribution to crustal thickening in the back arc of the Central Andes. Geology 25, 883–886.
Baker, M., Francis, P., 1978. Upper Cenozoic volcanism in the central Andes: ages and volumes. Earth Planet. Sci. Lett. 41, 175–187.
Baldauf, P., 1997. Timing of the uplift of the Cordillera Principal, Mendoza Province. Argentina. M. Sc. Thesis, George Washington University. 356 p.
Bally, A., Gordy, P., Stewart, G., 1966. Structure, seismic data, and orogenic evolution of southern Canadian Rocky Mountains. Bull. Can. Petrol. Geol. 14, 337–381.
Bande, A., Boll, A., Fuentes, F., Horton, B., Stockli, D., 2020. Thermochronological constraints on the exhumation of the Malargüe fold-thrust belt, southern Central Andes. In: Kietzmann, D., Folguera, A. (Eds.), Opening and Closure of the Neuquén Basin in the Southern Andes, Springer Earth System Sciences. https://doi.org/10.1007/978-3-030-29680-315.
Bangerth, W., Dannberg, J., Gassmoeller, R., Heister, T., 2019. ASPECT v2.1.0, *Zenodo*. https://doi.org/10.5281/zenodo.592692.
Bao, X.W., Eaton, D., Guest, A., 2015. Plateau uplift in western Canada caused by lithosphere delamination along a craton edge. Nat. Geosci. 7, 830–833. . channel flows: 1. Numerical models with applications to the tectonics of the Himalayan-Tibetan orogen. J. Geophys. Res: Solid Earth 109 (2004).
Barrientos, S., Vera, E., Alvarado, P., Monfret, T., 2004. Crustal seismicity in central Chile. J. S. Am. Earth Sci. 16, 759–768. https://doi.org/10.1016/j.jsames.2003.12.001.
Barrionuevo, M., Sibiao, L., Mescua, J., Yagupsky, D., Quinteros, J., Giambiagi, L., Sobolev, S., Strecker, M., Rodríguez Piceda, C., 2021. The influence of variations in crustal composition and lithospheric strength on the evolution of deformation processes in the southern Central Andes: insights from geodynamic models. J. Int. Earth Sci. https://doi.org/10.1007/s00531-021-01982-5.
Bascuñán, S., Arriagada, C., Le Roux, J., Deckart, K., 2016. Unraveling the Peruvian Phase of the Central Andes: stratigraphy, sedimentology and geochronology of the Salar de Atacama Basin (22°30–23°S), northern Chile. Basin Res. 28, 365–392.
Beck, S.L., Zandt, G., 2002. The nature of orogenic crust in the central Andes. J. Geophys. Res. Solid Earth 107. . ESE 7-1-ESE 7-16.
Beer, J.A., Allmendinger, R.W., Figueroa, D.E., Jordan, T.E., 1990. Seismic Stratigraphy of a Neogene Piggyback Basin, Argentina. Am. Assoc. Pet. Geol. Bull. 74, 1183–1202.
Bello-González, J.P., Contreras-Reyes, E., Arriagada, C., 2018. Predicted path for hotspot tracks off South America since Paleocene times: tectonic implications of ridge-trench collision along the Andean margin. Gondwana Res. https://doi.org/10.1016/j.gr.2018.07.008.
Bevis, M., Kendrick, E.C., Smalley, R., Herring, T., Godoy, J., Galban, F., 1999. Crustal motion north and south of the Arica deflection: comparing recent geodetic results from the central Andes. Geochem. Geophys. Geosyst. 1. https://doi.org/10.1029/1999GC000011.
Bialas, J., Kukowski, N., 2000. FS SONNE FAHRTBERICHT SO146/1&2/CRUISE REPORT SO146/1&2 GEOPECO: GEOphysical experiments at the PEruvian COntinental margin investigations of tectonics, mechanics, gashydrates, and fluid transport; Arica-Talcahuano, March 1-May 4, 2000.
Bird, P., 1979. Continental delamination and the Colorado Plateau. J. Geophys. Res. 84 (B13), 7561–7571. https://doi.org/10.1029/JB084iB13p07561.
Blanco, N., 2008. Estratigrafía y evolución tectono-sedimentaria de la cuenca cenozoica de Calama (Chile, 22°S). Master´s Thesis (unpublished). Universidad de Barcelona. . 68 p.
Blanco, N., Tomlinson, A.J., Mpodozis, C., Pérez d´Arce, C, Matthews, S., 2003. Formación Calama, Eoceno, II Región de Antofagasta: estratigrafía e implicancias tectónicas. In: Proceedings of the 10th Congreso Geológico Chileno, Concepción.
Boll, A., Alonso, A., Fuentes, F., Vergara, M., Laffitte, G., Villar, H.J., 2014. Factores controlantes |de las acumulaciones de hidrocarburos en el sector norte de la cuenca Neuquina, entre los ríos Diamante y Salado, Provincia de Mendoza, Argentina. In: proceedings of the 9th Congreso de Exploración y Desarrollo de Hidrocarburos, IAPG, Mendoza.
Bonali, F.L., Corazzato, C., Tibaldi, A., 2012. Elastic stress interaction between faulting and volcanism in the Olacapato-San Antonio de Los Cobres area (Puna plateau, Argentina). Glob. Planet. Chang. 90–91 (104), 120.
Bonini, R.A., Georgieff, S.M., Candela, A.M., 2017. Stratigraphy, geochronology, and paleoenvironments of Miocene-Pliocene boundary of San Fernando, Belén (Catamarca, northwest of Argentina). J. S. Am. Earth Sci. 79, 459–471. https://doi.org/10.1016/j.jsames.2017.08.020.
Bossi, G.E., Muruaga, C., 2009. Estratigrafía e inversión tectónica del rift neógeno en el Campo del Arenal, Catamarca, NO Argentina. Andean Geol. 36, 311–341.
Bossi, G.E., Georgieff, S., Gavriloff, I., Ibañez, L., Muruaga, C., 2001. Cenozoic evolution of the intramontane Santa María Basin, Pampean Ranges, northwestern Argentina. J. S. Am. Earth Sci. 14, 725–734.
Boyce, D., Charrier, R., Farías, M., 2020. The first Andean compressive tectonic phase: Sedimentologic and structural analysis of Mid-Cretaceous deposits in the Coastal Cordillera, Central Chile (32°50´S). Tectonics. https://doi.org/10.1029/2019TC005825.
Brooks, B., et al., 2011. Orogenic-wedge deformation and potential for great earthquakes in the central Andean backarc. Nat. Geosci. 4 (5), 1–4. https://doi.org/10.1038/ngeo1143.
Buelow, E., Suriano, J., Mahoney, J.B., Kimbrough, D.L., Mescua, J.F., Giambiagi, L.B., Hoke, G.D., 2018. Sedimentologic and stratigraphic evolution of the Cacheuta Basin: constraints on the development of the Miocene retroarc foreland basin, South-Central Andes. Lithosphere. https://doi.org/10.1130/L709.1.
Burchardt, S., Annen, C.J., Kavanagh, J.L., Hilmi Hazim, S., 2022. Developments in the study of volcanic and igneous plumbing systems: outstanding problems and new opportunities. Bull. Volcanol. 84 (6), 1–9.
Burov, E.B., 2011. Rheology and strength of the lithosphere. Mar. Pet. Geol. 28, 1402–1443.
Burov, E.B., Diament, M., 1995. The effective elastic thickness (Te) of continental lithosphere: what does it really mean? J. Geophys. Res. Solid Earth 100 (B3), 3905–3927.
Cahill, T., Isacks, B., 1992. Seismicity and shape of the Subducted Nazca Plate. J. Geophys. Res. Solid Earth 97, 17503–17529.
Canavan, R., Carrapa, B., Clementz, M.T., Quade, J., DeCelles, P.G., Schoenbohm, L.M., 2014. Early Cenozoic uplift of the Puna Plateau, Central Andes, based on stable isotope paleoaltimetry of hydrated volcanic glass. Geology 42 (5), 447–450. https://doi.org/10.1130/G35239.1.
Capaldi, T.N., Horton, B.K., McKenzie, N.R., Mackaman-Lofland, C., Stockli, D.F., Ortiz, G., Alvarado, P., 2020. Neogene retroarc foreland basin evolution, sediment provenance, and magmatism in response to flat slab subduction, western Argentina. Tectonics 39. https://doi.org/10.1029/2019TC005958.
Capitanio, F.A., Faccenna, C., Zlotnik, S., Stegman, D.R., 2011. Subduction dynamics and the origin of Andean orogeny and the Bolivian orocline. Nat. Lett. https://doi.org/10.1038/nature10596.
Carrapa, B., DeCelles, P.G., 2008. Eocene exhumation and basin development in the Puna of northwestern Argentina. Tectonics 27. https://doi.org/10.1029/2007TC002127. . TC1015.
Carrapa, B., Strecker, M.R., Sobel, E.R., 2006. Cenozoic orogenic growth in the Central Andes: evidence from sedimentary rock provenance and apatite fission track thermochronology in the Fiambalá Basin, southernmost Puna Plateau margin (NW Argentina). Earth Planet. Sci. Lett. 247, 82–100.
Carrapa, B., Hauer, J., Schoenbohm, L., Strecker, M.R., Schmitt, A.K., Villanueva, A., Sosa Gomez, J., 2008. Dynamics of deformation and sedimentation in the northern sierras Pampeanas: An integrated study of the Neogene Fiambalá basin, NW Argentina. Geol. Soc. Am. Bull. 120, 1518–1543. https://doi.org/10.1130/B26111.1.
Carrapa, B., Trimble, J.D., Stockli, D.F., 2011. Patterns and timing of exhumation and deformation in the Eastern Cordillera of NW Argentina revealed by (U-Th)/He thermochronology. Tectonics 30 (TC3003).
Carrapa, B., et al., 2022. Estimates of paleo-crustal thickness at Cerro Aconcagua (Southern Central Andes) from detrital proxy-records: implications for models of continental arc evolution. Earth Planet. Sci. Lett. 585, 11726.
Cashman, K.V., Sparks, R.S.J., Blundy, J.D., 2017. Vertically extensive and unstable magmatic systems: a unified view of igneous processes. Science 355 (6331). . eaag3055.
Cegarra, M., Ramos, V.A., 1996. La faja plegada y corrida del Aconcagua. In: Ramos, V.A. (Ed.), Geología de la región del Aconcagua, provincias de San Juan y Mendoza. SEGEMAR, Anales, 24, pp. 387–422.
Cembrano, J., Lara, L., 2009. The link between volcanism and tectonics in the southern volcanic zone of the Chilean Andes: a review. Tectonophys. 471, 96–113.
Cembrano, J., Zentilli, M., Grist, A., Yáñez, G., 2003. Nuevas Edades De Trazas De Fisión Para Chile Central (30°-34°S). Implicancias en el alzamiento y exhumación de Los Andes desde el Cretácico. In: proceedings of the 10th Congreso Geológico Chileno, Concepción.
Cembrano, J., Lavenu, A., Yañez, G., Riquelme, R., García, M., González, G., Hérail, G., 2007. Neotectonics. In: Moreno, T., Gibbons, W. (Eds.), The Geology of Chile, Geological Society of London. pp. 231–261. https://doi.org/10.1144/GOCH.
Charrier, R., Baeza, O., Elgueta, S., Flynn, J.J., Gans, P., Kay, S.M., Munoz, N., Wyss, A.R., Zurita, E., 2002. Evidence for Cenozoic extensional basin development and tectonic inversion south of the flat-slab segment, southern Central Andes, Chile (33°–36°S). J. S. Am. Earth Sci. 15, 117–139.
Charrier, R., Bustamante, M., Comte, D., Elgueta, S., Flynn, J.J., Iturra, N., Muñoz, N., Pardo, M., Thiele, R., Wyss, A.R., 2005. The Abanico Extensional Basin: Regional extension, chronology of tectonic inversion, and relation to shallow seismic activity and Andean uplift, Neues Jahrb. Geol. Palaeontol. Abh. 236, 43–47.
Charrier, R., Pinto, L., Rodríguez, M.P., 2007. Tectonostratigraphic evolution of the Andean Orogen in Chile. In: Moreno, T., Gibbons, W. (Eds.), The Geology of Chile, Geological Society of London. pp. 21–114.
Charrier, R., Farías, M., Maksaev, V., 2009. Evolución tectónica, paleogeográfica y metalogénica durante el cenozoico en los Andes de Chile Norte y Central e implicaciones para las regiones adyacentes de Bolivia y Argentina. Rev. Asoc. Geol. Argentina 65, 5–35.
Chen, L., Gerya, T.V., 2016. The role of lateral lithospheric strength heterogeneities in orogenic plateau growth: Insights from 3-D thermo-mechanical modeling. J. Geophys. Res. Solid Earth 121, 3118–3138. https://doi.org/10.1002/2016JB012872.
Chen, J., Kufner, S.-K., Yuan, X., Heit, B., Wu, H., Yang, D., Schurr, B., Kay, S., 2020. Lithospheric delamination benearth the Southern Puna plateau resolved by local earthquake tomography. J. Geophys. Res. Solid Earth 125. https://doi.org/10.1029/2019JB019040. . e2019JB019040.
Choukroune, P., ECORS Team, 1989. The ECORS Pyrenean deep seismic profile reflection data and the overall structure of an orogenic belt. Tectonics 8, 23–89.
Coblentz, D.D., Richardson, R.M., 1996. Analysis of the South American intraplate stress field. J. Geophys. Res. Solid Earth 101 (B4), 8643–8657.

Coira, B., Davidson, J., Mpodozis, C., Ramos, V.A., 1982. Tectonic and magmatic evolution of the Andes of northern Argentina and Chile. Earth Sci. Rev. 18, 303–322.
Collo, G., Ezpeleta, M., Dávila, F.M., Giménez, M., Soler, S., Martina, F., Schiuma, M., 2018. Basin thermal structure in the Chilean-Pampean Flat Subduction zone. In: The Evolution of the Chilean-Argentinean Andes. Springer, Cham, pp. 537–564.
Comínguez, A.H., Ramos, V.A., 1995. Geometry and seismic expression of the Cretaceous Salta rift system, northwestern Argentina. In: Tankard, A.J., Suárez, R., Welsink, H.J. (Eds.), Petroleum basins of South America. Am. Assoc. Petrol. Geol. Memoir, 62, pp. 325–340.
Comte, D., Farías, M., Charrier, R., González, A., 2008. Active tectonics in the Central Chilean Andes: 3D tomography based on the aftershock sequence of the 28 August 2004 shallow crustal earthquake. In: Proceedings of the 7° International Symposium on Andean Geodynamics (ISAG 2008, Nice). pp. 160–163.
Comte, D., Farías, M., Roecker, S., Russo, R., 2019. The nature of the subduction wedge in an erosive margin: Insights from the analysis of aftershocks of the 2015 Mw 8.3 illapel earthquake beneath the Chilean Coastal Range. Earth Planet. Sci. Lett. 520, 50–62.
Cornejo, P., Mpodozic, C., Ramírez, C., Tomlinson, C.F., 1993. Estudio geológico de la región de El Salvador y Potrerillos. SERNAGEOMIN, Informe Registrado IR-93-1: 1-258, Santiago, Chile.
Cortés, J., 2000. Hoja Palestina, Región de Antofagasta. SERNAGEOMIN, Mapas Geológicos 19, Santiago.
Cortés, J.M., Vinciguerra, P., Yamín, M., Pasini, M., 1999. Tectónica Cuaternaria de la Región Andina del Nuevo Cuyo (28°–38° LS). In: Caminos, R. (Ed.), Geología Argentina, SEGEMAR. Anales, Buenos Aires, vol 29, pp. 760–778.
Costa, C., Diederix, H., Gardini, C., Cortés, J., 2000. The Andean orogenic front at Sierra de Las Peñas-Las Higueras, Mendoza, Argentina. J. S. Am. Earth Sci. 13, 287–292.
Costa, C.H., Murillo, M.V., Sagripanti, G.L., Gardini, C.E., 2001. Quaternary intraplate deformation in the Southeastern Sierras Pampeanas, Argentina. J. Seismol. 5, 399–409.
Costa, C., Ahumada, E., Vázquez, F., Kröhling, D., 2015. Holocene shortening rates of an Andean-front thrust, Southern Precordillera, Argentina. Tectonophys. 664, 191–201.
Costa, C.H., Schoenbohm, L.M., Brooks, B.A., Gardini, C.E., Richard, A.D., 2019. Assessing Quaternary shortening rates at an Andean frontal thrust (32° 30′S), Argentina. Tectonics 38, 3034–3051.
Coughlin, T.J., O'Sullivan, P.B., Kohn, B.P., Holcombe, R.J., 1998. Apatite fission-track thermochronology of the Sierras Pampeanas, central western Argentina: implications for the mechanism of plateau uplift in the Andes. Geology 26, 999. https://doi.org/10.1130/0091-7613(1998)0262.3.CO;2.
Coutand, I., Cobbold, P., de Urreiztieta, M., Gautier, P., Chauvin, A., Gapais, D., Rossello, E., López Gamundi, O., 2001. Style and history of Andean deformation, Puna Plateau, northwestern Argentina. Tectonics 20, 210–234.
Coutand, I., Carrapa, B., Deeken, A., Schmitt, A.K., Sobel, E., Strecker, M.R., 2006. Orogenic plateau formation and lateral growth of compressional basins and ranges: insights from sandstone petrography and detrital apatite fission-track thermochronology in the Angastaco Basin, NW Argentina. Basin Res. 18, 1–26.
Cowan, A.M., Rech, J.A., Currie, B.S., 2004. Mid-Miocene hyperaridity in the Atacama Desert, Chile: evidence from the gypsic Barros Arana paleosol. Geol. Soc. Am. 36, 293–303.
Coward, M.P., 1983. Thrust tectonics, thin skinned or thick skinned, and the continuation of thrusts to deep in the crust. J. Struct. Geol. 5, 113–123.
Cristallini, E.O., Ramos, V.A., 2000. Thick-skinned and thin-skinned thrusting in the La Ramada fold and thrust belt: crustal evolution of the High Andes of San Juan, Argentina (32°S). Tectonophys. 317 (3–4), 205–235.
Cristallini, E.O., Comínguez, A.H., Ramos, V.A., Mercerat, E.D., 2004. Basement double-wedge thrusting in the northern Sierras Pampeanas of Argentina (27-28°S): Constraints from deep seismic reflection. In: McClay, K.R. (Ed.), Thrust Tectonics and Hydrocarbon Systems: AAPG Memoir, 82, pp. 65–90.
Dahlen, F.A., Barr, T.D., 1989. Brittle frictional mountain building, 1. Deformation and mechanical energy budget. J. Geophys. Res. 94, 3906–3922.
Dahlen, F.A., Suppe, J., Davis, D., 1984. Mechanics of fold-and-thrust belts and accretionary wedges: Cohesive Coulomb theory. J. Geophys. Res. 89. https://doi.org/10.1029/JB089iB12p10087. . 10,087–10,101.
Dávila, F.M., 2010. Dynamics of deformation and sedimentation in the northern Sierras Pampeanas: an integrated study of the Neogene Fiambalá Basin, NW Argentina: comment and discussion. Geol. Soc. Am. Bull. 122, 946–949. https://doi.org/10.1130/B30133.1.
Davila, F.M., Astini, R.A., 2007. Cenozoic provenance history of synorogenic conglomerates in western Argentina (Famatina belt): implications for Central Andean foreland development. Geol. Soc. Am. Bull. 119, 609–622.
Dávila, F., Giménez, M., Nóbile, J., Martínez, P., 2012. The evolution of the high-elevated depocenters of the northern Sierras Pampeanas (ca. 28° SL), Argentine broken foreland, South-Central Andes: the Pipanaco basin. Basin Res. 24, 1–22.
Davis, D., Suppe, J., Dahlen, F.A., 1983. Mechanics of fold-and-thrust belts and accretionary wedges. J. Geophys. Res. 1153–1172. https://doi.org/10.1029/JB088iB02p01153.
De Silva, S.L., 1989a. Geochronology and stratigraphy of the ignimbrites from the 21 to 23° S portion of the central Andes of northern Chile. J. Volcanol. Geotherm. Res. 37, 93–131.
De Silva, S.L., 1989b. Altiplano-Puna volcanic complex of the Central Andes. Geology 17 (12), 1102–1106. https://doi.org/10.1130/0091-7613.
De Silva, S., Zandt, G., Trumbull, R., Viramonte, J.G., Salas, G., Jiménez, N., 2006. Large ignimbrite eruptions and volcano-tectonic depressions in the Central Andes: a thermomechanical perspective. In: Troise, C., et al. (Ed.), Mechanisms of Activity and Unrest at Large Calderas: Geological Society of London, Special Publication, 269, pp. 47–63.
DeCelles, P.G., Horton, B.K., 2003. Early to middle Tertiary foreland basin development and the history of Andean crustal shortening in Bolivia. Geol. Soc. Am. Bull. 115, 58–77.
DeCelles, P.G., Carrapa, B., Horton, B.K., McNabb, J., Gehrels, E., Boyd, J., 2015a. The Miocene Arizaro basin, central Andes hinterland: response to partial lithosphere removal? Geol. Soc. Am. Mem. 212, 359–386.
DeCelles, P.G., Ducea, M.N., Kapp, P., Zandt, G., 2015b. Cyclicity in Cordilleran orogenic systems. Nat. Geosci. https://doi.org/10.1038/NGEO469.
Deckart, K., Godoy, E., Bertens, A., Jerez, D., Saeed, A., 2010. Barren Miocene granitoids in the central Andean metalogenic belt, Chile: geochemistry and Nd–Hf and U–Pb isotope systematic. Andean Geol. 37 (1), 1–31.
Deeken, A., Sobel, E.R., Coutand, I., Haschke, M., Riller, U., Strecker, M.R., 2006. Development of the southern Eastern Cordillera, NW Argentina, constrained by apatite fission track thermochronology: From early Cretaceous extension to middle Miocene shortening. Tectonics 25. https://doi.org/10.1029/2005TC001894. . TC6003.
del Papa, C., 1999. Sedimentation on a ramp type lake margin: Paleocene-Eocene Maíz Gordo Formation, Northwestern Argentina. J. S. Am. Earth Sci. 12, 389–400.
del Papa, C.E., Petrinovic, I.A., 2017. The development of Miocene extensional and short-lived basin in the Andean broken foreland: The Conglomerado Los Patos, Northwestern Argentina. J. S. Am. Earth Sci. 73, 191–201.
del Papa, C., Hongn, F., Powell, J., Payrola, P., Do Campo, M., Strecker, M., Petrinovic, I., Schmitt, A., Pereyra, R., 2013. Middle Eocene- Oligocene broken- foreland evolution in the Andean Calchaqui Valley, NW Argentina: insights from stratigraphic, structural and provenance studies. Basin Res. 25 (5), 574–593.
del Rey, Á., Deckart, K., Planavsky, N., Arriagada, C., Martínez, F., 2019. Tectonic evolution of the southwestern margin of Pangea and its global implications: evidence from the mid Permian–Triassic magmatism along the Chilean-Argentine border. Gondwana Res. 76, 303–321.
Deri, M., Ciccioli, P., Amidon, W., Marenssi, S., 2019. Estratigrafía y edad máxima de depositación de la Formación Tambería en el Bolsón de Fiambalá, Catamarca. In: Proceedings of the 5th Simposio del Mioceno Pleistoceno del Centro y Norte de Argentina. p. 3.
Dewey, J.F., Bird, J.M., 1970. Mountain belts and the new global tectonics. J. Geophys. Res. 75, 2625–2647. https://doi.org/10.1029/JB075i014p02625.
Díaz-Alvarado, J., Galaz, G., Oliveros, V., Creixell, C., Calderón, M., 2019. Fragments of the late Paleozoic accretionary complex in central and northern Chile: similarities and differences as a key to decipher the complexity of the late Paleozoic to Triassic early Andean events. In: Horton, B., Folguera, A. (Eds.), Andean Tectonics. Elsevier, pp. 509–530.
D'nnunzio, C., Rubinstein, N., Rabbia, O., 2018. Petrogenesis of the Gualcamayo Igneous Complex: Regional implications of Miocene magmatism in the Precordillera over the Pampean flat slab segment, Argentina. J. S. Am. Earth Sci. https://doi.org/10.1016/j.jsames.2018.06.012.
Dunn, J.F., Hartshorn, K.G., Hartshorn, P.W., 1995. Structural styles and hydrocarbon potential of the Sub-Andean thrust belt of southern Bolivia. In: Tankard, A., Suarez Soruco, R., Welsink, H. (Eds.), Petroleum Basins of South America. Am. Assoc. Petroleum Geol. Mem., 62, pp. 523–543.
Echaurren, A., et al., 2022. Fore-to-retroarc crustal structure of the north Patagonian margin: How is shortening distributed in Andean-type orogens? Glob. Planet. Chang. 209, 103734.
Echavarria, R., Hernandez, R., Allmendinger, R.W., Reynolds, J.H., 2003. Sub-Andean thrust and fold belt of northwest Argentina: geometry and timing of the Andean evolution. Am. Assoc. Pet. Geol. Bull. 87, 965–985. https://doi.org/10.1306/01200300196.
Ege, H., Sobel, E.R., Scheuber, E., Jacobshagen, V., 2007. Exhumation history of the southern Altiplano plateau (southern Bolivia) constrained by apatite fission track thermochronology. Tectonics 26, TC1004. https://doi.org/10.1029/2005TC001869.
Eichelberger, N., McQuarrie, N., Ehlers, T.A., Enkelmann, E., Barnes, J.B., Lease, R.O., 2013. New constraints on the chronology, magnitude, and distribution of deformation within the central Andean orocline. Tectonics 32, 1432–1453. https://doi.org/10.1002/tect.20073.
Elger, K., Oncken, O., Glodny, J., 2005. Plateau-style accumulation of deformation: Southern Altiplano. Tectonics 24. https://doi.org/10.1029/2004TC001675. . TC4020.
Emparan, C., Pineda, G., 1999. Área Condoriaco-Rivadavia, Región de Coquimbo: Mapas Geológicos, No12. SERNAGEOMIN. Mapa escala 1:100.000.
Emparan, C., Pineda, G., 2000. Área La Serena-La Higuera, región de Coquimbo. SERNAGEOMIN. Mapas Geológicos, No18. 1 Mapa escala 1:100.000.
Emparan, C., Pineda, G., 2006. Geología del Área Andacollo-Puerto Aldea, Región de Coquimbo. SERNAGEOMIN, Cart. Geol. Chile. Geol. Básica 86, 85.
England, P., Houseman, G., 1989. Extension during continental convergence, with application to the Tibetan Plateau. J. Geophys. Res. 94. https://doi.org/10.1029/JB094iB12p17561.
Faccenna, C., Oncken, O., Holt, A.F., Becker, T.W., 2017. Initiation of the Andean orogeny by lower mantle subduction. Earth Planet. Sci. Lett. 463, 189–201.
Farías, M., Charrier, R., Comte, D., Martinod, J., Hérail, G., 2005. Late Cenozoic deformation and uplift of the western flank of the Altiplano: Evidence from the depositional, tectonic, and geomorphologic evolution and shallow seismic activity (northern Chile at 19°30′S). Tectonics 24, TC4001. https://doi.org/10.1029/2004TC001667.
Farías, M., Charrier, R., Carretier, S., Martinod, J., Fock, A., Campbell, D., Cáceres, J., Comte, D., 2008. Late Miocene high and rapid surface uplift and its erosional response in the Andes of central Chile (33°–35°S). Tectonics 27, TC1005. https://doi.org/10.1029/2006TC002046.
Farías, M., Comte, D., Charrier, R., Martinod, J., David, C., Tassara, A., Tapia, F., Fock, A., 2010. Crustal-scale structural architecture in central Chile based on seismicity and

surface geology: Implications for Andean mountain building. Tectonics 29, TC3006. https://doi.org/10.1029/2009TC002480.
Fazzito, S., Cortés, J.M., Rapalini, A.E., Terrizzano, C.M., 2013. The geometry of the active strike-slip El Tigre Fault, Precordillera of San Juan, Central-Western Argentina: integrating resistivity surveys with structural and geomorphological data. Int. J. Earth Sci. 102, 1447–1466.
Feng, M., Assumpçao, M., Van der Lee, S., 2004. Group-velocity tomography and lithospheric S-velocity structure of the South American continent. Phys. Earth Planet. Inter. 147 (4), 315–331.
Feng, M., Van der Lee, S., Assumpção, M., 2007. Upper mantle structure of South America from joint inversion of waveforms and fundamental mode group velocities of Rayleigh waves. J. Geophys. Res. Solid Earth 112 (B4).
Flesch, L.M., Kreemer, C., 2010. Gravitational potential energy and regional stress and strain rate fields for continental plateaus: Examples from the central Andes and Colorado Plateau. Tectonophysics 482 (1–4), 182–192.
Flint, S., Turnere, P., Jolley, E., Hartley, A., 1993. Extensional tectonics in convergent margin basins: An example from the Salar de Atacama. Chilean Andes. Geol. Soc. Ame. Bull. 105, 603–617.
Flueh, E.R., Grevemeyer, I., 2005. RV Sonne Fahrtbericht/Cruise Report SO181 TIPTEQ (from The Incoming Plate to mega Thrust EarthQuakes) 06.12. 2004.-26.02. 2005.
Fock, A., Charrier, R., Marsaev, V., Farías, M., Alvarez, P., 2006. Evolución cenozoica de los andes de chile central (33°-34°s). In: Proceedings of the 9th Congreso Geológico Chileno, Antofagasta, Chile, 2, pp. 205–208.
Fosdick, J.C., Carrapa, B., Ortiz, G., 2015. Faulting and erosion in the Argentine Precordillera during changes in subduction regime: reconciling bedrock cooling and detrital records. Earth Planet. Sci. Lett. 432, 73–83.
Fosdick, J.C., Reat, E.J., Carrapa, B., Ortiz, G., Alvarado, P.M., 2017. Retroarc basin reorganization and aridification during Paleogene uplift of the southern central Andes. Tectonics 36, 493–514. https://doi.org/10.1002/2016TC004400.
Fox-Maule, C., Purucker, M.E., Olsen, N., Mosegaard, K., 2005. Heat flux anomalies in Antarctica revealed by satellite magnetic data. Science 309 (5733), 464–467.
Froidevaux, C., Isacks, B., 1984. The mechanical state of the lithosphere in the Altiplano-Puna segment of the Andes. Earth Planet. Sci. Lett. 71, 305–314.
Fromm, R., Zandt, G., Beck, S., 2004. Crustal thickness beneath the Andes and Sierras Pampeanas at 30°S inferred from Pn apparent phase velocities. Geophys. Res. Lett. 31, L06625. https://doi.org/10.1029/2003GL019231.
Fuentes, F., Horton, B.K., Starck, D., Boll, A., 2016. Structure and tectonic evolution of hybrid thick- and thin-skinned systems in the Malargüe fold-thrust belt, Neuquén basin. Argentina. Geol. Magaz. 153, 1066–1084.
Furque, G., et al., 2003. Hoja Geológica 3169-II, San José de Jáchal. Provincias de San Juan y La Rioja., 259. SEGEMAR. Buenos Aires.
Gans, Ch., Beck, S.L., Zandt, G., Gilbert, H., Alvarado, P., Anderson, M., Linkimer, L., 2011. Continental and oceanic crustal structure of the Pampean flat slab region, western Argentina, using receiver function analysis: new high-resolution results. Geophys. J. Int. 186, 45–58.
García, V., Casa, A., 2015. Quaternary tectonics and seismic potential of the Andean retrowedge at 33-34°S. In: Sepulveda, S., et al. (Ed.), Geodynamic Processes in the Andes of Central Chile and Argentina. Geol. Soc. London, Special Publications, 399. https://doi.org/10.1144/SP399.11.
Garzione, C., et al., 2017. Tectonic evolution of the Central Andean Plateau and implications for the growth of plateaus. Annu. Rev. Earth Planet. Sci. 2017 (45), 529–559.
Giambiagi, L., Ramos, V.A., 2002. Structural evolution of the Andes between 33°30′ and 33°45′S, above the transition zone between the flat and normal subduction segment, Argentina and Chile. J. S. Am. Earth Sci. 15, 99–114.
Giambiagi, L.B., Ramos, V.A., Godoy, E., Alvarez, P.P., Orts, S., 2003. Cenozoic deformation and tectonic style of the Andes, between 33° and 34° south latitude. Tectonics 22. https://doi.org/10.1029/2001tc001354.
Giambiagi, L., Bechis, F., García, V., Clark, A., 2008. Temporal and spatial relationship between thick- and thin-skinned deformation in the Malargüe fold and thrust belt, southern Central Andes. Tectonophys. 459, 123–139.
Giambiagi, L., Mescua, J., Bechis, F., Martínez, A., Folguera, A., 2011. Pre-Andean deformation of the Precordillera southern sector, Southern Central Andes. Geosphere 7, 1–21.
Giambiagi, L., Mescua, J., Bechis, F., Tassara, A., Hoke, G., 2012. Thrust belts of the Southern Central Andes: along-strike variations in shortening, topography, crustal geometry, and denudation. Geol. Soc. Am. Bull. 124 (7–8), 1339–1351.
Giambiagi, L., et al., 2014. Reactivation of Paleozoic structures during Cenozoic deformation in the Cordón del Plata and Southern Precordillera ranges (Mendoza, Argentina). J. Iber. Geol. 40 (2), 309–320.
Giambiagi, L., et al., 2015a. Evolution of shallow and deep structures along the Maipo-Tunuyán transect (33°40´S): from the Pacific coast to the Andean foreland. In: Sepúlveda, S., et al. (Ed.), Geodynamic Processes in the Andes of Central Chile and Argentina, Geol. Soc. London, Special Publication 399. pp. 63–82. https://doi.org/10.1144/SP399.14.
Giambiagi, L., Spagnotto, S., Moreiras, S.M., Gómez, G., Stahlschmidt, E., Mescua, J., 2015b. Three-dimensional approach to understanding the relationship between the Plio-Quaternary stress field and tectonic inversion in the Triassic Cuyo basin, Argentina. Solid Earth 6, 1–17.
Giambiagi, L., Alvarez, P., Spagnotto, S., 2016. Temporal variation of the stress field during the construction of the Central Andes: Constrains from the volcanic arc region (22°-26°S), Western Cordillera, Chile, during the last 20 Ma. Tectonics 35. https://doi.org/10.1002/2016TC004201.
Giambiagi, L., Giambiagi, L., Alvarez, P., Spagnotto, S., Godoy, E., Lossada, A., Mescua, J., Barrionuevo, M., Suriano, J., 2019. Geomechanical model for a seismically active geothermal field: insights from the Tinguiririca volcanic-hydrothermal system. Geosci. Front. https://doi.org/10.1016/j.gsf.2019.02.006.
Giraudo, R., Limachi, R., 2001. Pre-Silurian control in the genesis of the central and southern Bolivian foldbelt. J. S. Am. Earth Sci. 14, 665–680.
Gleason, G.C., Tullis, J., 1995. A flow law for dislocation creep of quartz aggregates determined with the molten salt cell. Tectonophysics 247, 1–23.
Godoy, E., Yáñez, G., Vera, E., 1999. Inversion of an Oligocene volcano-tectonic basin and uplift of its superimposed Miocene magmatic arc, Chilean Central Andes: first seismic and gravity evidence. Tectonophys. 306, 217–326.
Gómez, J., Schobbenhaus, C., Montes, N.E., 2019. Geological Map of South America, scale 1:5 000 000. Commission for the Geological Map of the World (CGMW). Colombian Geological Survey and Geological Survey of Brazil, Paris.
González, G., Niemeyer, H., 2005. Carta Antofagasta y Punta Tetas, Región de Antofagasta. SERNAGEOMIN. Carta No 89. 1 mapa escala 1:100.000. Santiago.
González, G., Cembrano, J., Carrizo, D., Macci, A., Schneider, H., 2003. Link between forearc tectonics and Pliocene-Quaternary deformation of the Coastal Cordillera, Northern Chile. J. S. Am. Earth Sci. 16, 321–342.
González, G., Dunai, T., Carrizo, D., Allmendinger, R., 2006. Young displacements on the Atacama fault system, northern Chile from field observations and cosmogenic 21Ne concentrations. Tectonics 25. https://doi.org/10.1029/2005TC001846.
González, G., Cembrano, J., Aron, F., Veloso, E., Shyu, B., 2009. Coeval compressional deformation and volcanism in the central Andes, case studies from northern Chile (23°-24°S). Tectonics 28. https://doi.org/10.1029/2009TC002538. . TC6003.
González, G., Salazar, P., Loveless, J., Allmendinger, R., Aron, F., Mahesh, S., 2015. Upper plate reverse fault reactivation and the unclamping of the megathrust during the 2014 northern Chile earthquake sequence. Geology 43. https://doi.org/10.1130/G36703.1.
González, R., Espinoza, D., Robledo, F., Jeria, V., Espinoza, M., Torres, P., Rogers, H., 2020. Evidence for two stages of back-arc compression in the late Cretaceous fold-and-thrust belt in the Precordillera of northern Chile (24°30´S-25°30´S). J. S. Am. Earth Sci. https://doi.org/10.1016/j.jsames.2020.102706.
Goss, A., Kay, S.M., Mpodozis, C., 2013. Andean adakite-like high-Mg andesites on the northern margin of the Chilean-Pampean flat-slab (27-28.5°S) associated with frontal arc migration and fore-arc subduction erosion. J. Petrol. 54, 2193–2234.
Graeber, F., Asch, G., 1999. Three-dimensional models of P wave velocity and P-to-S velocity ratio in the southern central Andes by simultaneous inversion of local earthquake data. J. Geophys. Res. 104. . no. b9. pages 20,237-20,256, september 10, 1999.
Grevemeyer, I., Diaz-Naveas, J.L., Ranero, C.R., Villinger, H.W., Leg, O.D.P., 2003. Heat flow over the descending Nazca plate in central Chile, 32 S to 41 S: Observations from ODP Leg 202 and the occurrence of natural gas hydrates. Earth Planet. Sci. Lett. 213 (3–4), 285–298.
Grevemeyer, I., Kaul, N., Diaz-Naveas, J.L., Villinger, H.W., Ranero, C.R., Reichert, C., 2005. Heat flow and bending-related faulting at subduction trenches: case studies offshore of Nicaragua and Central Chile. Earth Planet. Sci. Lett. 236 (1–2), 238–248.
Grevemeyer, I., Kaul, N., Diaz-Naveas, J.L., 2006. Geothermal evidence for fluid flow through the gas hydrate stability field off Central Chile—transient flow related to large subduction zone earthquakes? Geophys. J. Int. 166 (1), 461–468.
Gubbels, T.L., Isacks, B.L., Farrar, E., 1993. High-level surfaces, plateau uplift, and foreland development, Bolivian central Andes. Geology 21, 695–698.
Gutscher, M.-A., Spakman, W., Bijwaard, H., Engdahl, R., 2000. Geodynamics of flat subduction: Seismicity and tomographic constraints from the Andean margin. Tectonics 9, 814–833.
Haberland, Ch., Rietbrock, A., 2001. Attenuation tomography in the western central Andes: A detailed insight into the structure of a magmatic arc. J. Geophys. Res. Solid Earth 106. . 11,151-11,167.
Haddon, A., Porter, R., 2018. S-Wave receiver function analysis of the Pampean flat-slab region: evidence for a torn slab. Geochem. Geophys. Geosyst. 19 (10), 4021–4034.
Halter, W.E., Bain, N., Becker, K., Heinrich, C.A., Landtwing, M., Von Quadt, A., Bissig, T., Clark, A.H., Sasso, A.M., Tosdal, R.M., 2004. From andesitic volcanism to the formation of a porphyry Cu-Au mineralizing magma chamber: the Farallón Negro Volcanic Complex, NW Argentina. J. Volcanol. Geotherm. Res. 136, 1–30.
Hamza, V.M., Muñoz, M., 1996. Heat flow map of South America. Geothermics 25 (6), 599–646.
Hamza, V.M., Dias, F.J.S., Gomes, A.J., Terceros, Z.G.D., 2005. Numerical and functional representations of regional heat flow in South America. Phys. Earth Planet. Inter. 152 (4), 223–256.
Harris, A.C., Allen, C.M., Bryan, S.E., Campbell, I.H., Holcombe, R.J., Palin, J.M., 2004. ELA-ICP-MS U-Pb zircon geochronology of regional volcanism hosting the Bajo de la Alumbrera Cu-Au deposit: implications for porphyry-related mineralization. Mineral. Deposita 39, 46–67.
Harry, D.L., Oldow, J.S., Sawyer, D.S., 1995. The growth of orogenic belts and the role of crustal heterogeneities in decollement tectonics. Geol. Soc. Am. Bull. 107, 1411–1426.
Haschke, M., Gunther, A., 2003. Balancing crustal thickening in arcs by tectonic vs. magmatic means. Geology 31, 933–936.
Haschke, M., Siebel, W., Gunther, A., Scheuber, E., 2002. Repeated crustal thickening and recycling during the Andean orogeny in north Chile (21°–26°S). J. Geophys. Res. 107, 2019. https://doi.org/10.1029/2001JB000328.
Haschke, M., Deeken, A., Insel, N., Sobel, E., Grove, M., Schmitt, A., 2005. Growth pattern of the Andean Puna plateau constrained by apatite fission track, apatite (U-Th)/He, K-feldspar 40Ar/39Ar, and zircon U-Pb geochronology. In: Proceedings of the 6th Int. Symposium Andean Geodyn. pp. 360–363.
Heit, B., Koulakov, I., Asch, G., Yuan, X., Kind, R., Alcozer-Rodriguez, I., Tawackoli, S., Wilke, H., 2008. More constraints to determine the seismic structure beneath the Central Andes at 21°S using teleseismic tomography analysis. J. S. Am. Earth Sci. 25, 22–36.

Henriquez, S., DeCelles, P.G., Carrapa, B., 2019. Cretaceous to middle Cenozoic exhumation history of the Cordillera de Domeyko and Salar de Atacama basin, northern Chile. Tectonics 38, 395–416. https://doi.org/10.1029/2018TC005203.
Henriquez, S., DeCelles, P.G., Carrapa, B., Hughes, A.N., Davis, G.H., Alvarado, P., 2020. Deformation history of the Puna plateau, Central Andes of northwestern Argentina. J. Struct. Geol. 140. https://doi.org/10.1016/j.jsg.2020.104133.
Henry, S.G., Pollack, H.N., 1988. Terrestrial heat flow above the Andean subduction zone in Bolivia and Peru. J. Geophys. Res. Solid Earth 93 (B12), 15153–15162.
Heredia, N., Rodriguez Fernández, L.R., Gallastegui, G., Busquets, P., Colombo, F., 2002. Geological setting of the Argentine Frontal Cordillera in the flat-slab segment (30°00'–31°30'S latitude). J. S. Am. Earth Sci. 15, 79–99.
Herrera, C., Cassidy, J.F., Dosso, S.E., Dettmer, J., Bloch, W., Sippl, C., Salazar, P., 2021. The crustal stress field inferred from focal mechanisms in northern Chile. Geophys. Res. Lett. 48. https://doi.org/10.1029/2021GL092889. . e2021GL092889.
Hervé, M., Sillitoe, R.H., Wong, C., Fernández, P., Crignola, F., Ipinza, M., Urzúa, F., 2012. Geologic overview of the Escondidad porphyry copper district, northern Chile. Soc. Econ. Geol. Spec. Public. 16, 55–78.
Heuret, A., Lallemand, S., 2005. Plate motions, slab dynamics and back-arc deformation. Phys. Earth Planet. Inter. 149, 31–51. https://doi.org/10.1016/j.pepi.2004.08.022.
Hilairet, N., Reynard, B., Wang, Y., Daniel, I., Merkel, S., Nishiyama, N., Petitgirard, S., 2007. High-pressure creep of serpentine, interseismic deformation, and initiation of subduction. Science 318 (5858), 1910–1913.
Hindle, D., Kley, J., 2003. Displacements, strains and rotations in the Central Andean Plate Boundary Zone. In: Stein, S., Freymuller, J. (Eds.), Plate Boundary Zones, AGU Geodynamics Series 30. American Geophysical Union, pp. 135–144.
Hirth, G., Kohlstedt, D.L., 2003. Rheology of the upper mantle and the mantle wedge: a view from the experimentalists. Geophys. Monogr. Ser. 138, 83–105.
Hoke, G.D., Giambiagi, L., Garzione, C., Mahoney, B., Strecker, M., 2014. Neogene paleoelevation of intermontane basins in a narrow, compressional mountain range, southern Central Andes of Argentina, Earth Planet. Sci. Lett. 406, 153–164.
Hoke, G.D., Graber, N.R., Mescua, J.F., Giambiagi, L.B., Fitzgerald, P.G., Metcalf, J.R., 2015. Near Pure Surface Uplift of the Argentine Frontal Cordillera: insights from (U–Th/ He) thermochronology and geomorphic analysis. In: Sepúlveda, S., et al. (Ed.), Geodynamic Processes in the Andes of Central Chile and Argentina. Geol. Soc. London, Spec. Publ 399. pp. 383–399. https://doi.org/10.1144/SP399.4.
Hongn, F., Sobel, E.R., Coutand, I., Haschke, M., Riller, U., Strecker, M.R., 2007. Middle Eocene deformation and sedimentation in the Puna-Eastern Cordillera transition (23–26°S): control by preexisting heterogeneities on the pattern of initial Andean shortening. Geology 35, 271–274. https://doi.org/10.1130/G23189A.1.
Hongn, F., Mon, R., Petrinovic, I., del Papa, C., Powell, J., 2010. Inversión y reactivación tectónicas cretácico-cenozoicas en el noroeste argentino: influencia de las heterogeneidades del basamento Neoproterozoico-Paleozoico inferior. Rev. Asoc. Geol. Argent. 66, 38–53.
Horton, B.K., 1998. Sediment accumulation on top of the Andean orogenic wedge: oligocene to late Miocene basins of the Eastern Cordillera, southern Bolivia. Geol. Soc. Am. Bull. 110, 1174–1192.
Horton, B.K., 2005. Revised deformation history of the central Andes: inferences from Cenozoic foredeep and intermontane basins of the Eastern Cordillera, Bolivia. Tectonics 24, TC3011. https://doi.org/10.1029/2003TC001619.
Horton, B., 2018. Tectonic regimes of the central and southern Andes: responses to variations in plate coupling during subduction. Tectonics 37, 402–429. (2018). https://doi.org/10.1002/2017TC004624.
Horton, B.K., DeCelles, P.G., 2001. Modern and ancient fluvial megafans in the foreland basin systems of the central Andes, southern Bolivia: implications for drainage network evolution fold-thrust belts. Basin Res. 13, 43–63.
Horton, B.K., Fuentes, F., Boll, A., Starck, D., Ramirez, S.G., Stockli, D.F., 2016. Andean stratigraphic record of the transition from backarc extension to orogenic shortening: a case study from the northern Neuquén Basin, Argentina. J. S. Am. Earth Sci. 71, 17–40.
Houseman, G.A., McKenzie, D.P., Molnar, P., 1981. Convective instability of a thickened boundary layer and its relevance for the thermal evolution of continental convergent belts. J. Geophys. Res. 86, 6115–6132.
Husson, L., Conrad, C., Faccenna, C., 2012. Plate motions, Andean orogeny, and volcanism above the South Atlantic convection cell. Earth Planet. Sci. Lett. 317–318, 126–135.
Iaffaldano, G., Bunge, H.-P., Dixon, T.H., 2006. Feedback between mountain belt growth and plate convergence. Geology 34, 893–896.
Ibarra, F., Liu, S., Meeßen, C., Prezzi, C.B., Bott, J., Scheck-Wenderoth, M., Sobolev, S., Strecker, M.R., 2019. 3D data-derived lithospheric structure of the Central Andes and its implications for deformation: insights from gravity and geodynamics modeling. Tectonophys. 766, 453–468.
Ibarra, F., Prezzi, C.B., Bott, J., Scheck-Wenderoth, M., Strecker, M., 2021. Distribution of temperature and strength in the Central Andean lithosphere and its relationship to seismicity and active deformation. J. Geophys. Res. Solid Earth 126. https://doi.org/10.1029/2020JB021231. . e2020JB021231.
Introcaso, A., Pacino, M.C., Fraga, H., 1992. Gravity, isostasy and Andean crustal shortening between latitudes 30 and 35°S. Tectonophys. 205, 31–48.
Irigoyen, M.V., Buchan, K.L., Brown, R.L., 2000. Magnetostratigraphy of Neogene Andean foreland-basin strata, lat 33°S, Mendoza Province, Argentina. Geol. Soc. Am. Bull. 112, 803–816.
Isacks, B.L., 1988. Uplift of the Central Andean Plateau and bending of the Bolivian Orocline. J. Geophys. Res. 93, 3211–3231.
Isacks, B.L., Barazangi, M., 1977. Geometry of Benioff zones: Lateral segmentation and downward bending of the subducted lithosphere, in Island arcs, Deep Sea Trenches and Back arc basins. In: Talwani, M., Pitman, W. (Eds.), AGU. Washington, D.C, pp. 99–114.
Jamieson, R.A., Beaumont, C., 2013. On the origin of orogens. Geol. Soc. Am. Bull. 125, 1671–1702.
Jammes, S., Huismans, R., 2012. Structural styles of mountain building: Controls of lithospheric rheologic stratification and extensional inheritance. J. Geophys. Res. 117, B10403. https://doi.org/10.1029/2012JB009376.
Jaquet, Y., Duretz, T., Grujic, D., Masson, H., Schmalholz, S.M., 2018. Formation of orogenic wedges and crustal shear zones by thermal softening, associated topographic evolution and application to natural orogens. Tectonophys. 746, 512–529.
Jara, P., Charrier, R., 2014. Nuevos antecedentes geocronológicos y estratigráficos en la Cordillera Principal de Chile central entre 32° y 32°300S Implicancias paleogeográficas y estructurales. Andean. Geology 41 (1). https://doi.org/10.5027/andgeoV41n1-a07.
Jensen, E., Cembrano, J., Faulkner, D., Veloso, E., Arancibia, G., 2011. Development of a self-similar strike-slip duplex system in the Atacama fault system, Chile. J. Struct. Geol. 33, 1611–1626.
Johnson, N.M., Jordan, T.E., Johnsson, P.A., Naeser, C.W., 1986. Magnetic polarity stratigraphy, age and tectonic setting of fluvial sediments in an Eastern Andean Foreland Basin, San Juan Province, Argentina. In: Foreland Basins. Blackwell Publishing Ltd., Oxford, UK, pp. 63–75. https://doi.org/10.1002/9781444303810.ch3.
Jones, R.E., Kirstein, L.A., Kasemann, S.A., Litvak, V.D., Poma, S., Alonso, R.N., Hinton, R., 2016. The role of changing geodynamics in the progressive contamination of Late Cretaceous to Late Miocene arc magmas in the southern Central Andes. Lithos 262, 169–191.
Jordan, T.E., Allmendinger, R.W., 1986. The Sierras Pampeanas of Argentina: a modern analogue of Rocky Mountain foreland deformation. Amer. J. Sci. 286 (10), 737–764. https://doi.org/10.2475/ajs.286.10.737.
Jordan, T.E., Alonso, R.N., 1987. Cenozoic stratigraphy and basin tectonics of the Andes mountains, 20° -28° south latitude. Am. Assoc. Pet. Geol. Bull. 71, 49–64. https://doi.org/10.1306/94886D44-1704-11D7-8645000102C1865D.
Jordan, T.E., Isacks, B.L., Allmendinger, R.W., Brewer, J.A., Ramos, V.A., Ando, C.J., 1983. Andean tectonics related to geometry of subducted Nazca Plate. Geol. Soc. Am. Bull. 94 (3), 341–361.
Jordan, T.E., Allmendinger, R.W., Damanti, J.F., Drake, R.E., 1993. Chronology of motion in a complete thrust belt: the Precordillera, 30–31°S, Andes Mountains. J. Geol. 101 (2), 135–156. . (1993).
Jordan, T.E., Schlunegger, F., Cardozo, N., 2001. Unsteady and spatially variable evolution of the Neogene Andean Bermejo foreland basin, Argentina. J. S. Am. Earth Sci. 14, 775–798. https://doi.org/10.1016/S0895- 9811(01)00072-4.
Jordan, T.E., Mpodozis, C., Munoz, N., Blanco, N., Pananont, P., Gardeweg, M., 2007. Cenozoic subsurface stratigraphy and structure of the Salar de Atacama Basin, northern Chile. J. S. Am. Earth Sci. 23, 122–146.
Jordan, T.E., Kirk-Lawlor, N.E., Blanco, N.P., Rech, J.A., Cosentino, N.J., 2014. Landscape modification in response to repeated onset of hyperarid paleoclimate states since 14 Ma, Atacama Desert, Chile. Geol. Soc. Am. Bull. 126 (7–8), 1016–1046.
Juez-Larré, J., Kukowski, N., Dunai, T., Hartley, A., Andriessen, P., 2010. Thermal and exhumation history of the Coastal Cordillera arc of northern Chile revealed by thermochronological dating. Tectonophysics 495, 48–66.
Kay, S.M., Coira, B., 2009. Shallowing and steepening subduction zones, continental lithosphere loss, magmatism and crustal flow under the central Andean Altiplano–Puna plateau, in: Backbone of the Americas: Shallow Subduction, Plateau and Ridge and Terrane Collisions. Geol. Soc. Ame. 204, 229–260.
Kay, R.W., Kay, S.M., 1993. Delamination and delamination magmatism. Tectonophys 219, 177–189.
Kay, S., Kurtz, A., 1995. Magmatic and tectonic characterization of the El Teniente region: Internal report, Superintendencia de Geología, El Teniente, CODELCO, 180 p.
Kay, S.M., Mpodozis, C., 2001. Central Andean ore deposits linked to evolving shallow subduction systems and thickening crust. GSA Today 11, 4. https://doi.org/10.1130/1052-5173(2001)0112.0.CO;2.
Kay, S.M., Mpodozis, C., 2002. Magmatism as a probe to the Neogene shallowing of the Nazca plate beneath the modern Chilean flat-slab. J. S. Am. Earth Sci. 15, 39–57.
Kay, S., Maksaev, V., Moscoso, R., Mpodozis, C., Nasi, C., Gordillo, C.E., 1988. Tertiary Andean magmatism in Chile and Argentina between 28°S and 33°S: Correlation of magmatic chemistry with a changing Benioff zone. J. S. Am. Earth Sci. 1, 21–38.
Kay, S.M., Coira, B., Viramonte, J., 1994a. Young mafic back arc volcanic rocks as indicators of continental lithospheric delamination beneath the Argentine Puna Plateau, Central Andes. J. Geophys. Res. 99, 24323–24339.
Kay, S.M., Mpodozis, C., Tittler, A., Cornejo, P., 1994b. Tertiary magmatic evolution of the Maricunga mineral belt in Chile. Int. Geol. Rev. 36 (12), 1079–1112.
Kay, S.M., Mpodozis, C., Coira, B., 1999. Magmatism, tectonism, and mineral deposits of the central Andes (22°-33°S). In: Skinner, B. (Ed.), Geology and Ore Deposits of the Central Andes. Soc. Econom. Geol. Special Public., 7, pp. 27–59.
Kay, S.M., Godoy, E., Kurtz, A., 2005. Episodic arc migration, crustal thickening, subduction erosion, and magmatism in the south-central Andes. Geol. Soc. Am. Bull. 117, 67–88.
Kay, S.M., Ramos, V.A., Dickinson, W., 2009. Backbone of the Americas: shallow subduction, plateau uplift, and ridge and terrane collision. Geol. Soc. Am. Memoir 204. . 279 pp.
Kay, S.M., Mpodozis, C., Gardeweg, M., 2013. Magma sources and tectonic setting of Central Andean andesites (25.5 – 28°S) related to crustal thickening, forearc subduction erosion and delamination. Geol. Soc. London, Special Public. 385. https://doi.org/10.1144/SP385.11.
Kelly, J.G., 1961. Geología de las sierras de Moquina y perspectivas petrolíferas, Dto. de Jáchal, Provincia de San Juan, YPF, Gerencia Exploración Buenos Aires.
Kennan, L., Lamb, S., Rundle, C., 1995. K-Ar dates from the Altiplano and Cordillera Oriental of Bolivia: implications for Cenozoic stratigraphy and tectonics. J. S. Am. Earth Sci. 8, 163–186.

Kirby, S.H., Durham, W.B., Stern, L.A., 1991. Mantle phase changes and deep-earthquake faulting in subducting lithosphere. Science 252, 216–225.
Kley, J., 1996. Transition from basement-involved to thin-skinned thrusting in the Cordillera Oriental of southern Bolivia. Tectonics 15, 763–775.
Kley, J., 1999. Geologic and geometric constraints on a kinematic model of the Bolivian orocline. J. S. Am. Earth Sci. 12, 221–235.
Kley, J., Monaldi, C.R., 1998. Tectonic shortening and crustal thickness in the central Andes: how good is the correlation? Geology 26, 723–726.
Kley, J., Monaldi, C.R., 2002. Tectonic inversion in the Santa Barbara System of the central Andean foreland thrust belt, northwestern Argentina. Tectonics 21. https://doi.org/10.1029/2002TC902003.
Kley, J., Reinhardt, M., 1994. Geothermal and tectonic evolution of the Eastern Cordillera and the Subandean ranges of southern Bolivia. In: Tectonics of the Southern Central Andes: Structure and Evolution of an Active Continental Margin. Springer-Verlag, Berlin, pp. 155–170.
Kley, J., Müller, J., Tawackoli, S., Jacobshagen, V., Manutsoglu, E., 1997. Pre-Andean and Andean age deformation in the eastern Cordillera of southern Bolivia. J. S. Am. Earth Sci. 10, 1–19. https://doi.org/10.1016/S0895-9811(97)00001-1.
Kley, J., Rossello, E.A., Monaldi, C.R., Habighorst, B., 2005. Seismic and field evidence for selective inversion of Cretaceous normal faults, Salta rift, northwest Argentina. Tectonophys. 399, 155–172.
Kozlowski, E., Manceda, R., Ramos, V.A., 1993. Estructura. In: Ramos, V.A. (Ed.), Geología y Recursos Naturales de Mendoza. Asoc. Geol, Argentina, Buenos Aires, pp. 235–256.
Krystopowicz, N.J., Currie, C.A., 2013. Crustal eclogitization and lithosphere delamination in orogens. Earth Planet. Sci. Lett. 361, 195–207. https://doi.org/10.1016/j.epsl.2012.09.056.
Kudrass, H.R., Delisle, G., Goergens, A., Heeren, F., von Huene, R., Jensen, A., Marzan, I., 1995. Crustal investigations off-and onshore, Nazca/Central Andes (CINCA), Bundesanstalt für Geowissenschaften und Rohstoffe Hannover (Germany). Report Sonne-Cruise 104.
Kurtz, A., Kay, S.M., Charrier, R., Farrar, E., 1997. Geochronology of Miocene plutons and exhumation history of the el Teniente region, Central Chile (34°–35°S). Rev. Geol. Chile 24 (1), 75–90.
Lacombe, O., Bellahsen, N., 2016. Thick-skinned tectonics and basement-involved fold-thrust belts. Insights from selected Cenozoic orogens. Geol. Mag. 1, 1–48. https://doi.org/10.1017/S0016756816000078.
Ladino, M., Tomlinson, A., Blanco, N., 1999. New constraints for the age of the Cretaceous compressional deformation in the Andes of northern Chile (Sierra de Moreno, 21°-22°10´S). In: Proceedings of the 4th International Symposium on Andean Geodynamics, Göttingen, Germany. pp. 407–410. Paris.
Lamb, S., Hoke, L., 1997. Origin of the high plateau in the central Andes, Bolivia, South America. Tectonics 16, 623–649.
Lamb, S., Hoke, L., Kennan, L., Dewey, J., 1997. Cenozoic evolution of the Central Andes in Bolivia and northern Chile. In: Burg, J.P., Ford, M. (Eds.), Orogeny Through Time. Geol. Soc. Spec. Pub., 121, pp. 237–264.
Lanza, F., Tibaldi, A., Bonali, F.L., Corazzato, C., 2013. Space-time variations of stresses in the Miocene-Quaternary along the Calama-Olacapato-El Toro fault zone, Central Andes. Tectonoph. 593 (33), 56.
Levina, M., Horton, B.K., Fuentes, F., Stockli, D.F., 2014. Cenozoic sedimentation and exhumation of the foreland basin system preserved in the Precordillera thrust belt (31–32°S), southern central Andes, Argentina. Tectonics 33. https://doi.org/10.1002/2013TC003424.
Limarino, C.O., Fauqué, L.A., Cardó, R., Gagliardo, M.L., Escoteguy, L., 2002. La faja volcánica miocena de la Precordillera septentrional. Rev. Asoc. Geol. Argentina 57, 289–304.
Lindsay, D., Zentilli, M., Rojas de la Rivera, J., 1995. Evolution of an active ductile to brittle shear system controlling mineralization at the Cuquicamata porphyry copper deposits, northern Chile. Int. Geol. Rev. 37, 945–995.
Litherland, M., Klinck, B.A., O´Connor, E.A., Pitfield, P., 1985. Andean-trending mobile belts in the Brazilian Shield. Nature 314, 345–348.
Liu, S., Currie, C.A., 2016. Farallon plate dynamics prior to the Laramide orogeny: numerical models of flat subduction. Tectonophysics 666, 33–47.
Löbens, S., Sobel, E.R., Bense, F.A., Wemmer, K., Dunkl, I., Siegesmund, S., 2013. Refined thermochronological aspects of the Northern Sierras Pampeanas. Tectonics 32 (3), 453–472. https://doi.org/10.1002/tect.20038.
López, C., Martínez, F., Del Ventisette, C., Bonini, M., Montanari, D., Muñoz, B., Riquelme, R., 2020. East-vergent thrusts and inversion structures: an updated tectonic model to understand the Domeyko Cordillera and the Salar de Atacama basin transition in the western Central Andes. J. S. Am. Earth Sci. 103. https://doi.org/10.1016/j.jsames.2020.102741.
Lossada, A.C., Giambiagi, L., Hoke, G.D., Fitzgerald, P.G., Creixell, C., Murillo, I., Mardonez, D., Velásquez, R., Suriano, J., 2017. Thermochronologic evidence for Late Eocene Andean mountain building at 30°S. Tectonics 36, 2693–2713. https://doi.org/10.1002/2017TC004674.
Lossada, A., Hoke, G.D., Giambiagi, L.B., Fitzgerald, P.G., Mescua, J.F., Suriano, J., Aguilar, A., 2020. Detrital thermochronology reveals major middle Miocene exhumation of the eastern flank of the Andes, predating the Pampean flat-slab (33°-33.5°S). Tectonics. https://doi.org/10.1029/2019TC005764.
Lunkenheimer, F., 1930. El terremoto submendocino del 30 de mayo de 1929. Observatorio Astronómico de La Plata. Contribuciones Geofísicas Tomo III, N° 2. La Plata.
Lynner, C., Beck, S., Zandt, G., Porritt, R., Lin, F.-C., Eilon, Z., 2018. Midcrustal deformation in the Central Andes constrained by radial anisotropy. J. Geophys. Res. Solid Earth 123, 4798–4813. https://doi.org/10.1029/2017JB014936.
Lyon-Caen, H., Molnar, P., Suárez, G., 1985. Gravity anomalies and flexure of the Brazilian Shield beneath the Bolivian Andes. Earth Planet. Sci. Lett. 75, 81–92. https://doi.org/10.1016/0012-821X(85)90053-6.
Mackaman-Lofland, C., Horton, B.K., Fuentes, F., Constenius, K.N., Stockli, D.F., 2019. Mesozoic to Cenozoic retroarc basin evolution during changes in tectonic regime, southern Central Andes (31–33°S): Insights from zircon U-Pb geochronology. J. S. Am. Earth Sci. 89, 299–318. https://doi.org/10.1016/j.jsames.2018.10.004.
Mackaman-Lofland, C., et al., 2020. Andean mountain building and foreland basin evolution during thin- and thick-skinned Neogene deformation (32−33°S). Tectonics 39. https://doi.org/10.1029/2019TC005838. . e2019TC005838.
Maggi, A., Jackson, J., McKenzie, D., Priestley, K., 2000. Earthquake focal depths, effective elastic thickness, and the strength of the continental lithosphere. Geology 28, 495–498.
Maksaev, V., Marinovic, N., 1980. Cuadrángulos Cerro de la Mica, Quillagua, Cerro Posada y Oficina Prosperidad, Región de Antofagasta, Instituto de Investigaciones Geológicas, Carta Geológica de Chile, pp. 45–48. 63 pp.
Maksaev, V., Zentilli, M., 1988. Marco metalogénico regional de los megadepósitos de tipo pórfido cuprífero del norte grande de Chile. In: Proceedings of the 5th Congreso Geológico Chileno, 1, B181-B212.
Maksaev, V., Zentilli, M., 1999. Fission track thermochronology of the Domeyko Cordillera, Northern Chile: Implications for Andean tectonics and porphyry copper metallogenesis. Explor. Min. Geol. 8, 65–89.
Maksaev, V., Moscoso, R., Mpodozis, C., Nasi, C., 1984. Las unidades volcánicas y plutónicas del Cenozoico superior en la alta Cordillera del Norte Chico (29°-31°S): Geología, alteración hidrotermal y mineralización. Rev. Geol. Chile 21, 11–51.
Maksaev, V., Munizaga, F., McWilliams, M., Fanning, M., Mathur, R., Ruiz, J., Zentilli, M., 2004. New chronology for El Teniente, Chilean Andes, from U/Pb, 40Ar/39Ar, Re-Os and fission track dating: implications for the evolution of a supergiant porphyry Cu-Mo deposit. In: Sillitoe, R.H., Perelló, J., Vidal, C.E. (Eds.), Andean Metallogeny: New Discoveries, Concepts and Updates, 11. Society of Economic Geologists, p. 5. Soc. Econom. Geol., Special Public.
Mardones, V., Peña, M., Pairoa, S., Ammirati, J.-B., Leisen, M., 2021. Architecture, kinematics, and tectonic evolution of the principal cordillera of the Andes in central Chile (~33.5°S): Insights from detrital zircon U-Pb geochronology and seismotectonics implications. Tectonics 40. https://doi.org/10.1029/2020TC006499. . e2020TC006499.
Mardonez, D., 2020. Relación entre estructuras profundas y someras a lo largo de la transecta La Serena-Jáchal (30°S), Andes Centrales Sur. PhD thesis. Universidad Nacional de Córdoba, Argentina.
Mardonez, D., Suriano, J., Giambiagi, L.B., Mescua, J.F., Lossada, A.C., Creixell, C., Murillo, I., 2020. Cenozoic structural evolution of the 30°S transect, between the Frontal Cordillera and the Western Sierras Pampeanas, Argentina. J. S. Am. Earth Sci. 104. https://doi.org/10.1016/j.jsames.2020.102838.
Marinovic, N., 2007. Carta Oficina Domeyko, Región de Antofagasta. SERNAGEOMIN. Carta Geológica de Chile, Serie Geología Básica 105, p 41 (1: 100.000).
Marinovic, N., Lahsen, A., 1984. Hoja Calama, Región de Antofagasta. Servicio Nacional de Geología y Minería, Carta Geológica de Chile 58. 140 p., 1 mapa escala 1:250.000. Santiago.
Marquillas, R.A., del Papa, C., Sabino, I.F., 2005. Sedimentary aspects and paleoenvironmental evolution of a rift basin: Salta Group (Cretaceous-Paleogene), northwestern Argentina. Int. J. Earth Sci. 94 (1), 94–113. https://doi.org/10.1007/s00531-004-0443-2.
Martin, M.W., Clavero, J., Mpodozis, C., Cuitiño, L., 1995. Estudio geológico de la franja El Indio, Cordillera de Coquimbo. SERNAGEOMIN, Informe Registrado IR-95-6, pp. 1–238. Santiago.
Martin, M.W., Clavero, J., Mpodozis, C., 1997. Eocene to late Miocene structural development of Chile´s El Indio gold belt, ~30°S. In: Proceedings of the 8th Congreso Geológico Chileno 1. pp. 144–148. Antofagasta, Chile.
Martínez, C., Soria, E., Uribe, H., Escoba, A., Hinajosa, A., 1994. Estructura y evolución del Altiplano sur occidental: el sistema de cabalgamientos de Uyuni-Khenayani y su relación con la sedimentación terciaria. Revista Técnica de YPFB 15 (3–4), 245–264.
Martínez, F., Arriagada, C., Peña, M., Deckart, K., Charrier, R., 2016. Tectonic styles and crustal shortening of the Central Andes "Pampean" flat-slab segment in northern Chile (27–29°S). Tectonophysics 667 (23), 144–162. https://doi.org/10.1016/j.tecto.2015.11.019.
Martínez, F., López, C., Parra, M., Espinoza, D., 2019. Testing the occurrence of thick-skinned triangle zones in the Central Andes forearc: Example from the Salar de Punta Negra Basin in northern Chile. J. Struct. Geol. 120, 14–28. https://doi.org/10.1016/j.jsg.2018.12.009.
Martínez, F., López, C., Parra, M., 2020. Effects of Pre-Orogenic Tectonic Structures On The Cenozoic Evolution Of Andean Deformed Belts: Evidence From The Salar De Punta Negra Basin In The Central Andes Of Northern Chile. Basin Res. https://doi.org/10.1111/bre.12436.
Martínez, F., Peña, M., Parra, M., López, C., 2021. Contraction and exhumation of the western Central Andes induced by basin inversion: new evidence from "Pampean" subduction segment. Basin Res. 33 (5), 2706–2724.
Martinod, J., Gérault, M., Husson, L., Regards, V., 2020. Widening of the Andes: an interplay between subduction dynamics and crustal wedge tectonics. Earth Sci. Rev. https://doi.org/10.1016/j.earscirev.2020.103170.
Martos, F.E., et al., 2022. Neogene evolution of the Aconcagua fold-and-thrust belt: linking structural, sedimentary analyses and provenance U-Pb detrital zircon data for the Penitentes basin. Tectonophysics 825, 229233.
Massoli, D., Koyi, H., Barchi, M., 2006. Structural evolution of a fold and thrust belt generated by multiple decollements: analogue models and natural examples from the Northern Apennines (Italy). J. Struct. Geol. 28, 185–199.
Matteini, M., Mazzuoli, R., Omarini, R., Cas, R.A., Maas, R., 2002. Geodynamical evolution of the Central Andes at 24°S as inferred by magma composition along the

Calama-Olacapato-El Toro transversal volcanic belt. J. Volcanol. Geotherm. Res. 118, 205–228.
McFarland, P.K., Bennett, R.A., Alvarado, P., DeCelles, P.G., 2017. Rapid geodetic shortening across the Eastern Cordillera of NW Argentina observed by the Puna-Andes GPS Array. J. Geophys. Res. 122, 8600–8623. https://doi.org/10.1002/2017JB014739.
McGlashan, N., Brown, L., Kay, S., 2008. Crustal thickness in the central Andes from teleseismically recorded depth phase precursors. Geophys. J. Int. 175, 1013–1022.
McQuarrie, N., 2002. The kinematic history of the central Andean fold-thrust belt, Bolivia: implications for building a high plateau. Geol. Soc. Am. Bull. 114, 950–963. https://doi.org/10.1130/0016-7606.
McQuarrie, N., Davis, G.H., 2002. Crossing the several scales of strain-accomplishing mechanisms in the hinterland of the central Andes fold-thrust belt, Bolivia. J. Struct. Geol. 24, 1587–1602.
McQuarrie, N., DeCelles, P.G., 2001. Geometry and structural evolution of the central Andean. Tectonics 20, 669–692. https://doi.org/10.1029/2000TC001232.
McQuarrie, N., Horton, B., Zandt, G., Beck, S., DeCelles, P., 2005. Lithospheric evolution of the Andean fold-thrust belt, Bolivia, and the origin of the Central Andean Plateau. Tectonophys. 399, 15–37. https://doi.org/10.1016/j.tecto.2004.12.013.
Meigs, A.J., Nabelek, J., 2010. Crustal-scale pure shear foreland deformation of western Argentina. Geophys. Res. Lett. 37, L11304. https://doi.org/10.1029/2010GL043220.
Mescua, J.F., Giambiagi, L., Ramos, V.A., 2013. Late Cretaceous uplift in the Malargüe fold-and-thrust belt (35° S), southern central Andes of Argentina and Chile. Andean Geol. 40, 102–116.
Mescua, J., Giambiagi, L., Tassara, A., Gimenez, M., Ramos, V.A., 2014. Influence of pre-Andean history over Cenozoic foreland deformation: structural styles in the Malargüe fold-and-thrust belt at 35°S. Andes of Argentina. Geosphere 10 (3), 585–609.
Mingramm, A., Russo, A., Pozzo, A., Cazau, L., 1979. Sierras subandinas. In: Turner, J. (Ed.), Geología Regional Argentina, Academia Nacional de Ciencias, Córdoba. pp. 95–138. (1979).
Molnar, P., England, P., 1990. Temperatures, heat flux, and frictional stress near major thrust faults. J. Geophys. Res. Solid Earth 95 (B4), 4833–4856.
Mon, R., Hongn, F., 1991. The structure of the Precambrian and lower Paleozoic basement of the Central Andes between 22° and 32°S. Latin Geologische Rundschau 80, 745–758.
Mon, R., Salfity, J.A., 1995. Tectonic evolution of the Andes of northern Argentina. In: Petroleum Basins of South America, edited by A. J. Tankard et al., Ame. Assoc. Petr. Geol. Mem, 62, pp. 269–283.
Montero-López, C., del Papa, C.E., Hongn, F.D., Strecker, M.R., Aramayo, A., 2016. Synsedimentary broken foreland tectonics during the Paleogene in the Andes of NW Argentine: new evidence from regional to centimetre-scale deformation features. Basin Res. 1–18. https://doi.org/10.1111/bre.12212.
Montero-López, C., et al., 2020. Development of an incipient Paleogene topography between the present-day Eastern Andean Plateau (Puna) and the Eastern Cordillera, southern Central Andes, NW Argentina. Basin Res. 33 (2), 1194–1217.
Morency, C., Doin, M.P., 2004. Numerical simulations of the mantle lithosphere delamination. J. Geophys. Res. 109, B03410. https://doi.org/10.1029/2003JB002414.
Mortimer, E., Carrapa, B., Coutand, I., Schoenbohm, L., Sobel, E.R., Sosa Gomez, J., Strecker, M.R., 2007. Fragmentation of a foreland basin in response to out-ofsequence basement uplifts and structural reactivation; El Cajon-Campo del Arenal Basin, NW Argentina. Geol. Soc. Am. Bull. 119, 637–653. https://doi.org/10.1130/B25884.1.
Moscoso, R., Mpodozis, C., 1988. Estilos estructurales en el Norte Chico de Chile (28°-31°S), Regiones de Atacama y Coquimbo. Rev. Geol. Chile 25, 151–166.
Mouthereau, F., Lacomb, O., Meyer, B., 2006. The Zagros folded belt (Fars, Iran): constrains from topography and critical wedge modelling. Geophys. J. Int. 165, 336–356.
Mouthereau, F., et al., 2007. Placing limits to shortening evolution in the Pyrenees: Role of margin architecture and implications for the Iberia/Europe convergence. Tectonics 26. https://doi.org/10.1002/2014TC003663.
Mpodozic, C., Marinovic, N., Smoje, I., Cuitiño, L., 1993. Estudio geológico-estructural de la Cordillera de Domeyko entre Sierra Limón Verge y Sierra Mariposas, Región de Antofagasta. Sernageomin-Codelco. 282 pp., Santiago.
Mpodozis, C., Cornejo, P., 1986. Hoja Pisco-Elqui. SERNAGEOMIN. Carta No. 68.
Mpodozis, C., Cornejo, P., 2012. Cenozoic tectonics and porphyry copper systems of the Chilean Andes. Soc. Econom. Geol., Special Public. 16. pp. 329–360.
Mpodozis, C., Kay, S.M., 2009. Evolution of less than 10 Ma Valle Ancho region lavas, southern end of the Central Andean Volcanic Zone (27·58S). In: Proceedings of the 12th Congreso Geologico Chileno, Santiago, S7 019.
Mpodozis, C., Ramos, V.A., 1989. The Andes of Chile and Argentina. In: Ericksen, G.E., Cañas Pinochet, M.T., Rieinemud, J.A. (Eds.), Geology of the Andes and its Relation to Hydrocarbon and Mineral Resources, 11, pp. 59–90. Circumpacific Council for Energy and Mineral Resources, Earth Science Series.
Mpodozis, C., Cornejo, P., Kay, S., Tittler, A., 1995. La Franja de Maricunga: síntesis de la evolución del frente volcánico oligocenomioceno de la zona sur de los Andes Centrales. Rev. Geol. Chile 22, 273–313.
Mpodozis, C., Kay, S., Gardeweg, M., Coira, B., 1997. Geología de la región de Valle Ancho-Laguna Verde (Catamarca, Argentina): Una ventana al basamento del extremo sur de la zona volcánica de los Andes Centrales. In: Proceedings of the 8th Congreso Geológico Chileno, Antofagasta, 3. pp. 1689–1693.
Mpodozis, C., Arriagada, C., Basso, M., Roperch, P., Cobbold, P., Reich, M., 2005. Late Mesozoic to Paleogene stratigraphy of the Salar de Atacama Basin, Antofagasta, Northern Chile: Implications for the tectonics evolution of the central Andes. Tectonophys. 399, 125–154. https://doi.org/10.1016/j.tecto.2004.12.019.
Mpodozis, C., Clavero, J., Quiroga, R., Droguett, B., Arcos, R., 2018. Geología del área Cerro Cadillal-Cerro Jotabeche, región de Atacama. SERNAGEOMIN, Carta Geológica de Chile, Serie Geología Básica 200, 1 mapa escala 1:100.000. Santiago.
Mukhopadhyay, S., Sharma, J., 2010. Crustal scale detachment in the Himalayas: a reappraisal. Geophys. J. Int. 183, 850–860.
Müller, J.P., Kley, J., Jacobshagen, V., 2002. Structure and Cenozoic kinematics of the Eastern Cordillera, southern Bolivia (21°S). Tectonics 21. https://doi.org/10.1029/2001TC001340.
Müller, R.D., et al., 2016. Ocean basin evolution and global-scale plate reorganization events since Pangea breakup. Annu. Rev. Earth Planet. Sci. 44, 107–138.
Muñoz, M., Hamza, V., 1993. Heat flow and temperature gradients in Chile. Stud. Geophys. Geod. 37 (3), 315–348.
Muñoz, N., Charrier, R., Jordan, T., 2002. Interactions between basement and cover during the evolution of the Salar de Atacama basin, northern Chile. Andean Geol. 29, 55–80.
Muñoz, M., Fuentes, F., Vergara, M., Aguirr, L., Olov Nyström, J., Féraud, G., Demant, A., 2006. Abanico East Formation: petrology and geochemistry of volcanic rocks behind the Cenozoic arc front in the Andean Cordillera, central Chile (33°50´S). Rev. Geol. Chile 33, 109–140.
Muñoz, N., Blanco, N., Pananont, P., Gardeweg, M., 2007. Cenozoic subsurface stratigraphy and structure of the Salar de Atacama basin, northern Chile. J.South Am.Earth Sci. 23, 122–146.
Murillo, I., Velasquez, R., Creixell, C., 2017. Geología del área Guanta-Los Cuartitos y Paso de Vacas Heladas, escala 1:100.000. SERNAGEOMIN Carta Geológica de Chile, Serie Geología Básica.
Muruaga, C.M., 1998. Estratigrafía y Sedimentología del Terciario Superior de la Sierra de Hualfín, entre las localidades de Villavil y San Fernando, Provincia de Catamarca. Ph. D. Thesis. Universidad Nacional de Tucuman, Facultad de Ciencias Naturales e Instituto M. Lillo, 270 pp.
Nacif, S., Triep, E., Spagnotto, S., Aragon, E., Furlani, R., Álvarez, O., 2015. The flat to normal subduction transition study to obtain the nazca plate morphology using high resolution seismicity data from the nazca plate in central chile. Tectonophysics. 657, 102–112. https://doi.org/10.1016/j.tecto.2015.06.027.
Nacif, S., Lupari, M., Triep, E., Nacif, A., Alvarez, O., Folguera, A., Gimenez, M., 2017. Change in the pattern of cristal seismicity at the southern Central Andes from a local seismic network. Tectonophys. 708, 56–69.
Niemeyer, H., 2013. Geología del área Cerro Lila-Peine, Región de Antofagasta. SERNAGEOMIN. Serio Geología Básica 147. . 39p, Santiago.
Niemeyer, H., Urrutia, C., 2009. Transcurrencia a lo largo de la Falla Sierra de Varas (Sistema de fallas de la Cordillera de Domeyko), norte de Chile. Andean Geol. 36, 37–49.
Norabuena, E.O., Dixon, T.H., Stein, S., Harrison, C.G., 1999. Decelerating Nazca-South America and Nazca-Pacific plate motions. Geophys. Res. Lett. 26, 3405–3408.
Nyström, J.O., Vergara, M., Morata, D., Levi, B., 2003. Tertiary volcanism in central Chile (33°15´-33°45´S): a case of Andean Magmatism. Geol. Soc. Am. Bull. 115, 1523–1537.
Oliveros, V., Féraud, G., Aguirre, L., Fornari, M., Morata, D., 2006. The Early Andean Magmatic Province (EAMP): 40Ar/39Ar dating on Mesozoic volcanic and plutonic rocks from the Coastal Cordillera, northern Chile. J. Volcanol. Geotherm. Res. 157, 311–330.
Oncken, O., Sobolev, S., Stiller, M., Luschen, E., 2003. Seismic imaging of a convergent continental margin and plateau in the central Andes (Andean Continental Research Project 1996 ANCORP' 96). J. Geophys. Res. Solid Earth 108, 2328. https://doi.org/10.1029/2002JB001771.
Oncken, O., Hindle, D., Kley, J., Elger, K., Victor, P., Schemmann, K., 2006. Deformation of the Central Andean Upper Plate System — facts, fiction, and constraints for plateau models. In: The Andes. Springer, Berlin Heidelberg, pp. 3–27. https://doi.org/10.1007/978-3-540-48684-8_1.
Oncken, O., Boutelier, D., Dresen, G., Schemmann, K., 2012. Strain accumulation controls failure of a plate boundary zone: linking deformation of the Central Andes and lithosphere mechanics. Geochem. Geophys. Geosyst. 13. https://doi.org/10.1029/2012GC004280. . Q12007.
Ord, A., Hobbs, B.E., 1989. The strength of the continental crust, detachment zones and the development of plastic instabilities. Tectonophysics 158, 269–289.
Ortiz, G., Alvarado, P., Fosdick, J.C., Perucca, L., Saez, M., Venerdini, A., 2015. Active deformation in the northern Sierra de Valle Fertil, Sierras Pampeanas, Argentina. J. S. Am. Earth Sci. 64, 339–350. https://doi.org/10.1016/j.jsames.2015.08.015. . (2015).
Ortiz, G., Goddard, A.L.S., Fosdick, J.C., Alvarado, P., Carrapa, B., Cristofolini, E., 2021. Fault reactivation in the Sierras Pampeanas resolved across Andean extensional and compressional regimes using thermocrhonologic modeling. J. S. Am. Earth Sci. 112 (6), 103533.
Pardo, M., Comte, D., Monfret, T., 2002. Seismotectonic and stress distribution in the central Chile subduction zone. J. S. Am. Earth Sci. 15, 11–22.
Pardo-Casas, F., Molnar, P., 1987. Relative motions of the Nazca (Farallon) and South American plates since late Cretaceous time. Tectonics 6, 233–248.
Payrola, P., Powell, J., del Papa, C., Hongn, F., 2009. Middle Eocene deformation-sedimentation in the Luracatao Valley: tracking the beginning of the foreland basin of northwestern Argentina. J. S. Am. Earth Sci. 28, 142–154.
Pearson, D., et al., 2012. Major Miocene exhumation by fault-propagation folding within a metamorphosed, early Paleozoic thrust belt: Northwestern Argentina. Tectonics 31 (4), 1–24. https://doi.org/10.1029/2011TC003043.
Pearson, D., Kapp, P., DeCelles, P.G., Reiners, P.W., Gehrels, G.E., Ducea, M.N., Pullen, A., 2013. Influence of pre-Andean crustal structure on Cenozoic thrust belt kinematics and shortening magnitude: Northwestern Argentina. Geosphere 9 (6), 1766–1782. https://doi.org/10.1130/GES00923.S2.
Perarnau, M., Gilbert, H., Alvarado, P., Martino, R., Anderson, M., 2012. Crustal structure of the Eastern Sierras Pampeanas of Argentina using high frequency local receiver functions. Tectonophys. 580, 208–217.
Pérez-Peña, J.V., Al-Awabdeh, M., Azañón, J.M., Galve, G., Booth-Rea, J.P., Notti, D.,

2017. SwathProfiler and NProfiler: Two new ArcGIS Add-ins for the automatic extraction of swath and normalized river profiles. Comput. Geosci. 104, 135–150. https://doi.org/10.1016/j.cageo.2016.08.008.
Perucca, L.P., Martos, L.M., 2012. Geomorphology, tectonism and Quaternary landscape evolution of the central Andes of San Juan (30°S–69°W), Argentina. Quat. Int. 253, 80–90. https://doi.org/10.1016/j.quaint.2011.08.009.
Perucca, L.P., Vargas, N., 2014. Neotectónica de la provincia de San Juan, centro-oeste de Argentina. Bol. Soc. Geol. Mex. 66, 291–304.
Perucca, L.P., Espejo, K., Angillieri, M.Y.E., Rothis, M., Tejada, F., Vargas, M., 2018. Neotectonic controls and stream piracy on the evolution of a river catchment: a case study in the Agua de la Peña River basin, Western Pampean Ranges, Argentina. J. Iber. Geol. 44, 207–224. https://doi.org/10.1007/s41513-018-0052-8.
Petrinovic, I., Martí, J., Aguirre-Diaz, G.J., Guzmán, S., Geyer, A., Paz, N.S., 2010. The Cerro Aguas Calientes caldera, NW Argentina: an example of a tectonically controlled, polygenetic collapse caldera, and its regional significance. J. Volcanol. Geotherm. Res. 194, 15–26. https://doi.org/10.1016/j.jvolgeores.2010.04.012.
Petrinovic, I., Hernando, I., Guzmán, S.R., 2021. Miocene to Recent collapse calderas of the southern and central volcanic zones of the Andes and their tectonic constraints. Int. . Earth Sci 110, 2399–2434.
Pilger, R., 1981. Plate Reconstructions, Aseismic Ridges, and Low-Angle Subduction Beneath the Andes. Geol. Soc. Am. Bull. 92, 448–456.
Pineda, G., Emparán, C., 2006. Geología del área Vicuña-Pichasca, Región de Coquimbo. SERNAGEOMIN Carta Geológica de Chile, Serie Geología Básica 97, 40.
Pingel, H., Alonso, R., Altenberger, U., Cottle, J., Strecker, M., 2019. Miocene to Quaternary basin evolution at the southeastern Andean Plateau (Puna) margin (ca. 24°S lat, Northwestern Argentina). Basin Res. https://doi.org/10.1111/bre.12346.
Piquer, J., Berry, R.F., Scott, R.J., Cooke, D.R., 2016. Arc-oblique fault systems: their role in the Cenozoic structural evolution and metallogenesis of the Andes of central Chile. J. Struct. Geol. 89, 101–117.
Piquer, J., Hollings, P., Rivera, O., Cooke, D.R., Baker, M., Testa, F., 2017. Along-strike segmentation of the Abanico Basin, central Chile: New chronological, geochemical and structural constraints. Lithos 268–271, 174–197.
Poma, S., Ramos, A.M., Litvak, V.D., Quenardelle, S.M., Maisonnave, E.B., Díaz, I., 2017. Southern Central Andes Neogene magmatism over the Pampean flat slab: implications on crustal and slab melts contribution to magma generation in Precordillera, Western Argentina. Andean Geol. 44, 249–274.
Pope, D., Willett, S.D., 1996. Thermal-mechanical model for crustal thickening in the central Andes driven by ablative subduction. Geology 26, 511–514.
Porras, H., Pinto, L., Tunik, M., Giambiagi, L., Deckart, K., 2016. Provenance of the Miocene Alto Tunuyán Basin (33°40′S, Argentina) and its implications for the evolution of the Andean Range: insights from petrography and U–Pb LA–ICPMS zircon ages. Tectonophys. 690, 298–317. https://doi.org/10.1016/j.tecto.2016.09.034.
Porth, R.A., 2000. Strain-rate-dependent force model of lithospheric strength. Geophys. J. Int. 141 (3), 647–660.
Prezzi, C.B., Alonso, R.N., 2002. New paleomagnetic data from the northern Argentine Puna: Central Andes rotation pattern reanalyzed. J. Geophys. Res. 107 (B2), 2041. https://doi.org/10.1029/2001JB000225.
Prezzi, C., Götze, H.-J., Schmidt, S., 2009. 3D density model of the Central Andes. Phys. Earth Planet. Inter. 177, 217–234. https://doi.org/10.1016/j.pepi.2009.09.004.
Prezzi, C., Iglesia Llanos, M.P., Götze, H.J., Schmidt, S., 2014. Thermal and geodynamic contributions to the elevation of the Altiplano-Puna plateau. Phys. Earth Planet. Inter. 237, 51–64.
Price, R., 1981. The Cordilleran foreland thrust and fold belt in the southern Canadian Rocky Mountains. Geol. Soc. Lond. Spec. Publ. 9, 427–448.
Quade, J., et al., 2015. The growth of the central Andes, 22°S-26°S. In: DeCelles et al. (Eds), Geodynamics of a Cordilleran Orogenic System: The Central Andes of Argentina and Northern Chile: Geol. Soc. Am. Memoir. pp. 277–308.
Quiero, F., Tassara, A., Iaffaldano, G., Rabbia, O., 2022. Growth of Neogene Andes linked to changes in plate convergence using high-resolution kinematic models. Nat. Commun. 13, 1339.
Quinteros, J., Sobolev, S., 2013. Why has the Nazca plate slowed since the Neogene? Geology 41, 31–34.
Quiroga, R., et al., 2021. Spatio-temporal variations of the strain field in the southern Central Andes broken-foreland (27°30′S) during the Late Cenozoic. J. S. Am. Earth Sci. https://doi.org/10.1016/j.jsames.2020.102981.
Ramirez, C.F., Gardeweg, M., 1982. Hoja Toconao, Region de Antofagasta. SERNAGEOMIN Carta Geol de Chile. 54. p. 122.
Ramos, V.A., 2018. Tectonic evolution of the central Andes: From terrane accretion to crustal delamination. In: Zamora, G., McClay, K.M., Ramos, V.A. (Eds.), Petroleum basins and hydrocarbon potential of the Andes of Peru and Bolivia. Am. Assoc. Petroleum Geol. Memoir, 117, pp. 1–34.
Ramos, V.A., Godoy, E., Godoy, V., Pángaro, F., 1996a. Evolución tectónica de la cordillera principal Argentino–Chilena a la latitud del Paso de Piuquenes (33°30′S). In: Proceedings of the 13th Congreso Geológico Argentino, Buenos Aires. pp. 337–352. (1996a).
Ramos, V.A., Cegarra, M., Cristallini, E., 1996b. Cenozoic tectonics of the high Andes of west-central Argentina (30-36°S latitude). Tectonophys. 259, 185–200. https://doi.org/10.1016/0040-1951(95)00064-x.
Ramos, V.A., Cristallini, E., Pérez, D., 2002. The Pampean flat-slab of the Central Andes. J. S. Am. Earth Sci. 15, 59–78.
Ramos, V.A., Zapata, T.R., Cristallini, E.O., Introcaso, A., 2004. The Andean thrust system—latitudinal variations in structural styles and orogenic shortening. In: McClay, K.R. (Ed.), Thrust Tectonics and Hydrocarbon Systems. Am. Assoc. Petroleum Geol. Memoir. pp. 30–50. https://doi.org/10.1306/M82813C3.
Re, G., Jordan, T., Kelley, S., 2003. Cronología y paleogeografía del Terciario de la cuenca intermontana de Iglesia septentrional, Andes de San Juan, Argentina. Rev. Asoc. Geol. Argentina 58, 31–48.
Reat, E.J., Fosdick, J.C., 2018. Basin evolution during Cretaceous-Oligocene changes in sediment routing in the Eastern Precordillera, Argentina. J. S. Am. Earth Sci. 84, 422–443. https://doi.org/10.1016/j.jsames.2018.02.010.
Reiners, P., et al., 2015. Low-temperature thermochronology trends across the Central Andes, 21°S-28°S. Geol. Soc. Am. Mem. 212. https://doi.org/10.1130/2015.1212(12).
Reutter, K.J., Scheuber, E., Wigger, P., 1994. Tectonics of the Southern Central Andes: Structure and Evolution of an Active Continental Margin. Springer-Verlag, Berlin. 335 pp.
Reutter, K., Scheuber, E., Chong, G., 1996. The Precordillera fault system of Chuquicamata, northern Chile: evidence for reversal along arc-parallel strike-slip faults. Tectonophys. 259, 213–228.
Reynolds, J.H., Jordan, T.E., Johnson, N.M., Damanti, J.F., Tabbutt, K., 1990. Neogene deformation of the flatsubduction segment of the Argentine-Chilean Andes: magnetostratigraphic constraints from Las Juntas, La Rioja province, Argentina. Geol. Soc. Am. Bull. 102, 1607–1622. https://doi.org/10.1130/0016- 7606(1990)1022.3.CO;2.
Reynolds, J.H., Galli, C.I., Hernández, R.M., Idleman, B.D., Kotila, J.M., Hilliard, R.V., Naeser, C.W., 2000. Middle Miocene tectonic development of the Transition Zone, Salta Province, northwest Argentina: Magnetic stratigraphy from the Metan Subgroup, Sierra de Gonzalez. Geol. Soc. Am. Bull. 112 (11), 1736–1751.
Richard, A.D., 2020. Modelado cinemático aplicado a neotectónica en el frente orogénico andino entre 32°10´S – 32°40´S, provincias de Mendoza y San Juan. PhD thesis. Universidad Nacional de San Luis. 189 pp.
Richard, A.D., Costa, C., Giambiagi, L., Moreno Marcó, C., Ahumada, E., Vázquez, F., 2019. Neotectónica del extremo austral de la falla La Rinconada, Precordillera oriental, provincia de San Juan. Rev. Asoc. Geol. Argentina 76 (1), 24–39.
Richardson, T., Gilbert, H., Anderson, M., Ridgway, K., 2012. Seismicity within the actively deforming Eastern Sierras Pampeanas, Argentina. Geophys. J. Int. 188, 408–420.
Riesner, M., Lacassin, R., Simoes, M., Carrizo, D., Armijo, R., 2018. Revisiting the crustal structure and kinematics of the Central Andes at 33.5°S: implications for the mechanics of Andean mountain building. Tectonics 37, 1347–1375. https://doi.org/10.1002/2017TC004513.
Riesner, M., Simoes, M., Carrizo, D., Lacassin, R., 2019. Early exhumation of the Frontal Cordillera (Southern Central Andes) and implications for Andean mountain-building at~ 33.5° S. Sci. Rep. 9 (1), 1–10.
Riller, U., Petrinovic, I., Ramelow, J., Strecker, M.R., Oncken, O., 2001. Late Cenozoic tectonism, collapse caldera and plateau formation in the central Andes. Earth Planet. Sci. Lett. 188, 299–311. https://doi.org/10.1016/S0012-821X(01)00333-8.
Riller, U., Cruden, A.R., Boutelier, D., Schrank, C., 2012. The causes of sinuous crustal-scale deformation patterns in hot orogens: evidence from scaled analogue experiments and the southern Central Andes. J. Struct. Geol. 37, 65–74.
Rimando, J., Schoenbohm, L.M., Costa, C.H., Owen, L.A., Cesta, J.M., Richard, A.D., Gardini, C.E., 2019. Late Quaternary Activity of the La Rinconada Fault Zone, San Juan, Argentina. Tectonics 38, 916–940. https://doi.org/10.1029/2018TC005321.
Riquelme, R., Martinod, J., Hérail, G., Darrozes, J., Charrier, R., 2003. A geomorphological approach to determining the Neogene to Recent tectonic deformation in the Coastal Cordillera of northern Chile (Atacama). Tectonophys. 361, 255–275.
Rivas, C., Ortiz, G., Alvarado, P., Podesta, M., Martin, A., 2019. Modern cristal seismicity in the northern Andean Precordillera, Argentina. Tectonophys. 762, 144–158.
Rodríguez Fernández, L.R., Heredia, N., Espina, R., Cegarra, M., 1999. Estratigrafía y estructura de los Andes Centrales Argentinos entre los 30° y 31°S de Latitud Sur. Acta Geol. Hisp. 32, 51–75.
Rodríguez, M.P., Pinto, L., Encinas, A., 2012. Cenozoic erosion in the Andean forearc in Central Chile (33°–34°S): Sediment provenance inferred by heavy mineral studies. In: Rasbury, E.T., Hemming, S.R., Riggs, N.R. (Eds.), Mineralogical and Geochemical Approaches to Provenance. Geol. Soc. Am. Special Paper, 487, pp. 141–162. https://doi.org/10.1130/2012.2487(09).
Rodríguez, M.P., Charrier, R., Brichau, S., Carretier, S., Farías, M., de Parseval, P., Ketcham, R.A., 2018. Latitudinal and Longitudinal Patterns of Exhumation in the Andes of North-Central Chile. Tectonics 37, 2863–2886. https://doi.org/10.1029/2018TC004997.
Roeder, D., 1988. Andean-age structure of Eastern Cordillera (Province of La Paz, Bolivia). Tectonics 7, 23–39.
Rojas Vera, E., Giampaoli, P., Gobbo, E., Rocha, E., Olivieri, G., Figueroa, D., 2019. Structure and tectonic evolution of the Interandean and Subandean zones of the central Andean fold-and-thrust belt of Bolivia. Andean Tectonics. https://doi.org/10.1016/B978-0-12-816009-1.00016-2.
Royden, L., 1996. Coupling and decoupling of crust and mantle in convergent orogens: implications for strain partitioning in the crust. J. Geophys. Res. 101. . 17,679-17,705.
Ruskin, B., Jordan, T., 2007. Climate change across continental sequence boundaries: paleopedology and lithofacies of Iglesia basin, northwestern Argentina. J. Sediment. Res. 77, 661–679.
Safipour, R., Carrapa, B., DeCelles, P.G., Thomson, S.N., 2015. Exhumation of the Precordillera and northern Sierras Pampeanas and along-strike correlation of the Andean orogenic front, northwestern Argentina. In: DeCelles, P.G., Ducea, M.N., Carrapa, B., Kapp, P.A. (Eds.), Geodynamics of a Cordilleran Orogenic System: The Central Andes of Argentina and Northern Chile. Geol. Soc. Am. Memoir, 212, pp. 181–199. https://doi.org/10.1130/2015.1212(10).
Salazar, P., Kummerow, J., Wigger, P., Shapiro, S., Asch, G., 2017. State of stress and crustal fluid migration related to west-dipping structures in the slab-forearc system in the northern Chilean subduction zone. Geophys. J. Int. 208, 1403–1413. https://

doi.org/10.1093/gji/ggw463.
Salfity, J.A., Marquillas, R.A., 1994. Tectonic and sedimentary evolution of the Cretaceous-Eocene Salta Group Basin, Argentina. In: Salfity, J. (Ed.), Cretaceous Tectonics of the Andes, Vieweg, Brunswick. Germany, pp. 266–315.
Santibáñez, I., Cembrano, J., García-Pérez, T., Costa, C., Yáñez, G., Marquardt, C., Arancibia, G., González, G., 2019. Crustal faults in the Chilean Andes: geological constraints and seismic potential. Andean Geol. 46 (1), 32–65. https://doi.org/10.5027/andgeoV46n1-3067.
Sasso, A.M., 1997. Geological evolution and metallogenetic relationships of the Farallon Negro Volcanic Complex, NW Argentina. PhD Thesis. Queen University, 842 p, Kingston.
Saylor, J.E., Horton, B.K., 2014. Nonuniform surface uplift of the Andean plateau revealed by deuterium isotopes in Miocene volcanic glass from southern Peru. Earth Planet. Sci. Lett. 387, 120–131. https://doi.org/10.1016/j.epsl.2013.11.015.
Schellart, W.P., 2017. Andean mountain building and magmatic arc migration driven by subduction-induced whole mantle flow. Nat. Commun. 8, 2010. https://doi.org/10.1038/s41467-017-01847-z.
Schellart, W.P., Freeman, J., Stegman, D.R., Moresi, L., May, D., 2007. Evolution and diversity of subduction zones controlled by slab width. Nature 446, 308–311.
Scheuber, E., Giese, P., 1999. Architecture of the Central Andes: a compilation of geoscientific data along a transect at 21°S. J. S. Am. Earth Sci. 12, 103–107.
Scheuber, E., Mertmann, D., Ege, H., Silva-González, P., Heubeck, C., Reutter, K.J., Jacobshagen, V., 2006. Exhumation and basin development related to formation of the Central Andean plateau, 21°S. In: The Andes. https://doi.org/10.1007/978-3-540-48684-8_13.
Schmeling, H., Babeyko, A.Y., Enns, A., et al., 2008. A benchmark comparison of spontaneous subduction models-towards a free surface. Phys. Earth Planet. Inter. 171, 198–223. https://doi.org/10.1016/j.pepi.2008.06.028.
Schmitz, M.A., 1994. balanced model of the Southern Central Andes. Tectonics 13, 484–492.
Schmitz, M., Kley, J., 1997. The geometry of the Central Andean backarc crust: joint interpretation of cross-section balancing and seismic refraction data. J. S. Am. Earth Sci. 10, 99–110.
Schoenbohm, L.M., Strecker, M.R., 2009. Normal faulting along the southern margin of the Puna Plateau, northwest Argentina. Tectonics 28, TC5008. https://doi.org/10.1029/2008TC002341.
Scholz, C.H., 1990. Mechanics of Faulting and Earthquakes. Cambridge University Press, Cambridge. 484 pp.
Schott, B., Schmeling, H., 1998. Delamination and detachment of a lithospheric root. Tectonophys. 296, 225–247. https://doi.org/10.1016/S0040-1951(98)00154-1.
Schurr, B., Asch, G., Rietbrock, A., Kind, R., Pardo, M., Heit, B., Monfret, T., 1999. Seismicity and average velocity beneath the Argentine Puna. Geophys. Res. Lett. 26, 3015–3028.
Schurr, B., Asch, G., Rietbrock, A., Trumbull, R., Haberland, C., 2003. Complex patterns of fluid and melt transport in the central Andean subduction zone revealed by attenuation tomography. Earth Planet. Sci. Lett. 215, 105–119.
Seeber, L., Armbruster, J., Quittmeyer, R., 1981. Seismicity and continental subduction in the Himalayan arc. In: Gupta, H.K., Delany, F.M. (Eds.), Zagros, Hindu Kush, Himalaya, Geodynamic Evolution. American Geophysical Unions, Geodynamic Series 3, Washington DC, pp. 215–242.
Seggiaro, R.E., et al., 1998. Estudio geológico integrado de la Quebrada de Humahuaca. Argentina, Servicio Geológico Nacional, p. 88.
Seggiaro, R.E., et al., 2014. evolución tectónica Andina entre las Sierras de Hualfin, Capillitas y extremo sur de Aconquija, Provincia de Catamarca. Rev. la Asoc. Argent. 71 (4), 500–512.
Sempere, T., Herail, G., Oller, J., Bonhomme, M.G., 1990. Late Oligocene-early Miocene major tectonic crisis and related basins in Bolivia. Geology 18, 946–949.
Sempere, T., Butler, R.F., Richards, D.R., Marshall, L.G., Sharp, W., Swisher Iii, C.C., 1997. Stratigraphy and chronology of Upper Cretaceous-lower Paleogene strata in Bolivia and northwest Argentina. Bull. Geol. Soc. Am. 109, 709–727. https://doi.org/10.1130/0016-7606(1997)1092.3.CO;2.
Sheffels, B.M., 1990. Lower bound on the amount of crustal shortening in the central Bolivian Andes. Geology 18, 812–815. https://doi.org/10.1130/0091-7613(1990)0182.3.CO;2.
Siame, L.L., Bellier, O., Sébrier, M., Araujo, M., 2005. Deformation partitioning in flat subduction setting: case of the Andean foreland of western Argentina (28°S-33°S). Tectonics 24. https://doi.org/10.1029/2005TC001787.
Siks, B., Horton, B., 2011. Growth and fragmentation of the Andean foreland basin during eastward advance of fold-thrust deformation, Puna plateau and Eastern Cordillera, northern Argentina. Tectonics 30, TC6017. https://doi.org/10.1029/2011TC002944.
Silva-González, P., 2004. Der südliche Altiplano im Tertiär: Sedimentáre Entwicklung und tektonische Implikationen. Ph.D. thesis. Freie Univ, Berlin, Germany.
Silvestro, J., Kraemer, P., Achilli, F., Brinkworth, W., 2005. Evolución de las cuencas sinorogénicas de la Cordillera Principal entre 35°-36° S. Malargüe. Rev. Asoc. Geol. Argentina 60 (4), 627–643.
Smalley, R., Isacks, B., 1990. Seismotectonics of thin- and thick-skinned deformation in the Andean foreland from local network data: Evidence for a seismogenic lower crust. J. Geophys. Res. 95. . 12,487-12,497.
Smalley, R.F., et al., 1993. Basement seismicity beneath the Andean Precordillera thinskinned thrust belt and implications for crustal and lithospheric behavior. Tectonics 12, 63–76.
Sobel, E.R., Strecker, M.R., 2003. Uplift, exhumation and precipitation: tectonic and climatic control of Late Cenozoic landscape evolution in the northern Sierras Pampeanas. Argentina. Basin Res. 15, 431–451.
Sobolev, S., Babeyko, A., 2005. What drives orogeny in the Andes? Geology 33, 617–620. https://doi.org/10.1130/G21557.1.
Somoza, R., 1998. Updated Nazca (Farallon)-South America relative motions during the last 40 Ma: Implications for mountain building in the Central Andean region. J. S. Am. Earth Sci. 11, 211–215.
Somoza, R., Singer, S., Coira, B., 1996. Paleomagnetism of upper Miocene ignimbrites at the Puna: An analysis of vertical-axis rotations in the Central Andes. J. Geophys. Res. 101 (B5). . 11387 ± 11400.
Soto, R., Martinod, J., Riquelme, R., Hérail, G., Audin, L., 2005. Using geomorphological markers to discriminate Neogene tectonic activity in the Precordillera of North Chilean forearc (24-25°S). Tectonophys. 411, 41–55.
Spagnotto, S., Triep, E., Giambiagi, L., Lupari, M., 2015. Triggered seismicity in the Andean arc region via static stress variation by the Mw = 8.8, February 27, 2010, Maule Earthquake. J. S. Am. Earth Sci. 63, 36–47.
Springer, M., 1999. Interpretation of heat-flow density in the Central Andes. Tectonophysics 306 (3–4), 377–395.
Springer, M., Förster, A., 1998. Heat-flow density across the Central Andean subduction zone. Tectonophysics 291 (1–4), 123–139.
Stalder, N.F., Herman, F., Fellin, G.M., Coutand, I., Aguilar, G., Reiners, P.W., Fox, M., 2020. The relationships between tectonics, climate and exhumation in the Central Andes (18–36°S): Evidence from low-temperature thermochronology. Earth Sci. Rev. https://doi.org/10.1016/j.earscirev.2020.103276.
Stern, Ch., 2020. The role of subduction erosion in the generation of Andean and other convergent plate boundary arc magmas, the continental crust and mantle. Gondwana Res. 88, 220–249.
Strecker, M.R., Cerveny, P., Arthur, L., Malizia, D., 1989. Late Cenozoic tectonism and landscape development in the foreland of the Andes: northern Sierras Pampeanas (26°–28°S), Argentina. Tectonics 8, 517–534. https://doi.org/10.1029/TC008i003p00517.
Strecker, M.R., Alonso, R.N., Bookhagen, B., Carrapa, B., Hilley, G.E., Sobel, E.R., Trauth, M.H., 2007. Tectonics and climate of the southern central Andes. Annu. Rev. Earth Planet. Sci. 35, 747–787. https://doi.org/10.1146/annurev.earth.35.031306.140158.
Suppe, J., 1981. Mechanics of mountain building and metamorphism in Taiwan. Geol. Soc. China Mem. 4, 67–89.
Suriano, J., Limarino, C.O., Tedesco, A.M., Alonso, M.S., 2015. Sedimentation model of piggyback basins: Cenozoic examples of San Juan Precordillera, Argentina. In: Sepulveda, et al. (Ed.), Geodynamic Processes in the Andes of Central Chile and Argentina. Geol. Soc., London, Spec. Pub. 399. https://doi.org/10.1144/SP399.17.
Suriano, J., Mardonez, D., Mahoney, J.B., Mescua, J.F., Giambiagi, L.B., Kimbrough, D., Lossada, A., 2017. Uplift sequence of the Andes at 30°S: insights from sedimentology and U/Pb dating of synorogenic deposits. J. S. Am. Earth Sci. 75, 11–34.
Tao, W.C., O'Connell, R.J., 1992. Ablative subduction: a two-sided alternative to the conventional subduction model. J. Geophys. Res. 97, 8877–8904.
Tassara, A., 2005. Interaction between the Nazca and South American plates and formation of the Altiplano–Puna plateau: Review of a flexural analysis along the Andean margin (15–34 S). Tectonophysics 399 (1–4), 39–57.
Tassara, A., Echaurren, A., 2012. Anatomy of the Andean subduction zone: three-dimensional density model upgraded and compared against global-scale models. Geophys. J. Int. 189, 161–168. https://doi.org/10.1111/j.1365-246X.2012.05397x.
Tassara, A., Swain, C., Hackney, R., Kirby, J., 2007. Elastic thickness structure of South America estimated using wavelets and satellite-derived gravity data, Earth planet. Sci. Lett. 253, 17–36.
Tomlinson, A.J., Mpodozis, C., Cornejo, P.C., Ramirez, C.F., 1993. Structural Geology of the Sierra Castillo–Agua Amarga Fault System, Precordillera of Chile, El Salvador-Potrerillos. Second ISAG, Oxford (K). pp. 259–262.
Tomlinson, A., Mpodozis, C., Cornejo, P., Ramirez, C., Dumitru, T., 1994. El sistema de fallas Sierra Castillo – Agua Amarga: Transpresió sinestral eocena en la Precordillera de Potrerillos, El Salvador, in: proceedings of the 7th Congreso Geológico Chileno. pp. 1459–1463.
Tomlinson, A., Blanco, N., Maksaev, V., Dilles, J., Grunder, A.L., Ladino, M., 2001. Geología de la Precordillera andina de Quebrada Blanca – Chuquicamata, Regiones I y II (20°30´-22°30´S). Servicio Nacional de Geología y Minería, Chile, Informe registrado IR-01-20, 2, 444 pp, 20 maps (1:50.000), Santiago.
Tomlinson, A.J., Blanco, N., Dilles, J.H., 2010. Carta Calama, Región de Antofagasta, CartaGeológica de Chile, Serie Preliminar 8, Servicio Nacional de Geología y Minería, Santiago 1:50000.
Tomlinson, A., Blanco, N., Dilles, J., Maksaev, V., Ladino, M., 2018. Carta Calama, región de Antofagasta. Servicio Nacional de Geología y Minería, Carta Geológica de Chile, Serie Geología Básica 199: 213 p. Santiago.
Tunik, M., Folguera, A., Naipauer, M., Pimentel, M., Ramos, V.A., 2010. Early uplift and orogenic deformation in the Neuquén Basin: Constraints on the Andean uplift from U–Pb and Hf isotopic data of detrital zircons. Tectonophys. 489, 258–273.
Turcotte, D.L., Schubert, G., 2014. Geodynamics, 3rd ed. Cambridge University Press. https://doi.org/10.1017/CBO9780511843877.
Uba, C.E., Heubeck, C., Hulka, C., 2005. Facies analysis and basin architecture of the Neogene Subandean synorogenic wedge, southern Bolivia. Sediment. Geol. 180, 91–123.
Uba, C.E., Heubeck, C., Hulka, C., 2006. Evolution of the late Cenozoic Chaco foreland basin, Southern Bolivia. Basin Res. 18, 145–170. . 10/1111/j.1365-2117.2006.00291.x.
Uba, C.E., Kley, J., Strecker, M.R., Schmitt, A.K., 2009. Unsteady evolution of the Bolivian Subandean thrust belt: the role of enhanced erosion and clastic wedge progradation. Earth Planet. Sci. Lett. 281, 134–146. https://doi.org/10.1016/j.epsl.2009.02.010.
Uyeda, S., Kanamori, H., 1979. Back-arc opening and the mode of subduction. J. Geophis. Res. 84, 1049–1061.
Uyeda, S., Watanabe, T., 1982. Terrestrial heat flow in western South America. Tectonophysics 83 (1–2), 63–70.

Vanderhaeghe, O., Medvede, S., Fullsack, P., Beaumont, C., Jamieson, R., 2003. Evolution of orogenic wedges and continental plateaux: Insights from crustal thermal-mechanical models overlying subducting mantle lithosphere. Geophys. J. Int. 153, 27–51.

Vargas, G., et al., 2014. Probing large intraplate earthquakes at the west flank of the Andes. Geology 42, 1083–1086.

Vergara, M., Morata, D., Villarroel, R., Nyström, J., Aguirre, L., 1999. Ar/Ar ages, very low-grade metamorphism and geochemistry of the volcanic rocks from "Cerro El Abanico", Santiago Andean Cordillera (33°30´S-70°30´-70°25´W). In: Proceedings of the 4° International Symposium on Andean Geodynamics, Göttingen, Germany. pp. 785–788.

Victor, P., Oncken, O., Glodny, J., 2004. Uplift of the western Altiplano plateau: evidence from the Precordillera between 20° and 21°S (northern Chile). Tectonics 23. https://doi.org/10.1029/2003TC001519.

Villegas, A., Raquel, J., Zahradnik, J., Nacif, S., Spagnotto, S., Winocur, D., Flavia Leiva, M., 2016. Waveform inversion and focal mechanisms of two weak earthquakes in Cordillera Principal (Argentina) between 35 degrees and 35.5 degrees S. J. S. Am. Earth Sci. 71, 359–369.

Watts, A.B., Lamb, S.H., Fairhead, J.D., Dewey, J.F., 1995. Lithospheric flexure and bending of the Central Andes. Earth Plan. Scie. Let. 134, 9–21.

Wdowinski, S., Bock, Y., 1994. The evolution of deformation and topography of high elevated plateaus, 2. Application to the central Andes. J. Geophys. Res. 99, 7121–7130.

Wdowinski, S., O'Connell, R.J., 1991. Deformation of the central Andes (15-27S) derived from a flow model of subduction zones. J. Geophys. Res. 96, 12245–12255.

Wigger, P.J., et al., 1994. Variation in the crustal structure of the southern central Andes deduced from seismic refraction investigations. In: Reutter, K.J., Scheuber, E., Wigger, P.J. (Eds.), Tectonics of the Southern Central Andes. Springer-Verlag, Berlin, pp. 23–48.

Willett, S., Beaumont, C., Fullsack, P., 1993. Mechanical model for the tectonics of doubly vergent compressional orogens. Geology 21, 371–374.

Winocur, D.A., Litvak, V.D., Ramos, V.A., 2015. Magmatic and tectonic evolution of the Oligocene Valle del Cura Basin, Main Andes of Argentina and Chile: Evidence for generalized extension. In: Geodynamic processes in the Andes of central Chile and Argentina. Geol. Soc. Special Publ. 399. pp. 109–130.

Yamano, M., Uyeda, S., 1990. Heat-flow studies in the Peru Trench subduction zone. In: Proc. Ocean Drill. Program, Sci. Results, Vol. 112, pp. 653–661.

Yáñez, G., Cembrano, J., 2004. Role of viscous plate coupling in the late Tertiary Andean tectonics. J. Geophys. Res. 109, B02407. https://doi.org/10.1029/2003JB002494.

Yáñez, G., Perez-Estay, N., Araya-Vargas, J., Sanhueza, J., Figueroa, R., Maringue, J., Rojas, T., 2020. Shallow anatomy of the San Ramón Fault (Chile), constrained by geophysical methods: Implications for its role in the Andean deformation. Tectonics 39. https://doi.org/10.1029/2020TC006294. . e2020TC006294.

Yonkee, A., Weil, A., 2010. Reconstructing the kinematic evolution of curved mountain belts: Iinternal strain patterns in the Wyoming salient, Sevier thrust belt, USA. Geol. Soc. Am. Bull. 122, 24–49.

Yuan, X., et al., 2000. Subduction and collision processes in the Central Andes constrained by converted seismic phases. Nature 408, 958–961.

Yuan, X., Sobolev, S.V., Kind, R., 2002. Moho topography in the central Andes and its geodynamic implications. Earth Planet. Sci. Lett. 199, 389–402.

Zapata, T.R., Allmendinger, R.W., 1996. Thrust-front zone of the Precordillera, Argentina: a thick-skinned triangle zone. Am. Assoc. Pet. Geol. Bull. 80 (3), 359–381.

Zapata, S., Sobel, E.R., del Papa, C., Jelinek, A.R., Glodny, J., 2019. Using a paleosurface to constrain low-temperature thermochronological data: tectonic evolution of the Cuevas range, Central Andes. Tectonics 38. https://doi.org/10.1029/2019TC005887.

Zapata, S., Sobel, E., del Papa, C., Glodny, J., 2020. Upper plate controls on the formation of broken foreland basins in the Andean retro-arc between 26 and 28°S: from Cretaceous rifting to Paleogene and Miocene broken foreland basins. Geochem. Geophys. Geosyst. 21. https://doi.org/10.1029/2019GC008876.

Zhou, R., Schoenbohm, L., Sobel, E., Davis, D., Glodny, J., 2017. New constraints on orogenic models of the southern Central Andean Plateau: cenozoic basin evolution and bedrock exhumation. Geol. Soc. Am. Bull. 129, 152–170. https://doi.org/10.1130/B31384.1.